REANALYSIS OF THE EXTENDED MULTIVARIATE ENSO INDEX

by

Eric Webb

A thesis submitted to the faculty of
The University of North Carolina at Charlotte
in partial fulfillment of the requirements
for the degree of Master of Science in
Earth Science

Charlotte

2020

Approved by:

_____
Dr. Brian Magi

_____
Dr. Matthew Eastin

_____
Dr. Jacob Scheff

ABSTRACT

ERIC JAMES WEBB. Reanalysis of the Extended Multivariate ENSO Index. (Under the direction of Dr. BRIAN MAGI)

The El Nino Southern Oscillation (ENSO) is the most robust, coupled ocean-atmospheric component of intraseasonal-interannual variability on the globe. Therefore, an index that effectively characterizes a large fraction of ENSO's total variability is deemed to be of upmost importance. This work uses sea surface temperature (SST) and sea level pressure (SLP) datasets to produce a major update to the original Extended Multivariate ENSO Index (MEI.ext; Wolter and Timlin, 2011) that we call the Extended Multivariate ENSO Index version 2 (MEI.extv2). MEI.extv2 covers a timespan of 1865-2020 at a monthly time resolution where each month represents a rolling bi-monthly average, and we include accompanying estimates of the confidence intervals. By utilizing an ensemble of quality-controlled reanalysis datasets, creating a statistical suite of MEI "realizations", and applying a weighting procedure that accounts for time-varying quality and quantity of the underlying SST and SLP data since the mid-1800s, we argue that the MEI.extv2 is more robust, stable, and coherent than the original MEI.ext. A novel contribution of this work is to provide an empirical estimate of the uncertainty associated with the MEI that is built from the time-varying uncertainties apparent across the input reanalysis datasets. Overall, MEI.extv2 agrees well with the original MEI.ext, showing that ENSO was more active near the turn of the 20th and 21st centuries, but there are differences in MEI.extv2 and MEI.ext for individual ENSO events. We use our uncertainty estimates to assess conclusions about the duration, amplitude, spacing, and the onset and decay of ENSO on bi-monthly temporal scales. MEI.extv2 provides a comprehensive ENSO index that

extends from 1865 to the present day, includes a novel estimate of uncertainty, and is tied to observationally based records that themselves continue to be updated.

ACKNOWLEDGEMENTS

I would like to thank my advisor Dr. Brian Magi for providing invaluable input, guidance, and support all along the way, helping keep this project laser focused. I would like to thank Dr. Jacob Scheff for allowing me to take his programming class last year in python, it has molded me into a much better coder, and opened up a lot of future doors for this project. I would like to thank Dr Matthew Eastin for his input, discussions, and his class on instrumentation, the information I gleaned through his course provided pivotal groundwork in my understanding of the uncertainties in our data. I would like to thank Klaus Wolter for his pivotal research on the MEI as well as Dr. Geert Jan van Oldenborgh for creating the KNMI Climate Explorer tool, arguably one of the most underrated web-based weather climate tools on the web. I also extremely grateful for all my graduate student friends and colleagues at UNC-Charlotte as well as my family, their unwavering support and encouragement throughout the duration of my thesis, especially in light of the covid-19 pandemic proved pivotal in keeping me motivated to complete this project

TABLE OF CONTENTS

LIST OF TABLES

LIST OF FIGURES

LIST OF ABBREVIATIONS

Australia BOM SOI: Australian Bureau of Meteorology Southern Oscillation Index

CERA-20C: Coupled European Center for Medium Range Weather Forecast 20th Century Reanalysis

CMIP: Coupled Model Intercomparison Project

CMIP6: Coupled Model Intercomparison Project Version 6

COBE SST: Centennial In-Situ Observation-Based Estimates of the Variability of SST and Marine Meteorological Variables Version 1

COBE SST2: Centennial In-Situ Observation-Based Estimates of the Variability of SST and Marine Meteorological Variables Version 2

CTI: Cold Tongue Index

ECMWF: European Centers for Medium Range Weather Forecasting

ENSO: El Nino Southern Oscillation

EOF: Empirical Orthogonal Function

ERA: ECMWF Reanalysis

ERA-20C: European Center for Medium Range Weather Forecast 20th Century Reanalysis

ERA-20CM: European Center for Medium Range Weather Forecast 20th Century Reanalysis Model

ERI: Engine Room Intake

ERSSTv4: Extended Reconstructed Sea Surface Temperature Version 4

ERSSTv5: Extended Reconstructed Sea Surface Temperature Version 5

GFDL: Geophysical Fluid Dynamics Laboratory

HADISST: Hadley Centre Sea Ice and Sea Surface Temperature data set version 1

HADISST2.1: Hadley Centre Sea Ice and Sea Surface Temperature data set version 2.1

HADSLP: United Kingdom Met Office Hadley Centre Sea Level Pressure Dataset version 1

HADSLP2: United Kingdom Met Office Hadley Centre Sea Level Pressure Dataset version 2

Jones/CRU SOI: Jones (1987) and Climate Research Unit of East Anglia Southern Oscillation Index

JRA-55: Japanese 55-year Reanalysis

Kaplan Extended v2: Kaplan (1998)'s Extended Sea Surface Temperature dataset version 2

Kaplan SLP: Kaplan (1998)'s Sea Level Pressure dataset version 1

MARS: Meteorological Archival and Retrieval System

MEI: Multivariate ENSO Index

MEI.ext: Extended Multivariate ENSO Index

MEI.extv2: Extended Multivariate ENSO Index Version 2

MEI.v1: Multivariate ENSO Index version 1 (also known as COADS-MEI)

MEI.v2: Multivariate ENSO Index version 2

MJO: Madden-Julian Oscillation

NCEP-R1: National Centers for Environmental Prediction Reanalysis version 1

NOAA: National Oceanic Atmospheric Administration

NOAA's 20CRv2: National Oceanic Atmospheric Administration 20th Century Reanalysis Version 2

NOAA's 20CRv2c: National Oceanic Atmospheric Administration 20th Century Reanalysis Version 2c

NOAA's 20CRv3: National Oceanic Atmospheric Administration 20th Century Reanalysis Version 3

NPMM: North Pacific Meridional Mode

OLR: Outgoing Longwave Radiation

ONI: Oceanic Nino Index

PC: Principal Component

PCA: Principal Component Analaysis

PNA: Pacific-North American pattern

RMM: Realtime Multivariate MJO

SAT: Surface Air Temperature

SLP: Sea Level Pressure

SOI: Southern Oscillation Index

SPMM: South Pacific Meridional Mode

SST: Sea Surface Temperature

TAO: Tropical Atmosphere Ocean

TOGA: Tropical Ocean-Global Atmosphere program

WHOI OA Flux v3: Woods Hole Oceanographic Institute Objectively Analyzed air-sea Fluxes for the Global Oceans Version 3

CHAPTER 1: INTRODUCTION

1.1 Background

ENSO is among the first forms of climate variability to be discovered with dependence on the coupled interactions between the ocean and overlying atmosphere (Bjerknes, 1969), documented as early as Walker and Bliss (1932) and noted several centuries prior to this landmark paper to have a significant impact around Christmas time on the catch for Peruvian fisherman, with Carrillo (1892) being the first to make note of the term “El Nino” in scientific literature (McPhaden, 2014).

Wyrtiki (1975) is credited with being among the first to quantitatively associate zonal wind anomalies in the west-central Equatorial Pacific with changes in sea level, that eventually led to the discovery of the equatorially-trapped oceanic Kelvin Wave, a solution initially theorized by Matsuno (1966). Further oceanographic studies (Hulbert et al., 1976; McCreary, 1976; Philander, 1981) made the link between the aperiodic weakening of the easterly trade winds over the edge of the West Pacific Warm Pool and the zonal redistribution of heat in the upper ocean of the equatorial Pacific that is crucial to the development of El Nino.

The Madden-Julian Oscillation (MJO) was initially discovered by Roland and Madden (1971) using a decade of rawinsonde observations at Canton Island (3S, 172W) in the south Equatorial Pacific, and is a 30-90 day oscillation in the tropics consisting of coherent, coupled, eastward propagating ocean-atmosphere phenomena that is most prominent over the Indo-Pacific Warm Pool. The MJO evolves together with the large-scale, global circulation and is connected with ENSO (Zhang,1995; Roundy, 2012; Zhang, 2013). Many have made connections between gravest, lowest frequency oceanic

Kelvin Wave mode (associated with ENSO) and the MJO (Hendon et al, 1998; Zhang, 2005; Roundy and Kiladis, 2006), and Hendon et al (2007) further outlined a seasonal preference for this link in the boreal spring.

In order to monitor the subseasonal MJO, Wheeler and Hendon (2004) developed the Real-Time Multivariate MJO (RMM) index, which uses the first two leading Empirical Orthogonal Functions (EOFs) of combined fields of zonal winds at 850 hPa and 200 hPa in addition to Outgoing Longwave Radiation (OLR) in the 15N-15S latitudinal band. The utilization of combined fields instead of traditional bandpass filtering were deemed necessary to alleviate high frequency weather variability from projecting onto the EOFs (Wheeler and Hendon, 2004). However, it has also been noted that the leading pair of EOFs used to construct RMM index (Wheeler and Hendon, 2004) fail to capture an extensive fraction of MJO variability, and do not actually explain the advancement towards El Nino conditions that is largely contained within the 3rd EOF of zonal wind anomalies (Kessler, 2001; Liu, 2014; Roundy, 2015).

Nonetheless, these early observations of equatorially-trapped oceanic Kelvin Waves and their response to wind stress forcing were substantiated by the early work of Rowntree (1972), Julian and Chervin (1978), Gill (1980), Zebiak (1982), Philander et al (1984), and Zebiak and Cane (1987) who used simple and intermediate-complex coupled climate models to simulate and even predict ENSO. Rowntree (1972) and Julian and Chervin (1978) were the first to denote the importance of a general circulation model's (GCM's) contribution to the understanding of ENSO. Rowntree (1972) used 9-level atmospheric model from the NOAA Geophysical Fluid Dynamics Laboratory (GFDL) to test how tropical Pacific sea surface temperatures (SSTs) accounted for variations in the

Aleutian Low, noting that statistically significant mid-latitude effects were not evident until roughly one-week after tropical convection was initiated in the model. Julian and Chervin (1978), using only a 6-layer 5 degree (latitude by longitude) atmospheric model with fixed SSTs from the National Center for Atmospheric Research (NCAR) were able to reproduce many of what now are generally well known and accepted atmospheric expressions of El Nino, including a strong and equatorward-displaced subtropical jet in the western hemisphere.

The work of Gill (1980) led to the development of a linear model based on equations initially derived by Matsuno (1966) for a shallow water, equatorial beta plane. Newtonian cooling, Rayleigh friction, and idealized heating were also included in the model. Zebiak (1982) expanded on the Gill (1980) model by parameterizing heating in accordance with SST anomalies. Zebiak and Cane (1987) further enhanced this linear Gill (1980) model by also including a low-level moisture convergence feedback developed by Webster (1981), improving its performance during the mature phase of ENSO. This modeling work culminated in the first successful forecast of El Nino by Zebiak (1986) which correctly predicted the 1986-87 El Nino, which was in stark contrast to the exceptionally strong 1982-83 El Nino that took the meteorological community largely by surprise (Barnston, 2016).

Observations and research related to sub-seasonal MJO variability and the oceanic Kelvin Wave were motivated by the extraordinary 1982-83 El Nino event (Barnston et al, 1997). This El Nino spurred the development of the Tropical Ocean-Global Atmosphere (TOGA) program (1985-1994), in which the primary mission was to study seasonal-interannual climate variability through utilization of both satellite remote sensing, and the

construction of an in-situ, moored buoy array, known as the Tropical Atmosphere Ocean (TAO) Buoy array that is still in operation to this day (McPhaden, 1993). Before TOGA, only isolated expeditions were conducted to study ENSO events (McPhaden, 2015).

Following the 1982-83 El Nino and success of the TOGA program, a renaissance of ENSO-related field and theoretical research followed, and it became apparent that ENSO's footprint on global climate variability was not exclusive to the tropical Pacific and adjacent landmasses. TOGA helped confirm pivotal early work by Bjerknes (1969) and Horace and Wallace (1981) which showed distinct, remote mid-latitude "teleconnections" (Angstrom, 1935) linked to equatorial SST anomalies in the Pacific via redistribution of heating and mass by anomalous convection fueled by zonal displacements in the Indo-Pacific Warm Pool.

Ensuing research revealed ENSO's impression on extratropical SST anomalies, via the "atmospheric bridge" mechanism (Alexander, 2002; Lau and Nath, 1996), global precipitation variability (Dai and Wigley, 2000; Diaz, 2001), global tropical cyclone activity (Gray, 1984; Kim et al., 2011; Zhao and Wang, 2019), the Pacific-North American (PNA) pattern (Renwick and Wallace, 1996), North and South Pacific Meridional Mode (NPMM and SPMM respectively (Vimont et al, 2003; Chiang and Vimont, 2004; Chang et al, 2007; Zhang et al, 2009; Larson and Kirtman, 2014; Zhang et al, 2014; Stuecker, 2018), and coral bleaching (McGowan et al., 2017; Claar et al., 2018). Connections between ENSO and global climate change have also been well documented (Trenberth, 1997; Gergis and Fowler, 2009), suggesting that ENSO has become significantly more active during the 20th century than any prior period in the last several hundred years and this is potentially a consequence of anthropogenic climate change.

More recently, analogous counterparts to ENSO have been extensively studied in the Atlantic and Indian Ocean. The Atlantic ENSO cousin is termed the Atlantic or "Benguela Nino" (Tokinga et al., 2019; Nnamchi et al., 2015; Nnamchi et al., 2016; Yadav et al., 2018; Lübbecke and McPhaden, 2017) and "Ningaloo Nino" in the Indian Ocean (Doi et al., 2013; Kataoka et al., 2014; Tozuka et al., 2014; Benthuysen et al., 2014; Marshall et al., 2015).

The development of simple, one or two-dimensional ENSO indices to characterize the state of the tropical Pacific coincided with the rise in research on ENSO during the 1980s and 90s, becoming a backbone for quantitatively diagnosing teleconnections. Rasmusson and Carpenter (1982) developed NINO indices (NINO 1 + 2, NINO 3, and NINO 4) based on ship tracks over the east-central equatorial Pacific, and with improved analyses as well as additional data, Barnston et al (1997) further defined the NINO 3.4 index as representing the "core" of ENSO-related SST anomalies in the equatorial Pacific. A graphical depiction of the NINO regions taken from the NOAA Climate Prediction Center (CPC) "El Nino Regions" page is shown in Figure 1.

The NINO 3.4 region was found to contain the strongest contemporaneous and lagged relationships with other ocean-atmosphere variables in addition to the most robust, holistic global teleconnections to precipitation and temperature patterns in the USA (Barnston et al., 1997). This motivated the creation of the widely-used Oceanic Nino Index (ONI) by NOAA CPC, which uses tri-monthly averaged SST anomalies in the NINO 3.4 region against a 30-year sliding base period that is updated every 5 years.

In addition to the NINO 3.4 index, the Multivariate ENSO Index (MEI) has become a widely-cited ENSO index (Wolter and Timlin, 2011). Version 1 of the MEI

(MEIv1) was defined as the first unrotated Principal Component (PC) of six combined, primary observed surface variables over the Equatorial Pacific Ocean (SST, surface air temperature, sea level pressure, meridional winds, zonal winds, and total cloudiness fraction of the sky) computed separately over 12 sliding bi-monthly seasons ranging from 1950 to 1993. By utilizing and integrating Principal Component Analysis (PCA) across multiple variables, this allows the components MEIv1 to vary with the seasonal cycle, and the inclusion of more variables (as opposed to using only SST or SLP) makes MEIv1 less susceptible to instrumentation and reconstruction errors that may be contained within individual variables from singular datasets. Therefore, MEIv1 is inherently more stable than other geographically fixed, univariate ENSO indices such as NINO 3.4 SSTs and ONI (Barnston et al. 1997; Ropelewski and Jones, 1987; Wright, 1989), the Southern Oscillation Index (SOI; Allan et al., 1991), and the Cold Tongue Index (CTI; Wright, 1989; Deser and Wallace, 1990).

The Extended Multivariate ENSO Index (MEI.ext; Wolter and Timlin, 2011) adapts the same methodology used for MEIv1 and extends the index backwards in time to range from 1871 to 2005. MEI.ext is defined by Wolter and Timlin (2011) as the combined, bi-monthly, leading principal component analysis (PCA) of Sea Level Pressure (SLP) and SST over the Tropical Pacific domain (30S-30N, 100E-100W) in the UK Met Office Hadley Centre SST dataset version 2 (HADSST2) (Rayner et al., 2006) and the UK Met Office Hadley Centre SLP Dataset version 2 (HADSLP2) (Allan and Ansell, 2006) datasets from 1871 to 2005. The exclusion of other variables used in the original MEI such as OLR, zonal and meridional wind, is largely attributed to the lack of data and datasets describing them before the early 1950s and satellite era.

MEI.ext has become widely used since its inception in 2011. The index has been utilized to study not only ENSO itself but, variability in the Northern Annular Mode (Quadrelli and Wallace, 2002; Fletcher and Kushner, 2011), stratospheric temperature changes in the satellite era (Randel et al., 2009; Fernandez et al., 2004), global sea level reconstructions (Calafat et al, 2014; Hamlington et al, 2011), hydroclimate variability in proxy tree-ring and coral records (Fowler, 2008; Wilson et al., 2010), marine heat waves (Zhang et al., 2017; Oliver et al., 2018), wildfire activity (Swetnam and Batancourt, 1993; Letnic et al, 2005; Harrison and Meindl, 2001; Fasullo et al, 2018), extreme weather events (Brönnimann et al, 2004; Jiménez-Muñoz et al, 2016; Santoso et al, 2017; Tangang et al, 2018), and climate sensitivity in GCMs (Zhu et al, 2007; Latif et al, 2015). MEI.ext (Wolter and Timlin, 2011), on which this thesis is largely based, has been extremely influential in the atmospheric science community.

Recently, a new version of the MEI (MEIv2) was released by the NOAA Earth System Research Laboratory (ESRL) using the 55-year Japanese atmospheric Reanalysis (JRA-55) (Kobayshi et al, 2015; Harada et al., 2016), but extends only from 1979 to present. MEIv2 uses the same ENSO regions as MEIv1, but unlike MEIv1, the input data for MEIv2 via JRA-55 is now spatially and temporally complete, alleviating the need for the spatial clustering step described in Wolter and Timlin (2011). Furthermore, the surface air temperature variable was removed, and cloud fraction of sky was replaced with outgoing longwave radiation (OLR).

In terms of the underlying observations of SST and SLP, three primary periods of contention and notable disagreement emerge: the period prior to the 1877-78 El Nino, and during the first and second World Wars. Disagreements amongst datasets in those

early periods is largely explained by a relative lack of data as there were few ships or more of their records were lost at sea or remain stored in archives (e.g. Freeman et al, 2016). The apparent discrepancy amongst available datasets in and around World War 2, however, also includes a shift in how SST observations were taken with many ships switching from insulated bucket to engine room intake (ERI) measurements of SST (Huang et al., 2016; Kennedy et al., 2011; Kennedy et al, 2019) as well as a paradigm shift(s) from mostly nighttime to day observations (Kent et al, 2013) (Figure 2).

These ERI measurements of SST were deemed to be safer to collect during wartimes than insulated canvas buckets and were spearheaded by the US (Kennedy et al, 2019). ERI was generally found to be biased high relative to bucket measurements due in large part to heating from the engine room (Kennedy et al, 2019; Carella et al, 2018; Huang et al, 2016; Kennedy et al, 2011; Thompson et al, 2008).

In addition to a significant loss of data during and immediately following World War 2, this previously overlooked source of discrepancy in the SST record due to a systematic bias in ERI measurements and how this is accounted for amongst datasets, including bias correcting ERI to HADNMAT2 (Huang et al, 2016), applying a mean bias correction (Hirahara et al, 2014), and providing a range of bias corrections (Kennedy et al, 2011), likely contributes a large fraction to the observed increase uncertainty between available datasets in this period (Figure 3). Datasets constructed before the discovery of this systematic bias in SST measurements (e.g. Kaplan et al, 1998), introduce additional uncertainty in any index that incorporates them into the calculations.

1.2 Objective

This objective of this thesis is to expand MEI.ext (Walter and Timlin, 2011) and develop what I am calling the Extended MEI Version 2 (MEI.extv2), an index that extends from 1865 to 2020, with methods that allow for semi-operational updates to the record as more data emerges. As was the case with the MEI.ext (Walter and Timlin, 2011), only SST and SLP will be utilized in the MEI.extv2, but since the release of MEI.ext in 2011, the number of SST datasets available has nearly doubled, and multiple revisions of the International Comprehensive Ocean-Atmosphere Data Set (ICOADS) - a core element of MEI.ext - have been released. Along with that, tens of millions of new observations in the 19th and 20th centuries have been compiled. A major update to the Extended MEI is warranted, and I describe several methodological updates that both improve the stability of the index and quantify uncertainty. My work is the first attempt to quantify ENSO magnitude using an ensemble of observationally-based and reanalysis datasets extending back to 1865, and the first attempt to quantify the corresponding uncertainty.

MEI.extv2 provides a number of improvements on the original COADS-based MEIv1, the MEI.ext, and the new JRA-55 MEIv2. I use an ensemble of observationally-based and reanalysis datasets, thereby quantifying structural uncertainties in MEI.extv2. I also institute various quality control measures for alterations in both the background climate and observational base states of the observed record in addition to an estimation of uncertainties.

The construction MEI.extv2 could be important for several different types of evaluation. The long (1865 to present) record of MEI.extv2 captures roughly twice as

many ENSO events as compared with ENSO indices that have been limited to the modern era (1950 to present). This allows for more robust statistics due to the larger number of ENSO events (Paul Roundy personal communication, 2017; Garfinkel et al., 2019). Because the MEI.extv2 is linked to multiple datasets and has quantifiable uncertainty, it also allows for investigation of multidecadal to centennial-scale ENSO variability, as well as what role anthropogenically induced climate change has played in modifying ENSO behavior.

The methodology to develop MEI.extv2 is only possible now because of the multitude of SST and SLP reconstructions and reanalyses that are available. We utilize monthly SST and SLP reconstructions and reanalysis datasets with a wide array of spatial and temporal scales (Section 2.1), and with the incorporation of multiple datasets (Sections 2.2-2.3), we quantify uncertainties in MEI.extv2 that arise from limits and artifacts in the observationally-based record (Section 2.4). The SST component of the MEI.extv2 uses 15 SST datasets, and the SLP component uses 14 datasets (Tables 1 and 2). In this thesis, we describe the input datasets and methods in Chapter 2, and discuss the results in Chapter 3, with conclusions and future work in Chapter 4.

CHAPTER 2: DATA AND METHODOLOGY

2.1 Input Dataset Selection and Processing

The original MEI.ext used only one dataset for analyzing both SST (HADSST2; (Rayner et al, 2006) and SLP (HADSLP2; Allan and Ansell, 2006). For MEI.extv2, we use 15 SST (Table 1) and 14 SLP datasets (Table 2) and a suite of statistical realizations for each dataset (Section 2.4). This multi-dataset approach is intended to increase the stability, robustness, and confidence in the MEI.extv2 and provide first order parametric and structural uncertainty estimates of the index. Similar analyses have been conducted by (McGregor et al, 2010; Compo et al, 2011) on other various modes of climate variability. To our current knowledge, MEI.extv2 uses more datasets than any other prior study and is the most up-to-date and comprehensive analysis of any climate variable using only observational reanalyses and reconstructions.

A multitude of Sea Surface Temperature (SST), Surface Air Temperature (SAT), and Sea Level Pressure (SLP) datasets were used to compute the MEI.extv2 (Table 1 and Table 2). These include the following: NOAA's 20th Century Reanalysis Version 3 (NOAA's 20CRv3) (Slivinski et al, 2019), Version 2c (NOAA's 20CRv2c) and Version 2 (NOAA's 20CRv2) (Compo et al, 2011), Centennial In-Situ Observation-Based Estimates of the Variability of SST and Marine Meteorological Variables Version 2 (COBE SST2) (Hirahara et al, 2014) and Version 1 (COBE SST) (Ishii et al, 2004), Extended Reconstructed Sea Surface Temperature Version 5 (ERSSTv5), (Huang et al, 2017) and Version 4 (ERSSTv4) (Huang et al, 2015), Kaplan's Extended SST Version 2 (Kaplan Extended v2) (Kaplan et al, 1998), United Kingdom (UK) Met Office Hadley Centre Sea Ice and Sea Surface Temperature Version 1 (HADISST) (Rayner et al, 2003),

European Center for Medium Range Weather Forecast (ECMWF) 20th Century Reanalysis (ERA-20C) (Simmons et al, 2016), ECMWF 20th Century Reanalysis Model (ERA-20CM) (Hersbach et al, 2015), Coupled ECMWF Reanalysis of the 20th Century (CERA-20C), National Centers for Environmental Protection/National Centers for Atmospheric Research (NCEP/NCAR) Reanalysis (Kalnay et al, 1996), Japanese Meteorological Agency (JMA) 55-year Reanalysis (JRA-55) (Kobyashi et al, 2015), Woods Hole Oceanographic Institute Objectively Analyzed air-sea Fluxes for the Global Oceans Version 3 (WHOI OAv3) (Yu et al, 2008), UK Met Office Hadley Centre Sea Level Pressure dataset Version 2 (HADSLP2) (Allan and Ansell, 2006) and Version 1 (HADSLP) (Basnett and Parker, 1997), Kaplan SLP (Kaplan et al, 2000), Jones and Climate Research Unit of East Anglia SOI (Jones/CRU SOI), (Ropelewski and Jones, 1987), Australian Bureau of Meteorology (BOM) SOI (Troup, 1965), and NOAA Extended Reconstructed SLP (NOAA ER SLP) (Smith and Reynolds, 2004). All of the NOAA 20th Century Reanalyses (v3, v2c, and v2), ERSST (v5 and v4), COBE SST, Kaplan v2, Kaplan SLP, HADSLP (v1 and v2), NOAA Extended Reconstructed SLP, NCEP-R1, and JRA-55 reanalysis data were all obtained from the NOAA Earth System Research Laboratory website. The European Reanalysis (ERA) datasets were all obtained from the ECMWF's Meteorological Archival and Retrieval System (MARS). WHOI OAv3 data were retrieved from the NCAR-UCAR Research Data Archive (RDA) webpage. SOI indices were obtained from the Australian BOM, and the University of East Anglia Climate Research Unit (CRU). Aside from Jones/CRU and Australian BOM SOI, only spatially and temporally complete datasets were considered for the MEI.extv2 in order to avoid the spatial clustering step used in the original MEI (Wolter and Timlin,

2011). Note, however, that spatial clustering was found to be unimportant in the construction of any version of the MEI, even for datasets like ICOADS or Hadley Centre Sea Surface Temperature (HADSST), which contain a large fraction of missing data points (personal communication, Klaus Wolter, 2017). All the aforementioned datasets are listed in Tables 1-2.

Similar to the construction of the original COADS MEI (MEI.v1) (Wolter and Timlin, 1993), Extended MEI (MEI.ext) (Wolter and Timlin, 2011), and JRA-55 (MEIv2) (Zhang et al, 2019), we used unrotated Empirical Orthogonal Function (EOF) analysis on each bi-monthly SST, SAT, and SLP dataset in (Tables 1-2) to construct the bi-monthly MEI.extv2. To calculate EOFs, we used the Koninklijk Nederlands Meteorologisch Instituut (KNMI) Climate Explorer developed by Geert Jan van Oldenborgh (Trouet and van Oldenborgh, 2013), and each EOF was detrended with spatial variability being normalized before any data was projected on it. Early in the development of the MEI.extv2, we found that dataset spatial resolution had little effect on the final MEI.extv2 index values, so before computing the 1st EOFs in KNMI, all datasets used in the construction of the MEI.extv2 were linearly interpolated to a 5x5° grid to maximize cross-dataset continuity and to speed up the processing time of computing the 1st EOF of each dataset. In addition, for a large proportion of the instrumental record, especially before the introduction of passive microwave satellite data in the mid 1970s, TAO buoy data beginning in the 1980s, and more dense ship coverage after 1950, the majority of 1x1° grid boxes in the datasets contained no observations before the late 20th century, often for several months at a time (or more), and thus any

advantage gained by using a dataset with a higher spatial resolution is considered futile for the 1865 to 2020 period in our analysis, and processing time significantly increases.

Another dataset processing choice in developing the MEI.extv2 is that we do not use a seasonally varying bi-monthly EOF. While for SST and SAT, the seasonal cycle in EOF "loadings" varies little over the course of the year, we found that in nearly every SLP dataset (aside from HADSLP2, which was utilized in MEI.ext), the Tropical Pacific SLP EOF1 and Tropical Pacific SLP EOF2 "swap" during the mid-late northern spring (~April-May) through the late boreal summer (~August-September) (Figure 4). Early in the construction of the MEI.extv2, we decided that a more stringent investigation of this EOF swap, and why it occurs in some SLP datasets and not others, needs to be conducted but that the details were outside the scope of our objectives. For our calculations, the impact of the EOF swapping is that the dominant EOF loading can itself affect comparisons across datasets. Moreover, it is also not necessarily guaranteed or clear at this current juncture that the boreal summer Tropical Pacific SLP EOF2, which bears some semblance to EOF1 during the boreal winter, are actually part of the exact same phenomena. The work-around is simple: we exclude a seasonally varying bi-monthly EOF in developing the MEI.extv2 and instead, we use a 5-month pentad of the leading EOF of SST and SLP for October-February (ONDJF). This choice allows us to make a more valid comparison between the more stable leading SST and SLP EOFs. The stability in the dominant EOF is a result of the time of the year when ENSO's footprint in the Tropical Pacific and global circulation is typically the most robust. The methodological choice strengthens the similarity across datasets and avoids what a inter-dataset artifact that is difficult to reconcile. We assert that our methods to quantify

uncertainty described below account for inter-dataset variability far more directly, even without the seasonally varying EOF.

The SAT EOF1 loading pattern in the Equatorial Pacific is nearly identical to the SST EOF1 loading pattern (Figure 5), which was also concluded by Wolter (1993) and Wolter and Timlin (1998). The MEI.v2 index (Zhang et al, 2019) excludes SAT from its analysis for this very reason because the SST and SAT PC time series in the JRA-55 reanalysis are so closely correlated that including both in the index would be the near equivalent of double weighting. The strong correspondence between the two time series is expected given the coupling that occurs between the sea surface and overlying atmosphere in direct contact with it. Thus, in the MEI.extv2 all datasets which produce SST or SAT are included and lumped under the "SST" umbrella and herefore will be referred as such throughout the rest of this paper. Moreover, including SAT in addition to SST allows the MEI.extv2 to include several more datasets to constrain the SST component of the MEI.extv2, which is critical to obtaining a more reliable estimate of the MEI.extv2 and a concomitant estimate of uncertainty.

All periods used to "train" the EOFs for each dataset in the MEI.extv2 begin in 1876 due to higher uncertainties and spread amongst available datasets prior to that year. As discussed in Section 2.4, we also found in the uncertainty analysis of the MEI.extv2 that the period of the instrumental record preceding the 1877-78 El Nino that very few, if any ENSO events could be gleaned with any substantial confidence from the available data, which is a testament to the large uncertainties that exist in this portion of the observed record also shown in (Figures 3 and 6).

Similar to Wolter and Timlin (2011), we included pre-1950 data to compute the leading EOFs to stabilize the EOF loadings. Certainly, the 1876-1950 period is susceptible to higher uncertainty than the post-1950 period, but including the 1876-1950 period effectively doubles the sample size of post-1950 or satellite-era (1980-present) data in the EOF calculations, making the EOFs more robust to the addition or removal of a subset of years or slight alterations to the EOF region. Furthermore, many datasets used in the MEI.extv2 in their construction make the inherent assumption that post and pre-1950 ENSO behavior are exactly alike (Rayner et al, 2003; Huang et al, 2014; Huang et al, 2017).

The MEI.extv2 loading region for both the SST and SLP EOFs are spatially confined below 20 degrees north in the Pacific basin with regions as follows: SLP [100E-80W, 30S-20N], SST [160E-80W, 20S-15N]. Keeping both regions equatorward of 20N minimizes overlap between the ENSO EOFs and the Pacific Decadal Oscillation which is traditionally defined as the leading mode of SST variability poleward of 20N in the North Pacific Ocean (Mantua et al, 1997; Zhang et al, 1997). The longitudinal bounds for SLP remain the same as the original MEI.ext (100E-80W) but the latitudinal extent is confined to 20N-30S (Figure 7). The meridional asymmetry in the SLP EOF reflects one of the well-documented asymmetries in ENSO (hence the name “Southern Oscillation”). The EOF region for SST was further narrowed to 15N-20S, 160E-80W in developing MEI.extv2 to capture more variance exclusive to the cold tongue region of the equatorial pacific, while the asymmetry in the EOF region here is a reflection of slightly higher EOF loadings displaced in the tropical and subtropical Southern Hemisphere (Figures 8-9). All

of these changes are intended to improve how the leading SLP and SST EOFs capture ENSO variability in the tropical Pacific.

Along with unrotated PCA, another customary way to quantify ENSO variability is to use box-averaged SST or SLP. This is done for NINO 1-2, NINO 3, NINO 4 (Rasmussen and Carpenter, 1982), NINO 3.4 (Barston et al, 1997), and the Cold Tongue Index (Wright, 1989; Deser and Wallace, 1990). Unrotated PCA/EOF analysis and box-averaged indices are the two most common methods used to derive climate indices and each possess their respective advantages and disadvantages.

Unlike all other versions of the MEI (MEIv1, MEIv2, MEI.ext) as well as other ENSO indices, we developed MEI.extv2 to assess the influence of both EOF loading regions and box-averaged regions in our analysis. For SST, we choose a box region that is more spatially confined than the EOF region and analogous to the Cold Tongue Index (Wright, 1989; Deser and Wallace, 1990) [5S-5N,180W-80W]. For SLP, we chose to replicate the SOI (Allan et al., 1991, Ropelewski and Jones, 1987, Troup, 1965) by choosing the nearest grid box to Darwin, Australia [12.5S, 130.8E] and Tahiti, French Polynesia [17.7S, 149.4W] in each SLP reanalysis dataset to make their corresponding time series more comparable to the Jones/CRU and Australian BOM SOI indices. While the SOI is among the noisiest ENSO indices available to date, the inclusion of the SOI and corresponding reconstructions from Jones/CRU and Australian BOM help improve the robustness of the MEI.extv2. Unlike the overwhelming majority of sea surface observations that comprise the major SST and SLP reconstructions and reanalysis used in the MEI.extv2, these SOI reconstructions include surface-based, stationary, and bias corrected sea level pressure measurements taken nearly continuously through the mid-late

19th century at both Tahiti and Darwin, with intercomparisons having been made between the observations taken at these sites to other nearby observing stations with long observing records such as Madras, Suva, and Fiji (Ropelewski and Jones, 1987) to ensure their quality. However, we argue that it is also important to accompany these reconstructions with reanalysis datasets that include observations beyond these stationary observing sites to fully assess the basin-scale structure of ENSO's atmospheric component. Given the larger inherent variability in the singular point or grid box-based SOI from BOM and CRU, we rescaled those SOI time series to values ranging from -4 to +4 to make them more comparable to those of SLP EOFs that are determined from a large tropical Pacific spatial domain.

While EOF loading may better capture ENSO in many instances as compared with box-averaged data (e.g. NINO indices: Rasmusson and Carpenter, 1982; Barston, 1997) due to its inclusion of variability over a wide geographical area and accounting for the total spatial structure of the field (Roundy, 2015), there are cases where box-averaged indices coincide with points in space that are better constrained by verifiable surface observations and contain a larger fraction of grid boxes with actual data. Box-averaged domains also preserve physical units (as opposed to EOFs), and can aid in providing a focus on a particular aspect of ENSO. Our analysis directly tests the sensitivity of our MEI.extv2 ENSO index to the analysis choice of an EOF loading region or a box-average region, and our methods could be used to gain insight into the trade-offs in using one or the other to determine the overall SST and SLP. We discuss the results of this choice in Chapter 3, and in particular, we explore the period before 1950 when observational

density of both SST and SLP are markedly lower and are sensitive to the choice of an EOF or a box-average region.

2.2 Ensemble Member Creation from Input Datasets

To provide a statistically robust ENSO index with the added capability of providing first-order uncertainty estimates, a large suite of MEI.extv2 "ensemble members" or realisations were constructed for the bi-monthly SST and SLP EOFs from each of the 29 input datasets. For context, MEI.ext (Wolter and Timlin, 2011) used one base period (1871-2005) and a single dataset for both SST (HADSST2) and SLP (HADSLP2), resulting in only two possible values for the MEI during any given bi-monthly period. This limited the result to a best estimate, but with no estimate of uncertainty. For MEI.extv2, however, we build out thousands of possible MEI.extv2 values or "realizations" for each of the contributing SST and SLP datasets. This allows us to explore a deeper statistical landscape and better quantify both the best estimate of center for each dataset, as well as the best estimate of confidence intervals. The intent is to develop our 150 year ENSO index so that we can maximize the robustness to outliers in individual datasets, and we can quantify the effects of changing base period length, location, and frequency on the bi-monthly measure of center and the corresponding confidence intervals.

To build a large suite of realisations for the MEI.extv2, we consider several sources of parametric uncertainty in our analysis. Namely, our choices of the measure of central tendency, climatological base period length, base period updating frequency, as well as base period juxtaposition, and we apply this to both the PC1 and box-averaged time series for both SST and SLP.

The six measures of central tendency chosen here are: mean, median, tri-mean, mid-hinge, 20% trimmed mean, and winsorized mean. Unlike a standard mean value, tri-mean provides a weighted average of the median and 2 quartiles, with twice as much weight given to the median, whereas a trimmed mean calculates the standard mean but discards a specific subset of the distribution that is deemed to be "extreme". Here, 20% is chosen as a reasonable value for the trimmed mean as it effectively eliminates strong ENSO events from significantly influencing the climatological base periods, and also leaves enough remaining years for shorter-length base periods to have somewhat stable and robust values with which to define ENSO. Winsorized mean is analogous to the trimmed mean, with the only difference being that the aforementioned "extreme" values are not completely discarded, rather, they are replaced with the most deviant remaining values. The mid-hinge on the other hand is a complement to the interquartile range, and is the average of the first and third quartiles in a particular distribution. The utilization of these other measures of central tendency in addition to median and mean provide a more realistic, dispersive sample distribution and envelope of uncertainty during each bi-monthly period.

Three choices of climatological base period length are utilized: thirty, forty, and fifty year-long base periods. While the World Meteorological Organization (WMO) and central limit theorem generally dictate that 30-year base periods are of sufficient length to produce statistically robust and coherent climatological periods, we also extend this to forty and fifty-year periods as natural multidecadal variability and a few very intense ENSO events over the course of a few decades, (as was observed in the 1980s and 1990s) or lack of ENSO activity for several years (or more) can add significant skew to the

climatological base periods and make them less representative of the underlying, basic state climate, especially for measures of central tendency, like the mean, that are not robust to outliers. This choice to also introduce forty and fifty-year base periods also inherently means that for the lattermost part of the MEI.extv2 record may possess a bias that slightly favors El Nino events as the basic state climate has been given more time to change (i.e. warm) over the course of forty or fifty years as opposed to thirty, however, this problem is inherent in basically any ENSO index or even measure of global temperature anomalies, as the base state climate of 2020 is certainly significantly warmer than the 1981-2010 climate reference period that is frequently used (Cheng et al, 2019), (Cheng et al, 2020), (Blunden and Arndt, 2019).

Three choices of base period updating frequency are analyzed here: one, five, and ten years. Although NOAA's Oceanic Nino Index (ONI) uses a thirty-year sliding base period updated every five years, at times, this base period may not be the best choice to use for a climatological period as there may be more discontinuities, irregularities, and noise in using a base period that updates every five years as opposed to say ten years. It is also legitimately possible that the immediate climate fallout from extreme climate events, such as the 1997-98 El Nino that may not be effectively captured by using a base period that updates every five years and may require a more frequently updating base period to demarcate very specific points in the record where there were large, permanent, upward step changes in global temperature as we have observed in the satellite-era following the 1997-98 and 2015-16 El Nino events, wherein nearly every year following the El Nino was warmer than all years prior to the El Nino (Mears and Wentz, 2017; Lensenn et al, 2019; GISTemp Team, 2020).

Nine choices of base period juxtaposition are used to quantify sensitivity of values to the particular climatological base period in the context of other neighboring climatological base periods. In our analysis, for a thirty, forty, and fifty-year period, the 16th, 21st, and 26th values respectively are where the climatological base period is centered upon. For thirty year base periods, this center value then varies from the 16th element of a 30 year period by +/- 1, 2, 5, and 10 years, while 40 and 50 year base periods use +/- 5, 10, 15, 20 and +/- 10, 20, 30, and 40 years respectively. The larger intervals for larger base periods is intended to reflect similar changes to the climatological base period as a function of juxtaposition with 30-year base periods, due to differences in length and stability in these larger base periods. The intention of this is to provoke more dispersion between MEI realisations, as it was found in the data processing steps that using +/- 1, 2, 5, and 10 years for each base period length resulted in time series for 40 and 50 year base periods that were almost exactly the same regardless of central tendency and updating frequency.

All of these aforementioned choices of varying central tendency and climatological base periods are applied across both the PC and box averaged input time series and each realisation is linearly detrended to help create nearly 1,000 possible detrended MEI.extv2 realisations for each individual dataset at every bi-monthly time step and over 26,000 from 1958 to 1997, when every dataset in our analysis overlaps. The structure of the MEI.extv2 realisations are as follows: the first member of each dataset is a 30-year mean, updated every year with a juxtaposition shift of -10 years applied to the original input EOF time series. Members 2-9 then follow as 30-year means with the rest of the aforementioned juxtaposition tweaks in the following order:-5, -2, -1, 0, 1, 2, 5,

and 10. Members 10-18, 19-27, 28-36, 37-45, and 46-54 use the same base period length, updating frequency, and juxtaposition tweaks but now instead use median, tri-mean, mid-hinge, 20% trimmed mean, and winsorized mean respectively. This structure then repeats, with 30-year base periods updated every 5 years, 30-year base periods updated every 10 years, 40-year base periods updated every year, 40-year base periods updated every 5 years, etc. Then the same procedure is replicated for the input box-averaged time series to generate twice as many realisations for each dataset, with a few exceptions (Section 2.1).

Each of the EOFs for SST and SLP is then determined from the median of all ensemble members available at a given bi-monthly period. We do not use the mean value because, while the very large number of members might imply that the distribution across datasets is perfectly normal, this is not necessarily true, as the inter-dataset variability tends to drive the differences across datasets. Outlier datasets even with a very large set of MEI.extv2 realisations, may still result in significant skewness in some bi-monthly periods. Utilizing the median value as we do here preserves a little additional amplitude in the final MEI.extv2 output that may be lost due to spread and uncertainty across datasets. We also utilize these ensemble members to provide a crude measure of the probability for a particular phase and intensity of ENSO in each bi-monthly period. The analyzed median value and most likely ENSO phase often agree (~80% of the time).

Finally, we note that other sensitivity tests were performed including varying dataset resolution and projecting each dataset on other dataset EOFs, but this yielded very little, if any measurable dispersion and additional uncertainty in the MEI.extv2 value, even in the context of possible random errors that may arise in processing.

2.3 Weighting Factors for SST and SLP EOFs

A distinction between the MEI.ext (Wolter and Timlin, 2011) and MEI.extv2 is that the SST and SLP are not weighted equally in the index. We describe here the individual components that comprise a time-varying weighting equation and we also highlight why unequal weighting of SST and SLP is critically important for the MEI.extv2.

First, unlike the MEI.ext and MEI.v2, the EOF regions of SST and SLP are not of equal size, therefore the Lorenz (1956) assumption made in Wolter and Timlin (2011) which posits that both fields may be weighted equally in combined PCA, is not valid here, and leads to differences in explained variance, or the ratio of first EOF eigenvalue against all eigenvalues of the between the SST and SLP EOFs. Also, even if similar regions are used, there will certainly be at least some modest differences in the explained variance between SST and SLP (Figure 10) and thus they need to be properly accounted for in any ENSO index that uses both variables. Here, the explained variance between the two datasets will be expressed as a ratio of the average percentage of datasets available for both SST and SLP. Thus, the value of explained variance will vary with time as datasets for either SST or SLP are added or removed. Generally, we find that the average explained variance for SST datasets are approximately 20% greater than for SLP.

Second, the number of datasets we use in our analysis (Figure 11), and the spread across those datasets for SST and SLP as a function of time are different (Figures 3 and 6). The number of datasets for both SST and SLP increase as a function of time, although not at the same rate (Figure 12). There are as many if not more SST datasets at any given time in the entire MEI.extv2 record than there are SLP datasets. This gap between the

number of SST and SLP datasets is even larger near the beginning and end of the MEI.extv2 time series where more of the SLP datasets are absent or drop-out completely. Furthermore, to properly account for this ratio, the square root of the total number of datasets for each variable is taken because the relative impact of providing each additional dataset when the total number of datasets is already fairly high will be less than if the total number of datasets were initially closer to zero. The introduction of a square root to consider "n" number of datasets is analogous to the calculation of standard error, where the sample standard deviation is divided by the square root of the number of samples. We find that the impact of including the ratio of the number of datasets in the MEI is comparable to explained variance, whose magnitude is descriably a second-order term in the weighting equation.

Third, the number of observations associated with the data sources (mostly ICOADS) that provide the input or boundary conditions to reanalysis models and statistical reconstructions are different between SLP and SST (Figures 13-15). This is important because the number of available observations underlying each dataset is closely related to the structural uncertainties amongst available datasets at a particular portion of the record, as well as the quality and reliability of the data that is being analyzed. Here, we express the number of SST and SLP observations as observational density, or the number of observations per 2x2° grid box. As shown in Figures 13-14, SST and SLP observations in ICOADSR3.0 generally increase over the course of the record, but this increase is not constant. For example, in Figure 13, it is apparent that a major dropout in both SST and SLP observations occurred during and immediately following World War 2, which lasts to about 1950. This is primarily due to the

destruction of ships during the war, which leads to substantial increases in uncertainty during this part of the instrumental record, because nearly all of the sea surface observations prior to the late 20th century are collected via voluntary observing ships (VOSs) (Woodruff et al, 2011; Freeman et al, 2017; Kennedy et al, 2019). Furthermore, a pronounced local peak in surface observations occurs in the mid-late 1880s, providing comparable observational coverage to the early 1950s. This peculiar local maximum in surface observations is mainly due to the addition of 2 million US Marine Meteorological Journal reports in ICOADSR2.5, which has permeated into later versions of ICOADS and these reports contain critical information about the diurnal cycle of SST and SLP observations (Woodruff et al, 2011; Freeman et al, 2017), lending slightly more credence to data in this period in some of the datasets analyzed here.

We also find that for most of the instrumental record, SLP observational density is generally higher than SST, until the mid 1980s, where the introduction of moored TAO buoy data as part of the TOGA program leads to SST possessing an observational density that is roughly three times higher than SLP after 1985. Moreover, the impact of observational density on the weighted MEI is larger than either explained variance or dataset number combined, and is therefore a first-order term in the weighting equation.

Finally, the last term that is considered here for a weighted MEI is the spread amongst available datasets for both SST and SLP, or inter-dataset spread, denoted as the standard deviation of the output between datasets. This quantity is measured as an inverted ratio between SST and SLP, because larger spread between datasets of SST or SLP implies larger uncertainties and lower confidence in that particular variable and it . While the spread in available datasets certainly does not explicitly represent

observational uncertainty, the structural uncertainties involving how the assumptions made by each institution in how the data is reconstructed, filled, and filtered in each dataset, are inherently related to and partially represent observational uncertainties that underlie each dataset's input data. Furthermore, this inter-dataset spread, which is often referred to as structural uncertainty, is arguably the most elusive and poorly understood of the sources of uncertainty that are interwoven into the observational record (Kennedy, 2014). In addition, Compo et al (2013) compared surface thermometer records to reanalysis products, and found that the differences between the respective datasets were larger than would be expected from the individual dataset's ensembles. This suggests that analyzing uncertainty in a single dataset with perturbed ensemble members may significantly underestimate the "true" uncertainty in the data and may be inherently underdispersed. However, inter-comparisons between a wide array datasets as we do here, may actually provide a reasonable lower bound on the "true" uncertainty (Parker, 2016).

This analysis, which uses a multitude of SST and SLP datasets (Section 2.1) and statistical variations in "realizations" of each dataset (Section 2.2) provides the most complete and up-to-date estimate of structural uncertainty. Increases in spread in either SST or SLP relative to the other are indicative of lower confidence in that respective principal component (PC) or box-averaged time series, and that variable is weighted less in our calculations of bi-monthly MEI.extv2.

We find here that inter-dataset spread is a leading order term in our weighting equation, accounting for ~45% of the total weight in the weighting equation (Figure 16), and is nearly twice as large as contribution from observational density, with SST dataset

spread being on average, ~65% lower than SLP datasets (Figures 17-18). Akin to observational density, inter-dataset spread (Figures 3 and 6) does not monotonically decrease with time. Rather, we find that there are significant periods, namely during and immediately after World War I and II, where major dropouts in observations and/or systematic changes in how the observations were collected lead to increases in spread, particularly for SST. These include the switch from insulated buckets to engine room intake to measure SST (Kennedy et al, 2019; Carella et al, 2018; Huang et al, 2016; Kennedy et al, 2011; Thompson et al, 2008), the time of day the observations were obtained, and differences in methodology between datasets on how to reconcile these sources of uncertainty. All of these are incorporated differently in the individual datasets and increase inter-dataset variability. We interpret Inter-dataset variability as an integrated measure of the multiple ways data are ingested into the individual reanalyses.

The aggregate effect of (1) 1st EOF explained variance, (2) number of datasets, (3) observational density (number of observations per 2x2 grid box (via ICOADS R3.0), and (4) inter-dataset spread (σ) is captured in our calculation of the time-varying bimonthly values of MEI.extv2 and the uncertainty. MEI.extv2 is calculated as a linear combination of the time-varying EOFs or box-average determined indices of SST and SLP (E_{SST} and E_{SLP}) per

$$MEI.extv2 = \frac{S*E_{SST}+P*E_{SLP}}{S+P} \qquad (1)$$

where S and P are the time-varying weighting factors, noting that when $S = P$, then the calculation is a straight average, but usually $S \neq P$ as we discuss below. The weighting factors S and P in Equation 2 are

$$\frac{S}{P} = \frac{EV_{SST} * \sqrt{N_{SST}} * \sqrt{O_{SST}} * \sigma_{SST}^{-1}}{EV_{SLP} * \sqrt{N_{SLP}} * \sqrt{O_{SLP}} * \sigma_{SLP}^{-1}} \qquad (2)$$

where EV represents the explained variance (as a fraction), N the number of datasets, O the observational density, and σ the spread between datasets calculated as the standard deviation, and the subscripted SST and SLP indicates that the term refers to SST and SLP datasets, respectively. For example, N_{SST} is the number of SST datasets contributing to a particular bi-monthly time period in the data and ranges from zero to 16 (per Table 1), while N_{SLP} ranges from zero to 14 (Table 2). Finally, note that all terms in Equations (1) and (2) are time-varying.

The observational density and inter-dataset spread terms dominate the weighting equation, contributing over 70% of total weight in the weighting equation with explained variance and dataset number providing smaller contributions of about 15% and 10%, respectively. Observational density weighting can force S or P to zero if there are bi-monthly periods without any surface observations, as is the case for SST prior to 1870.

The percent of the total weight constituted by SST and SLP shown in (Figure 18) shows that SST is weighted roughly twice as much as SLP, meaning that the MEI.extv2 index is comprised of about 70% SST and 30% SLP. A majority of this discrepancy comes from the inter-dataset spread term in SST, although explained variance and dataset number make smaller, additional contributions, with SST dataset spread, as aforementioned, being nearly half of SLP dataset spread on average. This larger relative inter-dataset uncertainty between SLP datasets relative to SST likely emerges for several reasons. The slightly smaller number of datasets makes it more difficult to adequately constrain the inter-dataset spread term. The inherent nature of SLP is also a potential

source of additional spread, as this field is spatially and temporally fraught with more atmospheric “white noise” (Trenberth, 1984; Kawamura et al, 1998; Wu and Huang, 2004) and potentially more uncertainty per capita on a bi-monthly scale compared with SST. The introduction of an SOI index whose box-averaged region in each dataset is proportionally smaller than the large basin-wide SLP region as compared with the SST EOF and box-regions, and furthermore, the SOI index is likely to be riddled with appreciable more noise as it only represents a singular grid box in the SLP datasets. Also, it is worth pointing out of the SST and SLP datasets used here, the SLP datasets are on average nearly a decade older than the SST datasets. Hence, the SLP data may be predisposed to be of lower quality than the SST data, as many of the older SLP datasets may use outdated methods of reconstruction and bias corrections to the data, relative to SST.

2.4 MEI.extv2 Uncertainty

Unlike the MEI.ext, a novel contribution of this work is to provide first-order uncertainty estimates to establish confidence intervals in the monthly MEI.extv2 values. In the MEI.extv2, uncertainties between most of the aforementioned weighting factors of SST and SLP are assumed to be relatively independent and therefore are added in quadrature, but we account for the unequal weighting and moderate covariance (Beven, 2013) in the uncertainty in our estimate of uncertainty as well. We find that the largest source of uncertainty for MEI.extv2 is the structural uncertainty among datasets, as represented by inter-dataset spread (Section 2.3). Parametric uncertainties from our choice of climatological base period (Section 2.2) have a small impact on the total uncertainty. However, it was found that inclusion of this parametric uncertainty term

leads to an unrealistic time evolution of total uncertainty that does not exhibit a downward trend as would be expected from the inclusion of more datasets, more observations underlying the datasets, and higher quality observations later in the record, especially after 1950.

Moreover, we discovered during the data processing stage of the MEI.extv2, that inter-dataset spread between SST and SLP were weakly-to-moderately correlated. This result is anticipated given that many reanalysis products, such as the NOAA 20th Century Reanalysis and ECMWF 20th century Reanalysis products are used to analyze both SST and SLP for the MEI.extv2. Also, some reanalysis datasets use SST or SLP reconstructions to provide boundary layer input for their reanalysis models, as is the case with NOAA's 20th Century Reanalysis Version 2 using HADISST to prescribe SSTs (Compo et al, 2011).

The time-dependent MEI.extv2 uncertainty is calculated by considering a function of two variables with unequal weights (e.g. Bevan, 2013) as

$$f = w_x x + w_y y \tag{3}$$

where w_x and w_y are the weighting factors for a function f that depends on two variables x and y, with known standard deviations σ_x and σ_y. Uncertainty in Equation (3) is calculated based on the weighting factors and the uncertainties in x and y, and accounts for correlation in σ_x and σ_y and propagated in quadrature as

$$\sigma_f^2 = \left(\frac{\partial f}{\partial x}\sigma_x\right)^2 + \left(\frac{\partial f}{\partial y}\sigma_y\right)^2 + \frac{\partial f}{\partial x}\frac{\partial f}{\partial y}COV(x, y) \tag{4}$$

where $\frac{\partial f}{\partial x}$ and $\frac{\partial f}{\partial y}$ are the partial derivatives and $COV(x,y)$ is the covariance of x with y. Recognizing that $COV(x,y) = r_{x,y}\sigma_x\sigma_y = r_{y,x}\sigma_y\sigma_x$ where $r_{x,y}$ is the Pearson correlation coefficient and that $r_{x,y} = r_{y,x}$ then we can write

$$\sigma_f^2 = \left(\frac{\partial f}{\partial x}\sigma_x\right)^2 + \left(\frac{\partial f}{\partial y}\sigma_y\right)^2 + 2\frac{\partial f}{\partial x}\frac{\partial f}{\partial y}r_{x,y}\sigma_x\sigma_y \quad (5)$$

Applying weighted error propagation (Bevan, 2013) in Equation (5) to Equation (1)

$$\frac{\partial(MEI.extv2)}{\partial E_{SST}} = \frac{S}{S+P} \quad (6)$$

$$\frac{\partial(MEI.extv2)}{\partial E_{SLP}} = \frac{P}{S+P} \quad (7)$$

$$\sigma_{MEI.extv2} = \sqrt{\left[\frac{S}{S+P}\sigma_{SST}\right]^2 + \left[\frac{P}{S+P}\sigma_{SLP}\right]^2 + 2\frac{SP}{(S+P)^2}r\sigma_{SST}\sigma_{SLP}} \quad (8)$$

where r is the Pearson correlation coefficient of the standard deviations of σ_{SST} and σ_{SLP} and was calculated to be $r = 0.326$. We report uncertainties in the bi-monthly $MEI.extv2$ ($U_{MEI.extv2}$) as the 90% confidence interval such that

$$U_{MEI.extv2} = 1.645 * \sigma_{MEI.extv2} \quad (9)$$

noting that all terms are time-varying.

As shown in Figure 20, the MEI.extv2 uncertainty generally decreases over time, with local peaks in uncertainty during and immediately following the two major World Wars as also noted by (Kennedy et al, 2011; Kennedy, 2014) in addition to some smaller, yet notable peaks during the height of the 1982-83 and 1997-98 El Ninos. The 90% (~1.6σ) confidence interval was utilized here in favor of a more traditional 95% (~ 2σ) confidence interval. While we have not found spread to be dependent on intensity, the most extreme El Ninos in the modern (post 1950) era (1982-83, 1997-98, 2015-16) exhibited behavior that would suggest that in the most exceptional ENSO events which

occur with appreciably less frequency than other ENSO types, and are therefore apt to be less adequately constrained by observations, do exhibit some intensity dependent behavior due to spread in both SST and SLP. In addition to these extremely intense ENSO events being potentially poorly constrained by observations and therefore exhibiting larger uncertainties amongst available datasets, the raw standardized, unit less values of SST and SLP simply being larger than in any other part of the record may also lend itself to producing larger spread amongst available datasets during the height of these El Ninos.

Furthermore, it was deemed that the 95% interval was too conservative, particularly during the modern portion of the record. For instance, during the height of the 1997-98 Super El Nino, which has been often dubbed the "climate event of the century" (Broad, 2002), the lower bound of the 95% confidence interval specifically in the Nov-Dec 1997 bi-monthly period, dipped below the "Super" El Nino threshold, meaning that for this particular winter, it was legitimately possible that this El Nino was not within the top 5 of historical El Nino events. This is deemed to be unreasonable as the available datasets during this time period are very well constrained by a multitude of observing platforms with higher quality data per capita, and a host of corroborating evidence from other popular ENSO indices (SOI (Ropelewski and Jones, 1987), ONI (Barnston et al, 1997), BEST (Smith and Sardeshmukh, 2000), the original MEI.ext (Wolter and Timlin, 2011), COADS MEI (Wolter and Timlin, 1993), MEI.v2 (Zhang et al, 2019 suggests 1997-98 is easily among the strongest El Nino events on record during the fall of 1997 into the winter of 1997-98. Similarly, during February-March 1983 near

the height of the prolific 1982-83 El Nino, the lower bound of the 95% confidence interval dipped below the “Super” El Nino threshold.

The changes discussed above to the MEI.extv2 in the context of all other versions of the MEI are summarized in Table 3.

2.5 ENSO Definition

ENSO was defined here using an analogous percentile distribution to Wolter and Timlin (2011) and is shown in Table 4 and Figure 21. El Ninos, Neutral, and La Nina were generally assumed to each occur roughly one-third of the time, however unlike Wolter and Timlin (2011), the ranks are flipped such that El Ninos occupy the lowest ranks and La Ninas the highest, we use all bi-monthly periods to rank ENSO instead of individual bi-monthly periods, and the El Nino and La Nina thresholds correspond to the lower tercile (33%) and uppermost tercile (67%) respectively as opposed to the end of the 3rd decile (30%) and beginning of the 7th decile (70%), which does not change the conclusions we draw here, although it increases the detectability of ENSO events ever-so-slightly in MEI.extv2 over MEI.extv1. The distribution of El Nino and La Ninas using the aforementioned ENS ONI with NOAA CPC’s definition of 5 successive tri-monthly periods greater than or equal to +/-0.5C, found that La Nina and El Nino occur 31% and 32% of the time respectively. Therefore, the choice of ENSO threshold here is well within reason and similar to other popular ENSO indices and previous published studies.

Thus, going by our definition of ENSO, El Ninos occur when the MEI.extv2 bi-monthly values are in the top 33% of all MEI.extv2 values (regardless of bi-monthly period), while Neutral ENSO and La Nina correspond to the middle third and lower third of bi-monthlies respectively. Further distinctions to denote Weak, Moderate, Strong, and

Super (very strong) ENSO events were also made here as was done with MEI.ext and MEI. Similar to Wolter and Timlin (2011), moderate El Ninos and moderate La Ninas were assumed to be ongoing when the MEI.extv2 bi-monthly percentiles were in the 2nd (10-20%) and 9th deciles (80-90%) respectively. Also similar to Wolter and Timlin (2011), the minimum threshold for Strong El Nino and Strong La Nina is defined as the 10th and 90th percentiles respectively.

A further distinction is made to identify extraordinarily powerful El Nino and La Nina events. The motivation for this is attributable to the fact that 4 very intense El Nino events (1877-78, 1982-83, 1997-98, 2015-16) are all more intense than not only any other El Nino, but all other ENSO events in the observed record (Table 5). Furthermore, all of these El Ninos events have triggered exceptionally large and widespread climate anomalies across the globe, and the term “Super El Nino” has become increasingly popular and acceptable nomenclature in the atmospheric science community (Hameed et al, 2018; Zhu et al, 2018; Bing and Xie, 2017; Chen et al, 2016a; Hong, 2016; Latif et al, 2015).

The 1877-78 El Nino is regarded as among the most intense of the mid-late 19th century, triggering global temperature anomalies that were more than twice the amplitude of any other major El Nino event from 1865-2014 after removing a 30-year mean in Hadley Centre/Climate Research Unit Temperature Version 4.6 (HADCRUTv4.6; Morice et al, 2012) as shown in Figure 22 (motivated by Aceituno et al, 2009). This El Nino was connected to the warmest winter ever observed in the post-settlement era in portions of the upper midwest of the US and south-central Canada (Aceituno et al, 2009), and was of comparable magnitude to El Ninos in 1982-83 (Kiladis and Diaz, 1986) and

1997-98 (Grove, 1998; Huang et al, 2020) (also see Table 5). It was also attributed to a cataclysmic global famine that killed 3% of the world's population, with the population in some provinces of China for instance, not fully recovering to pre 1877-78 El Nino levels until the mid-1950s (Davis, 2002).

Super El Ninos in the 20th and 21st centuries were associated with major documented impacts, but also responses by the scientific community. The 1982-83 event spawned a cascade of ENSO research in the late 20th century and served as the catalyst for the creation of the Tropical Atmosphere Ocean (TAO) project to detect similarly intense El Ninos considerably sooner (McPhaden et al, 2015) and the first successful forecast of El Nino (Cane et al, 1986; Barnett et al, 1988). The 1997-98 El Nino event was arguably the most intense of the 20th century and is regarded as the "El Nino/climate event of the century" (Slingo and Annamalai, 2000; Broad, 2002), spurring the creation of seasonal forecasts (Barnston et al, 2010). The 2015-16 El Nino also ranks among the Super El Ninos and is clearly the most intense El Nino of the 21st century thus far. For more on corresponding bi-monthly, percentiles, and ranks see Table 4.

As depicted in Figure 21, unlike Wolter and Timlin (2011), the frequency of ENSO events monotonically decreases as a function of intensity, with Weak, Moderate, Strong, and Super ENSO constituting 13%, 10%, 7%, & 3% of the ranks respectively as opposed to occupying an equal fraction of the total ranks. Therefore, this distribution implies that stronger ENSO events occur with relatively less frequency than the weaker and moderate counterparts, which is likely a more reasonable assumption given that such intense events require more favorable intersection of conditions to develop, and this rank

distribution is also more in line with the frequencies of weak, moderate, and strong ENSO derived from CPC's ONI and ENS ONI indices.

CHAPTER 3: RESULTS AND DISCUSSION

Overall, as shown in Figure 23 and Table 6, the MEI.extv2 median ensemble value is similar to MEI.ext (Wolter and Timlin, 2011), with a correlation >0.95, and a mean squared difference in the index of 0.10 $\boldsymbol{\sigma}$. This suggests that analyzing holistic ENSO behavior over decades or more leads to the same general results regardless of the choice of dataset, central tendency, or climatological base period, and that the MEI.extv2 captures many of the same features as MEI.ext. However, for individual ENSO events, these values may differ substantially and these choices certainly become increasingly important. In fact, the MEI.ext is outside the MEI.extv2's 90% confidence interval (90% CI) in ~15% of all bi-monthly periods, with approximately 2/3rds of these bi-monthlies that are outside the 90% CI exceeding the upper 90% confidence bound. This is likely due to the MEI.ext's utilization of singular 1871-2005 base period in its analysis, as evidenced by the fact that 80% of the months that reported bi-monthly MEI.ext values above the 90% CI and a majority of all months that were outside the 90% CI (above or below) occurred after 1970. It is very likely that the utilization of a singular long-term base period in the MEI.ext is contributing to a significant positive bias in the index during the modern era due to long-term warming of the SST component of the index.

In order to remove any potential long-term biases in the MEI.ext and make it more comparable to the MEI.extv2, a linearly detrended version of MEI.ext was also created to provide a rough sense of what the MEI.ext would look like if there was some consideration for significant basic state climate change that occurs over the course of the instrumental record. The detrended MEI.ext was closer to the MEI.extv2 presented here, with a correlation coefficient of 0.96 and mean squared difference of 0.07$\boldsymbol{\sigma}$ in the 1876-

2005 period. Furthermore, the new detrended MEI.ext was inside the MEI.extv2's 90% CI bounds much more frequently with only 8% of bi-monthlies being outside the 90% CI and ever-so-slightly more bi-monthlies exceeding the lower than the upper 90% CI bound. The number of bi-monthlies after 1970 that were above the upper bound of the 90% CI decreased by over 80% relative to the unadjusted MEI.ext, highlighting the significance that proper base period adjustments has on the MEI.ext.

It is also worth mentioning that the weighted MEI.extv2 is on average about ~0.25$\boldsymbol{\sigma}$ different from the unweighted MEI.extv2, with a correlation of ~0.989. In the context of our uncertainty analysis, only ~2% of the weighted MEI.ext values were significantly different from the unweighted MEI, and most of the weighted MEI.ext values were within the IQR range of the unweighted MEI, suggesting that the inclusion of the weighting function has limited impact on the overall results of the MEI.extv2. However, on a case-by-case basis, these discrepancies may certainly be detectable and measurable, and while they are not significant in this analysis, these alterations arguably move the MEI.extv2 index general direction that is more consistent and backed by observations and the uncertainties associated with them.

The MEI.extv2 also compares favorably with the MEI.v1 (Wolter and Timlin, 1993) and MEI.v2 (Zhang et al, 2019), exhibiting correlations of 0.96 and 0.93 respectively (as shown in Table 9 and Figures 23-26). The weaker correlation associated with the MEI.v2 since 1979 may be due to the exclusion of surface air temperature in its analysis, which is kept in-tact in MEI.v1, and comprises ~2/3rds of the MEI.extv2 index since 1865, and over 80% of the total MEI.extv2 since 1979. In addition, MEI.v2 uses JRA-55 in its analysis, among the first reanalysis models to use 4D-Var (Kobayashi et al,

2015), while MEI.extv2 is limited to using many older reanalyses and reconstructions in its analysis, and the very short period of record may also allow for MEI.extv2 and MEI.v2 to exhibit increased dispersion in their handling of individual events and in particular, may make it somewhat difficult for MEI.v2 to constrain the intensity of events given their small sample size and large spread in event-to-event amplitude since the beginning of the satellite record.

In the context of the uncertainty analysis described in Section 2.3, the MEI.extv2 also compares favorably to all other versions of the MEI during the overlapping 1979-2005, with the overwhelming majority of bi-monthly periods for all MEI falling within the uncertainty bounds defined for MEI.extv2. The MEI.ext and MEI.v1, as expected, generally tend to fall towards the upper end of the MEI.extv2's uncertainty distribution for most of this part of the record as neither version of the MEI includes an adjustment to account for observational and climatic basic state changes that significantly influence MEI values, as depicted in figure 28 for MEI.ext. Also worth pointing out that the largest deviation any version of the MEI exhibits from MEI.extv2 and the uncertainty bounds is MEI.v2 during the decay phase of the 1997-98 "Super" El Nino. The MEI.v2 in late 1998 is greater than 1σ below the lowermost bound of MEI.extv2's uncertainty and the closest neighboring MEI index during this time, potentially signaling a potential issue in the JRA-55 reanalysis that MEI.v2 is based upon.

To define ENSO "years" we use the median ensemble analysis, and focus on the portion of the calendar year where ENSO is typically the most prominent (from the fall to spring equinox, or in bi-monthly form (September-October to February-March). Time periods when at least 4 of the 6 bi-monthly periods fall within one phase of ENSO are

labeled as El Nino or La Nina. Using this definition, the MEI.extv2 identifies 34 El Nino events and 31 La Ninas events as well as 52 El Nino winters and 53 La Nina winters since 1865 (see Table 7), with both exhibiting an average return period of about 4.5 years, and 90% confidence intervals of 4.1-5.6 and 4.2-7.3 years respectively. Roughly 95% of ENSO events since the mid-late 19th century exhibit an expected return period of 2-7 years (Figure 29), with all events returning within 12 years. The return period of La Ninas does not exhibit any notable trends over the record (not shown), but during the mid-20th century the overall dearth of El Ninos in the 1930s and 1940s is particularly evident, with the largest spacing between successive El Nino events lasting up to 12 years (1939-1951) and it was immediately preceded by another anomalously large period of 9 years from 1930-1939, although an very short-lived El Nino may have occurred in early-mid 1932 (see Table 10), not unlike other events in 1891 and 1993 which, like 1932, developed early in the year only to terminate before the following winter (Tables 11-12).

Based on the lower and upper bound of our 90% confidence interval, the number of boreal winters with an El Nino or La Nina may actually reasonably vary anywhere between 30 and 70 winters for either phase of ENSO, underlining the uncertainties associated with the data, especially given that the frequency of both El Ninos and La Ninas could legitimately differ by a factor of two.

The top five strongest El Ninos in our analysis (and corresponding peak ensemble MEI.extv2 value) as shown in Table 5 are 1997-98 (+2.94$\boldsymbol{\sigma}$), 1876-78 (+2.85$\boldsymbol{\sigma}$), 1982-83 (+2.72$\boldsymbol{\sigma}$), 2015-16 (+2.50$\boldsymbol{\sigma}$), and 1888-89 (+2.09$\boldsymbol{\sigma}$), while the strongest five La Ninas (as shown in Table 8) are 1975-76 (-2.07$\boldsymbol{\sigma}$), 1916-17 (-2.03$\boldsymbol{\sigma}$), 1973-74 (-1.96$\boldsymbol{\sigma}$), 1909-10 (-1.95$\boldsymbol{\sigma}$), and 2010-11 (-1.93$\boldsymbol{\sigma}$), with corresponding time series for both groups of ENSO

events depicted in Figures 30-31. Even from this analysis of the top five most intense events, it is apparent that the strongest El Ninos tend to be stronger than the deepest La Ninas and exhibit a more tightly clustered, uniform evolution. This result is somewhat expected since there are non-linear feedbacks related to locally forced moist convection and concomitant lower tropospheric wind anomalies that are often directly or very closely linked to positive near-equatorial SST anomalies (Geng et al, 2019; Xie et al, 2019; Takahashi et al 2015). It is also clear from our uncertainty and ensemble median analysis that the 1997-98, 1876-78, 1982-83, and 2015-16 El Ninos are not only likely the four strongest El Ninos since the mid 19th century, but the strongest El Nino or La Nina events in this time (Huang et al, 2020), with all of these El Ninos exhibiting a peak MEI.extv2 member El Nino and strong-Super El Nino probability of 100%, aside from 1877-78, whose Strong-Super El Nino probability was 91% in Jan-Feb 1878 at its ensemble median peak (Table 5; Figures 32-41).

Like Wolter and Timlin (2011), we find that the median length of La Ninas (16 bi-monthlies) is longer than that of El Ninos (13 bi-monthlies), although this difference is not significant at the 90% level. However, the upper end of the 90% interval for La Ninas is considerably larger than El Ninos, and the top 9 La Ninas were all pegged to be "Super" or "Strong" events, perhaps suggesting that with a longer and more reliable record, a more clear relationship would between ENSO phase and event length would emerge as is discussed in (Dienezio and Deser, 2014). Longer-lived La Ninas would be expected given that during multi-year La Ninas, weaker subsurface winds for a similar changes in SST anomalies, dampens and slows the recharge of the thermocline, ultimately limiting the ability of subsurface anomalies to influence ocean temperatures in

the mixed layer (DiNezio and Deser, 2014). Moreover, subsurface cold anomalies from off the equator often get entrained into the equatorial Pacific, interrupting the ENSO's recharge phase following an El Nino (Hu et al, 2014; Deepak et al, 2019) and disturbing the natural succession of ENSO (Kessler 2002), allowing La Ninas to persist longer. Multi-year La Ninas have also been found to be more likely when they were immediately preceded by an intense El Nino (Wu et al, 2019). Our results agree with these mechanisms. It is also possible that remote forcing of West Pacific trade wind variability from the Indian Ocean may play a role in shaping the behavior of multi-year La Ninas (Ohba and Ueda, 2007; Okumura and Deser, 2010; Dong and McPhaden, 2018). Furthermore, climate models often struggle in forecasting multi-year La Nina events (Hu et al, 2014; Barnston et al, 2010), revealing a potential weakness in our understanding of multi-year La Nina behavior and theories such as the recharge/discharge oscillator (Battisti and Hurst, 1988; Suarez and Schopf, 1988; Jin et al, 1997; Wang, 2001; Hu et al, 2014), although some successful model simulations have been conducted that accurately predict multi-year La Ninas (Dinezio et al, 2017).

We find that approximately half of El Ninos and 40% of La Nina events last more than one consecutive boreal winter, with a 90% confidence interval of 10-60% and 40-60% respectively. The confidence interval for multi-year El Nino proportion over the instrumental record is therefore considerably larger than for multi-year La Ninas. This is likely attributable to the fact that multi-year El Ninos more frequently contain at least one (or more) borderline, weak El Ninos relative to La Ninas, which may possess multiple strong events in very rapid succession (e.g. 1973-74 and 1975-76). Moreover, unlike La Ninas, multi-year El Ninos are thought to be more closely linked to timing of their onset

in the calendar year as well as their "flavor" (i.e. Central or East-Pacific based) (Wu et al, 2019). Studies such as Wu et al (2019) posit that El Ninos that onset later in the calendar year (late northern summer or fall vs spring) and events that are biased towards the central Pacific (i.e. modoki El Ninos; Ashok et al, 2007) are more likely to persist into the following year because the upwelling Rossby Waves that reflect on the western boundary region and become upwelling Kelvin Waves are delayed late enough in the calendar year such that the east-central Pacific cold tongue and Bjerknes feedbacks become re-established and dampen the impact of the upwelling Kelvin Wave. Also, El Ninos being biased towards the central Pacific make the western Pacific less susceptible to enhanced trade winds due to Indian Ocean warming during El Nino (Kug and Kang, 2006; Ohba and Ueda, 2007; Wu et al, 2019) and central Pacific El Ninos tend to be weaker on average than their traditional counterparts, effectively weakening the subsequent upwelling Kelvin Wave that attempts to weaken the El Nino.

The amplitude of these weak El Ninos relative to "Neutral" ENSO, as we defined previously in this paper, are not large enough to remain El Ninos within the bounds of uncertainty we have defined. The multi-year La Nina proportion and confidence interval found in our analysis is consistent with modeling studies that find in the Community Climate System Model 4.0 (CCSM4), and Community Earth System Model 1.0 (CESM1) respectively, that anywhere between 10% and 70% (Dinezio and Deser, 2014), and ~50% (Wu et al, 2019) of La Nina events are multi-year events.

Regarding ENSO amplitude as a function of length, both El Nino and La Nina events exhibit moderate-strong positive linear correlations between event length and intensity, with El Ninos and La Ninas exhibiting a correlation of 0.62 and 0.81

respectively. These values suggest that longer lived ENSO events are also more likely to be more intense, and this relationship is stronger for La Nina events. This relationship was not initially anticipated given the strong negative feedbacks that terminate El Nino (Guan et al, 2019; Enfield, 1989), however it clearly shows that larger El Ninos take more time to build-up than weaker events, and that this is generally more important in determining the duration of El Nino than the negative feedbacks that lead to their demise. In addition, the weaker linear relationship for El Ninos suggests that the relationship is, if anything, potentially more nonlinear, which once again, underscores the larger nonlinearities in the physical processes that drive El Ninos.

Akin to the holistic comparison between MEI.extv2 and MEI.ext, the choice of using EOF-based vs box-averaged does not have a substantial impact on the MEI.extv2 value over long periods of time, but the same can not be said on an individual case-by-case basis. The box-averaged regions were found to correlate very strongly at >0.96 with a mean squared difference of less than 0.15 $\boldsymbol{\sigma}$ with the PC1 EOF-based time series across datasets. One major distinction between the box-averaged and PC1 time series, especially for SST, was that the box-averaged series tends to lag PC1 by a few bi-monthlies near the peak and decay phase of a major El Nino event. This is likely indicative of how the SST and SAT anomalies in the east-central equatorial Pacific take time to completely deteriorate, with the latter having a well established lag with ENSO intensity (Trenberth et al, 2002) while the rest of the tropical Pacific is already beginning to adjust to the forthcoming ENSO basic state change (often a La Nina). Somewhat consistent with this result, when comparing the PC1 and box-averaged time series, the spread between the two is apparently slighter larger during both intense El Ninos and La Ninas. This

behavior may also be explained by the fact that more infrequent and intense ENSO events are less constrained by observations with fewer events with which to compare, and while we did not find that spread was intensity-dependent (not shown), it is legitimately possible with a longer time series, with more datasets and higher quality data to constrain it, that larger uncertainties would confidently be associated with stronger ENSO. Regardless, it certainly highlights the necessity to cross-validate different methods and datasets, especially if it is true that uncertainty is correlated with intensity, as ENSO typically garners more attention and widespread appeal when it is very strong.

When dissecting the individual SST and SLP ensemble medians, with the median time series for the EOFs shown in Figure 42, an emergent finding are the lead-lag relationships amongst these variables at specific points in the record, especially as it pertains to subseasonal variability. The cross-correlation analysis (Figure 43) reveals that they are slightly better correlated when SLP leads SST by about one bi-monthly period or so. We also encounter a few periods where the SLP ensemble median significantly leads changes in the SST component that eventually lead to the onset of an El Nino event. Our index identifies several possible periods prior to 1950 where the SLP component of the MEI was significantly greater (at the 90% level) than SST preceding the onset of El Nino. In particular we find that Sep-Oct 1876, Jul-Aug thru Aug-Sep 1887, Dec-Jan thru Jan-Feb 1884, Feb-Mar 1891, May-Jun and Oct-Nov 1913, Jun-Jul thru Jul-Aug 1923, May-Jun thru Jun-Jul 1925, as well as Nov-Dec 1929 and Feb-Mar 1930. Our index also identifies Mar-Apr 1997 as a period where the SLP component preceded significant changes in SST, with the spring of 1997 being associated with an especially intense MJO event (Zhang et al, 2001; McPhaden, 1999; Tang and Yu, 2008), thus lending credence to

its capability to potentially detect major sources of intense, and "reddened" atmospheric subseasonal variability that often precedes El Nino events.

Of the time periods and their associated subsequent El Ninos identified above for lead-lag analysis, the Jul-Aug thru Aug-Sep 1887 period is the most intriguing and notable. Firstly, as discussed in Chapter 2 and shown in Figure 13, the mid-late 1880s represents a local maximum in sea surface observational density, with the summer of 1887 being located near the tail end of this local max, wherein the greatest coverage of sea surface observations were seen here prior to the 1920s. Also, the difference between the SLP and SST ensemble medians is significant even at the 98% level. The SST component of the MEI.extv2 trailed the SLP component by ~2-3 months in mid-late 1887 and into early 1888, becoming positive in Oct-Nov 1887, while the SLP index was already positive in Jul-Aug 1887 (Figure 44). This lag is generally consistent with the period of the downwelling phase of the equatorial oceanic Kelvin Wave. While the MJO in its traditional form (as a Real-time Multivariate MJO or RMM index) only explains ~25% of the total subseasonal (20-90 day) variance in zonal winds and OLR (Wheeler and Hendon, 2004), it is possible that our MEI.extv2 index is actually picking up on an ancient MJO event (or series of MJOs) that preceded the onset of the very intense and prolonged "Super" El Nino in 1888-89 and perhaps other El Ninos prior to 1950, suggesting that many of the same physical processes that have been observed to trigger El Ninos in the modern, satellite-era also were also similarly operating in a basic state climate that was less influenced by anthropogenic climate change.

We find that ENSO amplitude was higher near the turn of the 20th and 21st centuries than during the mid-20th century. Based on our ensemble median analysis, 25-

year averaged El Nino amplitude was ~50% higher near the turn of the 20th and 21st centuries than during the mid-20th century. El Nino amplitude was utilized here in favor of analyzing both El Ninos and La Ninas as this has been the preferred way of measuring multidecadal-centennial scale ENSO amplitude in studies such as Quinn (1992) and Garcia-Herrera et al (2008). To determine El Nino amplitude, all bi-monthly periods with negative data were set equal to zero, with the rest of the positive values remaining unchanged, then a 25-year moving average filter was applied, and the resulting time series was fitted with a high order polynomial (Figure 45).

Interestingly, Garcia-Herrera et al (2008) found using a chronology of ENSO events based on documented sources from northern Peru that ENSO amplitude since the 1500s has tended to peak near the turn of the centuries and these active eras were flanked by relatively more quiescent periods during the middle of the centuries. While their work is not in complete agreement with those of previous studies (Quinn, 1992; Ortileb, 2000), extension of their chronology into the present-day using the MEI.extv2 suggests that there may be indeed a very low frequency, centennial scale oscillation that is forced by unknown or yet to be fully resolved slowly-varying, internal dynamics intrinsic to ENSO and/or harmonical "external" forcing. In fact, it is reasonably probable that the sum of the observed changes in ENSO frequency and intensity over the course of the instrumental record are a rectification of internal variability linked to centennial-scale changes in the the zonal surface pressure and sea surface temperature gradient across the equatorial Pacific and the variations in the strength and breadth of the west Pacific warm pool.

As discussed by Karnauskas et al (2012), this centennial-scale variability, which is also hinted at in ENSO chronologies from written records (Garcia-Herrera et al, 2008), may be a manifestation of oceanic heat content discharge (build-up) during periods of heightened (weaker) ENSO activity, wherein La Ninas (El Ninos) are not (are) capable of completely recharging all the heat that is released during (often preceding) (following) El Nino (La Nina) events. Thus, the impact of anthropogenic climate change on ENSO, which is most prominent in the last few hundred years and directly coincides with the instrumental record, may not be detectable against centennial-scale, internal variability and it is rather uncertain and yet to be seen whether or not this component of low frequency tropical variability will dampen or be enhanced by man-made climate change.

Very tentatively extrapolating the waveform of this apparent centennial-scale cycle derived from our data based on instrumental records forward in time suggests that ENSO activity may once again weaken in the mid 21st century relative to the late 20th and early 21st centuries as it did in the mid 20th century. If such behavior is in fact realized over the coming few decades, it would certainly lend considerably more confidence to the idea that there is a centennial-scale cycle in ENSO amplitude, as portions of at least three cycles of this oscillation would be captured by the instrumental record.

Whatever the case may be, it is an exceptionally interesting observation nonetheless that may not be fully explainable by random, stochastic behavior alone, and such an observation would not be possible without attempting to extend ENSO indices beyond the confines of the most reliable portion of the instrumental record in the mid-late 20th century.

CHAPTER 4: CONCLUSIONS AND FUTURE WORK

The MEI.extv2 is a significant upgrade to the original MEI.ext (Wolter and Timlin, 2011) and quantifies ENSO behavior since the middle of the 19th century with estimates of parametric and structural uncertainties as well as indirect measures of observational uncertainty. By utilizing multiple variables and multiple methods, a large array of reanalysis datasets and SST and SLP reconstructions (Tables 1-2), a very large suite of statistical realizations, and accounting for differences in observational input, EOF vs box-averaged output, and inter-dataset spread between the two variables (SST and SLP) that comprise the MEI.extv2, the bi-monthly resolution MEI.extv2 for 1865 to present is a major contribution to the community as a whole. In our methods, we also develop the first community estimate of the bi-monthly confidence interval in our ENSO index. Finally, unlike MEI.v1 and MEI.ext, MEI.extv2 is available in near real-time.

The MEI.extv2 over multi-decadal to centennial temporal scales agrees well with the original detrended Extended MEI (MEI.extv1), and is also comparable to the more limited time series from the original MEI (1950-2019) and MEI.v2 (1980-present) in the satellite era. Although the MEI.extv2 is in many ways different from other version of the MEI and other ENSO indices, the MEI.extv2 also correlates fairly strongly to other, non-MEI measures of ENSO, and thus is indeed measuring the same phenomena. Similar to Wolter and Timlin (2011), the MEI.extv2 shows that ENSO was more active at the turn of the 20th and 21st centuries than during the middle of the 20th century (Figure 45), and that recent ENSO behavior is not in any way unusual in the context of the centennial scale observational record. Furthermore, corroborating the MEI.extv2 with ENSO chronologies that extend back multiple centuries (Garcia-Herrera et al, 2008) very

tentatively suggests that ENSO activity could begin to wane as we approach the mid 21st century as it did in the mid-20th century, if the pattern holds.

Unlike Wolter and Timlin (2011), with the MEI.extv2, we do not find statistically significant relationships between ENSO phase and duration over the instrumental record, although these may certainly exist with a longer period of record that is better constrained by more higher quality observations and improved reanalyses (Wu et al, 2019). The frequency of El Nino and La Nina events in the instrumental record are also variable by a factor of two according to our uncertainty analyses, although we do find that most (~95%) of ENSO events exhibit a return period of 2-7 years (Figure 29), with the exceptions to these potentially occurring during the mid-20th century when ENSO was less active. We also take note that while the ensemble median analysis does not explicitly show any El Ninos in the observed record lasting longer than three successive bi-monthly winters, our uncertainty analysis indicates that even in the modern era, with a multitude of datasets analyzing SST and SLP which are also constrained by frequent observations, including in-situ buoy data, it is legitimately possible that a 5-year long El Nino was present from 1990-95 as also suggested by Trenberth and Hoar (1996) and Wolter and Timlin (2011). Indeed, even our median analysis indicates that ENSO during this general timeframe was characterized by at least 3 separate El Nino events (1991-92, 1993, and 1994-95), with the intervening periods marked by “warm neutral” conditions, whose uncertainty is not small enough to legitimately preclude the possibility that these periods were not also in weak El Nino territory. Regardless, such very long-lived El Ninos are legitimately possible and have been hinted at in proxy reconstructions, chronologies, and written records (Grove, 1998; Grove, 2007; Gergis and Fowler, 2009).

While the possibility that anthropogenic climate change influencing the phase, intensity, and ENSO asymmetry certainly exists to some extent (Gergis and Fowler, 2006; Trenberth and Hoar, 1997) given the rather large uncertainties associated with observations and reanalyses that rely on them, the small sample size of well observed, significant ENSO events, wherein internal variability may be larger than any actual signal derived from them without a record of several dozen (or more) ENSO events of specific phases and intensities (Garfinkel et al, 2019), and the possibility that a recent uptick in ENSO activity in late 20th and early 21st centuries could be significantly influenced by natural, centennial-scale variability in the tropical Pacific (Karnauskas et al, 2012), no detectable influence from climate change on ENSO was confidently found in the MEI.extv2.

In our ensemble median and uncertainty analyses, we find some evidence of potential rectification and projection of subseasonal variability even prior to 1950. Namely, the possible footprints of "ancient" MJO events in the growth stage of El Ninos (Figure 44), as we have observed during other extraordinary El Ninos in the satellite era (Kessler and Kleeman, 2000; Bergman et al, 2001; Hendon et al, 2007; Chen et al, 2016b), was also hinted at in our SLP data from mid-late 1887, preceding the 1888-89 "Super" El Nino.

Even with the improvements made in the MEI.extv2 over MEI.ext, there are still a host of potential upgrades worth exploring in future versions of the MEI.extv2. For instance, addition of EOF2 data similar to Wheeler and Hendon (2004) RMM MJO diagram would provide a more complete picture of ENSO allow for easier diagnosis of how not only the amplitude and phase, but the character of ENSO has changed over the

course of the observational record, which may be critical in understanding ENSO duration (Wu et al, 2019) and eradicating the spring predictability barrier.

On the other hand, introduction of EOF2 in SLP and SST may also warrant further, more complex uncertainty considerations as EOF-1 and EOF-2 may be non-linearly dependent on one another (Monahan et al, 2009) and it is possible that there are larger discrepancies in EOF-2 amongst most reanalysis datasets, which would require an additional examination of how EOF2 may affect the MEI.extv2's output, which we found to be of negligible influence here using EOF-1.

Re-introducing bi-monthly sliding EOFs for both SST and SLP as well as an additional stream of data, with a more moderate-sized box (or boxes) to further refine the effect of regional averaging on the MEI.ext, plus the uncertainty that may arise from using a singular EOF for all bi-monthlies as opposed to 12 bi-monthly EOFs may be worth additional inspection. The lack of bi-monthly sliding EOFs in MEI.extv2 may also mean that the MEI.extv2 is an inferior measure of ENSO at specific times of the calendar (especially the boreal summer), although this also happens to be when ENSO is the weakest and our inter-comparison with MEI.ext, MEI.v1, and MEI.v2 suggest that any changes to the would be minimal at best and potentially not measurable outside our uncertainty analysis. An additional change that may further buttress a future MEI.extv2 product would be to allow the EOF regions to change with each bi-monthly period, allowing them to effectively track the highest loading areas of SST and SLP, as this could result in the index capturing ENSO-related variability slightly better.

While MEI.extv2's weighting equation does not lead to significantly different values overall in the weighted vs unweighted MEI, introduction of additional pieces of

information, such as accounting for differences in power spectra between SST and SLP, wherein a larger fraction of variance at higher (lower) frequencies for SLP (SST) due to inclusion (exclusion) of atmospheric "white noise" and inherent differences in the thermal inertia and phase speeds of waves that propagate through the various mediums. However, it may be difficult to validate the power spectra prior to 1950, as the limited amount of data and assumption that pre and post 1950 ENSO behavior are exactly alike are significant points of contention. Additionally, exploration of sampling uncertainties and biases in the fraction of day vs night observations as a function of time in the observed record may be critical for understanding long-term ENSO behavior, particularly for SLP whose diurnal cycle is on the order of ~ 2-3mb in the tropics (Le Blancq, 2011), as few datasets aside from Hadley Nighttime Marine Air Temperature version 2 (HADNMAT2) (Kent et al, 2013), have examined this relationship, and none to our current knowledge have done so without complete removal of night or day observations from their analysis, which could be particularly problematic in parts of the record where few observations already exist and the vast majority of available data that would be removed actually comes during the time of the day that isn't being considered.

We also anticipate that subsequent versions of the MEI.extv2 should be capable of beginning to explicitly address observational uncertainty in the data underpinning most of our datasets from the release of observational platform data in later releases of ICOADS. Knowledge of observational platform types, their relative coverage in a particular part of the domain, the types of instruments they typically carried at specific time in the record, understanding of uncertainties associated w/ the instruments themselves, and some consideration of uncertainty in the observer recording the data will

provide a deeper, more complete understanding of uncertainty in the instrumental record to corroborate structural uncertainties between datasets and parametric uncertainties associated with processing of the output from these datasets that have been discussed here. Also, future versions of MEI.extv2 should further explore some of these parametric uncertainties, particularly relating to ENSO definitions, such that an ensemble of definitions from a wide array of literature is also produced and inter-compared, ultimately decreasing the sensitivity of the MEI.extv2 to subjective parameter spaces, and increasing the robustness of and confidence in our results.

As the number of archived observations and our breath of knowledge of their concomitant uncertainty increases, reanalysis products grow more numerous, sophisticated, and reliable, it may be feasible to introduce additional variables (such as low-level zonal winds) in a future version of the extended MEI apart from SST and SLP, even though discontinuities and secular trends are more likely given the relative lack of reanalysis datasets with which to examine this variable (Wolter and Timlin, 2011), and non-physical trends surface wind data due to changes in observational platforms such as a paradigm shift from sail to motorized ships in the late 19th century accompanied by more frequent anemometer measurements (Ramage, 1987). Inclusion of such data however would probably result in even larger ENSO asymmetry as measured by a future MEI.extv2, as the moist convection and surface wind variability coinciding with the convection are the primary catalysts for the asymmetries that permeate into SLP and especially SST anomalies.

Similar analyses as we have done with the MEI.extv2 could be applied to climate and general circulation models (Wolter, Personal Communication), although the new, 6th

generation of CMIP models (CMIP6) exhibits significant improvement in its depiction of tropical phenomena like the MJO and ENSO, limited progress has been made in simulating tropical precipitation, as CMIP6's precipitation errors in the tropics are beyond the uncertainty range of available satellite products and still exhibit a stout double ITCZ over the tropical Pacific (Fiedler et al, 2020). Moreover, statistical ENSO models still perform comparably to or often better than dynamical models for ENSO forecasting (Ham et al, 2019; Zhang et al, 2019).

Unlike MEI.extv1, the MEI.extv2 is intended to be used for near real-time monitoring of ENSO and may thus be a viable alternative to the MEI.v2 as a potential apples-apples comparison of ENSO events over very long periods of time. Users of the MEI.extv2 should expect some further improvements to the MEI.extv2 to continue for the foreseeable future with data expected to become publicly available relatively soon.

REFERENCES

Alexander, M. A., et al. (2002). "The Atmospheric Bridge: The Influence of ENSO Teleconnections on Air–Sea Interaction over the Global Oceans." Journal of Climate 15(16): 2205-2231.

Allan, R. J., et al. (1991). "A Further Extension of the Tahiti-Darwin SOI, Early ENSO Events and Darwin Pressure." Journal of Climate 4(7): 743-749.

Allan, R. and T. Ansell (2006). "A New Globally Complete Monthly Historical Gridded Mean Sea Level Pressure Dataset (HadSLP2): 1850–2004." Journal of Climate 19(22): 5816-5842.

An, S.-I. and F.-F. Jin (2004). "Nonlinearity and Asymmetry of ENSO." Journal of Climate 17(12): 2399-2412.

Ångström, A. (1935). "Teleconnections of Climatic Changes in Present Time." Geografiska Annaler 17: 242-258.

Ashok, K., et al. (2007). "El Niño Modoki and its possible teleconnection." Journal of Geophysical Research: Oceans 112(C11).

Barnett, T., et al. (1988). "On the prediction of the El Niño of 1986-1987." Science 241(4862): 192-196.

Barnston, A. G., et al. (1997). "Documentation of a highly ENSO-related sst region in the equatorial pacific: Research note." Atmosphere-Ocean 35(3): 367-383.

Barnston, A. G., et al. (2010). "Verification of the First 11 Years of IRI's Seasonal Climate Forecasts." Journal of Applied Meteorology and Climatology 49(3): 493-520.

Barnston, A. G. (2016). "Evolution of ENSO Prediction over the Past 40 Years." Climate Prediction S&T Digest: 94.

Battisti, D. S. and A. C. Hirst (1988). "Interannual Variability in a Tropical Atmosphere–Ocean Model: Influence of the Basic State, Ocean Geometry and Nonlinearity." Journal of the Atmospheric Sciences 46(12): 1687-1712.

Benthuysen, J., et al. (2014). "Spatial patterns of warming off Western Australia during the 2011 Ningaloo Niño: quantifying impacts of remote and local forcing." Continental Shelf Research 91: 232-246.

Bergman, J. W., et al. (2001). "Intraseasonal air–sea interactions at the onset of El Niño." Journal of Climate 14(8): 1702-1719.

Bevan, A. (2013). Statistical data analysis for the physical sciences, Cambridge University Press.

Bing, Z. and S. Xie (2017). "The 2015/16 “Super” El Niño Event and Its Climatic Impact." Chinese Journal of Urban and Environmental Studies 05(03): 1750017.

BJERKNES, J. (1969). "ATMOSPHERIC TELECONNECTIONS FROM THE EQUATORIAL PACIFIC." Monthly Weather Review 97(3): 163-172.

Blunden, J. and D. S. Arndt (2019). "State of the Climate in 2018." Bulletin of the American Meteorological Society 100(9): Si-S306.

Broad, K. (2002). "Stanley A. Changnon (ed.), El Niño 1997–98: The Climate Event of the Century." Climatic Change 53(4): 523-527.

Brönnimann, S., et al. (2004). "Extreme climate of the global troposphere and stratosphere in 1940–42 related to El Niño." Nature 431(7011): 971-974.

Calafat, F. M., et al. (2014). "On the ability of global sea level reconstructions to determine trends and variability." Journal of Geophysical Research: Oceans 119(3): 1572-1592.

Cane, M. A., et al. (1986). "Experimental forecasts of El Niño." Nature 321(6073): 827-832.

Carella, G., et al. (2018). "Estimating sea surface temperature measurement methods using characteristic differences in the diurnal cycle." Geophysical Research Letters 45(1): 363-371.

Carrillo, C. (1892). "Hidrografía oceánica." Bol. Soc. Geogr. Lima 1: 72-111.

Chang, P., et al. (2007). "Pacific meridional mode and El Niño—Southern Oscillation." Geophysical Research Letters 34(16).

Chen, L., et al. (2016)a. "Distinctive precursory air–sea signals between regular and super El Niños." Advances in Atmospheric Sciences 33(8): 996-1004.

Chen, S., et al. (2016)b. "Genesis of westerly wind bursts over the equatorial western Pacific during the onset of the strong 2015–2016 El Niño." Atmospheric Science Letters 17(7): 384-391.

Chiang, J. C. H. and D. J. Vimont (2004). "Analogous Pacific and Atlantic Meridional Modes of Tropical Atmosphere–Ocean Variability." Journal of Climate 17(21): 4143-4158.

Cheng, L., et al. (2019). 2018 continues record global ocean warming, Springer.

Cheng, L., et al. (2020). Record-setting ocean warmth continued in 2019, Springer.

Claar DC, Szostek L, McDevitt-Irwin JM, Schanze JJ, Baum JK (2018) Global patterns and impacts of El Niño events on coral reefs: A meta-analysis. PLoS ONE 13(2): e0190957. https://doi.org/10.1371/journal.pone.0190957

Climate Prediction Center. (2005). El Nino Regions.

Compo, G. P., et al. (2011). "The Twentieth Century Reanalysis Project." Quarterly Journal of the Royal Meteorological Society 137(654): 1-28.

Dai, A. and T. Wigley (2000). "Global patterns of ENSO-induced precipitation." Geophysical Research Letters 27(9): 1283-1286.

Davis, M. (2002). Late Victorian holocausts: El Niño famines and the making of the third world, Verso Books.

Deepak, S. N., et al. (2019). "Impact of multiyear La Niña events on the South and East Asian summer monsoon rainfall in observations and CMIP5 models." Climate Dynamics 52(11): 6989-7011.

Deser, C. and J. M. Wallace (1990). "Large-Scale Atmospheric Circulation Features of Warm and Cold Episodes in the Tropical Pacific." Journal of Climate 3(11): 1254-1281.

DiNezio, P. N. and C. Deser (2014). "Nonlinear Controls on the Persistence of La Niña*." Journal of Climate 27(19): 7335-7355.

DiNezio, P. N., et al. (2017). "A 2 Year Forecast for a 60–80% Chance of La Niña in 2017–2018." Geophysical Research Letters 44(22): 11,624-611,635.

Dong, L. and M. J. McPhaden (2018). "Unusually warm Indian Ocean sea surface temperatures help to arrest development of El Niño in 2014." Scientific Reports 8(1): 1-10.

Enfield, D. B. (1989). "El Niño, past and present." Reviews of Geophysics 27(1): 159-187.

Fasullo, J., et al. (2018). "ENSO's changing influence on temperature, precipitation, and wildfire in a warming climate." Geophysical Research Letters 45(17): 9216-9225.

Fernández, N. C., et al. (2004). "Analysis of the ENSO Signal in Tropospheric and Stratospheric Temperatures Observed by MSU, 1979–2000." Journal of Climate 17(20): 3934-3946.

Fiedler, S., et al. (2020). "Simulated Tropical Precipitation Assessed across Three Major Phases of the Coupled Model Intercomparison Project (CMIP)." Monthly Weather Review 148(9): 3653-3680.

Fletcher, C. G. and P. J. Kushner (2011). "The Role of Linear Interference in the Annular Mode Response to Tropical SST Forcing." Journal of Climate 24(3): 778-794.

Folland, C. K. and D. E. Parker (1995). "Correction of instrumental biases in historical sea surface temperature data." Quarterly Journal of the Royal Meteorological Society 121(522): 319-367.

Fowler, A. M., et al. (2008). "ENSO history recorded in Agathis australis (kauri) tree rings. Part A: kauri's potential as an ENSO proxy." International Journal of Climatology 28(1): 1-20.

Freeman, E., et al. (2017). "ICOADS Release 3.0: a major update to the historical marine climate record." International Journal of Climatology 37(5): 2211-2232.

Garcia-Herrera, R., et al. (2008). "A Chronology of El Niño Events from Primary Documentary Sources in Northern Peru*." Journal of Climate 21(9): 1948-1962.

Garden, D. (2008). "El Niño, Irrigation Dams and Stopbanks: Examining the repercussions of the 1876-78 El Niño in Australia and New Zealand." History of Meteorology 4: 1.

Garfinkel, C. I., et al. (2019). "The salience of nonlinearities in the boreal winter response to ENSO: North Pacific and North America." Climate Dynamics 52(7): 4429-4446.

Gelaro, R., et al. (2017). "The Modern-Era Retrospective Analysis for Research and Applications, Version 2 (MERRA-2)." Journal of Climate 30(14): 5419-5454.

Gergis, J. L. and A. M. Fowler (2009). "A history of ENSO events since AD 1525: implications for future climate change." Climatic Change 92(3-4): 343-387.

Gill, A. E. (1980). "Some simple solutions for heat-induced tropical circulation." Quarterly Journal of the Royal Meteorological Society 106(449): 447-462.

GISTEMP Team, 2020: GISS Surface Temperature Analysis (GISTEMP), version 4. NASA Goddard Institute for Space Studies. Dataset accessed 20YY-MM-DD at https://data.giss.nasa.gov/gistemp/

Gray, W. M. (1984). "Atlantic Seasonal Hurricane Frequency. Part I: El Niño and 30 mb Quasi-Biennial Oscillation Influences." Monthly Weather Review 112(9): 1649-1668.

Grove, R. H. (1998). "Global impact of the 1789-93 El Niño." Nature 393(6683): 318-319.

Grove, R. H. (2007). "The Climatic and Economic Crisis of 1788–1795 and the Discovery of El Niño." SUSTAINABILITY OR COLLAPSE?: 151.

Grove, R. and G. Adamson (2018). El Niño in the Twentieth Century. El Niño in World History. London, Palgrave Macmillan UK: 181-197.

Guan, C., et al. (2019). "Quantifying the Role of Oceanic Feedbacks on ENSO Asymmetry." Geophysical Research Letters 46(4): 2140-2148.

Ham, Y.-G., et al. (2019). "Deep learning for multi-year ENSO forecasts." Nature 573(7775): 568-572.

Hameed, S. N., et al. (2018). "A model for super El Niños." Nature Communications 9(1): 2528.

Hamlington, B., et al. (2011). "Reconstructing sea level using cyclostationary empirical orthogonal functions." Journal of Geophysical Research: Oceans 116(C12).

Harada, Y., et al. (2016). "The JRA-55 Reanalysis: Representation of Atmospheric Circulation and Climate Variability." Journal of the Meteorological Society of Japan. Ser. II 94(3): 269-302.

Harrison, D. and G. A. Vecchi (1997). "Westerly wind events in the tropical Pacific, 1986–95." Journal of Climate 10(12): 3131-3156.

Harrison, M. and C. F. Meindl (2001). "A statistical relationship between El Nino-Southern Oscillation and Florida wildfire occurrence." Physical Geography 22(3): 187-203.

Harvey, R. R. and W. C. Patzert (1976). "Deep current measurements suggest long waves in the eastern equatorial Pacific." Science 193(4256): 883-885.

Hayashi, M. and F.-F. Jin (2017). "Subsurface Nonlinear Dynamical Heating and ENSO Asymmetry." Geophysical Research Letters 44(24): 12,427-412,435.

Hendon, H. H., et al. (1998). "Oceanic Kelvin Waves and the Madden–Julian Oscillation." Journal of the Atmospheric Sciences 55(1): 88-101.

Hendon, H. H., et al. (2007). "Seasonal Dependence of the MJO–ENSO Relationship." Journal of Climate 20(3): 531-543.

Hennermann, K. and Berrisford, P.: What are the changes from ERA-Interim to ERA5?, available at: https://confluence.ecmwf.int/pages/viewpage.action?pageId=74764925 (last access: 10 Jun 2019), 2018.

Hersbach, H. and Dee, D.: ERA5 reanalysis is in production, ECMWF Newsletter, Vol. 147, p. 7, available at: https://www.ecmwf.int/en/newsletter/147/news/era5-reanalysis-production (last access: 10 Jun 2019), 2016

Hersbach, H., et al. (2015). "ERA-20CM: a twentieth-century atmospheric model ensemble." Quarterly Journal of the Royal Meteorological Society 141(691): 2350-2375.

Hirahara, S., et al. (2014). "Centennial-Scale Sea Surface Temperature Analysis and Its Uncertainty." Journal of Climate 27(1): 57-75.

Hong, L.-C. (2016). Super El Niño, Springer.

Horel, J. D. and J. M. Wallace (1981). "Planetary-Scale Atmospheric Phenomena Associated with the Southern Oscillation." Monthly Weather Review 109(4): 813-829.

Hu, Z.-Z., et al. (2014). "Why were some La Niñas followed by another La Niña?" Climate Dynamics 42(3): 1029-1042.

Huang, B., et al. (2015). "Extended Reconstructed Sea Surface Temperature Version 4 (ERSST.v4). Part I: Upgrades and Intercomparisons." Journal of Climate 28(3): 911-930.

Huang, B., et al. (2016). "Further Exploring and Quantifying Uncertainties for Extended Reconstructed Sea Surface Temperature (ERSST) Version 4 (v4)." Journal of Climate 29(9): 3119-3142.

Huang, B., et al. (2016). "Ranking the strongest ENSO events while incorporating SST uncertainty." Geophysical Research Letters 43(17): 9165-9172.

Huang, B., et al. (2017). "Extended reconstructed sea surface temperature, version 5 (ERSSTv5): upgrades, validations, and intercomparisons." Journal of Climate 30(20): 8179-8205.

Huang, B., et al. (2020). "How Significant Was the 1877/78 El Niño?" Journal of Climate 33(11): 4853-4869.

Hurlburt, H. E., et al. (1976). "A Numerical Simulation of the Onset of El Niño." Journal of Physical Oceanography 6(5): 621-631.

Ishii, M., et al. (2005). "Objective analyses of sea-surface temperature and marine meteorological variables for the 20th century using ICOADS and the Kobe Collection." International Journal of Climatology 25(7): 865-879.

Japan Meteorological Agency, 2006: Characteristics of Global Sea Surface Temperature Analysis Data (COBE-SST) for Climate Use. Monthly Report on Climate System, Separated Volume, 12, 116pp.

Jeong, H.-I. and J.-B. Ahn (2017). "A new method to classify ENSO events into eastern and central Pacific types." International Journal of Climatology 37(4): 2193-2199.

Jiménez-Muñoz, J. C., et al. (2016). "Record-breaking warming and extreme drought in the Amazon rainforest during the course of El Niño 2015–2016." Scientific Reports 6: 33130.

Jin, F.-F. (1997). "An equatorial ocean recharge paradigm for ENSO. Part I: Conceptual model." Journal of the Atmospheric Sciences 54(7): 811-829.

Jones, G. S. and P. A. Stott (2011). "Sensitivity of the attribution of near surface temperature warming to the choice of observational dataset." Geophysical Research Letters 38(21).

Jong, B.-T., et al. (2020). "ENSO Teleconnections and Impacts on U.S. Summertime Temperature during a Multiyear La Niña Life Cycle." Journal of Climate 33(14): 6009-6024.

Julian, P. R. and R. M. Chervin (1978). "A Study of the Southern Oscillation and Walker Circulation Phenomenon." Monthly Weather Review 106(10): 1433-1451.

Kanamitsu, M., et al. (2002). "NCEP–DOE AMIP-II Reanalysis (R-2)." Bulletin of the American Meteorological Society 83(11): 1631-1644.

Kaplan, A., et al. (1998). "Analyses of global sea surface temperature 1856–1991." Journal of Geophysical Research: Oceans 103(C9): 18567-18589.

Karnauskas, K. B., et al. (2012). "A Pacific Centennial Oscillation Predicted by Coupled GCMs*." Journal of Climate 25(17): 5943-5961.

Kataoka, T., et al. (2014). "On the Ningaloo Niño/Niña." Climate Dynamics 43(5-6): 1463-1482.

Kawamura, A., et al. (1998). "Chaotic characteristics of the Southern Oscillation Index time series." Journal of Hydrology 204(1-4): 168-181.

Kennedy, J. J., et al. (2011). "Reassessing biases and other uncertainties in sea surface temperature observations measured in situ since 1850: 1. Measurement and sampling uncertainties." Journal of Geophysical Research: Atmospheres 116(D14).

Kennedy, J. J. (2014). "A review of uncertainty in in situ measurements and data sets of sea surface temperature." Reviews of Geophysics 52(1): 1-32.

Kennedy, J. J., et al. (2019). "An ensemble data set of sea-surface temperature change from 1850: the Met Office Hadley Centre HadSST.4.0.0.0 data set." Journal of Geophysical Research: Atmospheres 0(ja).

Kent, E. C., et al. (2013). "Global analysis of night marine air temperature and its uncertainty since 1880: The HadNMAT2 data set." Journal of Geophysical Research: Atmospheres 118(3): 1281-1298.

Kessler, W. S. and R. Kleeman (2000). "Rectification of the Madden–Julian oscillation into the ENSO cycle." Journal of Climate 13(20): 3560-3575.

Kessler, W. S. (2001). "EOF Representations of the Madden–Julian Oscillation and Its Connection with ENSO." Journal of Climate 14(13): 3055-3061.

Kessler, W. S. (2002). "Is ENSO a cycle or a series of events?" Geophysical Research Letters 29(23): 40-41-40-44.

Kiladis, G. N. and H. F. Diaz (1986). "An Analysis of the 1877–78 ENSO Episode and Comparison with 1982–83." Monthly Weather Review 114(6): 1035-1047.

Kim, H.-M., et al. (2011). "Modulation of North Pacific Tropical Cyclone Activity by Three Phases of ENSO." Journal of Climate 24(6): 1839-1849.

"Klaus Wolter awarded International Journal of Climatology Prize in 2014". NOAA's Earth System Research Laboratory (ESRL) Physical Sciences Division (PSD). Web. 21 June 2019. https://www.esrl.noaa.gov/psd/news/2015/022715.html

Kobayashi, S., et al. (2015). "The JRA-55 Reanalysis: General Specifications and Basic Characteristics." Journal of the Meteorological Society of Japan. Ser. II 93(1): 5-48.

Ku, H. H. (1966). "Notes on the use of propagation of error formulas." Journal of Research of the National Bureau of Standards 70(4): 263-273.

Kug, J.-S. and I.-S. Kang (2006). "Interactive feedback between ENSO and the Indian Ocean." Journal of Climate 19(9): 1784-1801.

Kug, J.-S., et al. (2006). "Interactive feedback between ENSO and the Indian Ocean in an interactive ensemble coupled model." Journal of Climate 19(24): 6371-6381.

Laloyaux, P., et al. (2018). "CERA-20C: A Coupled Reanalysis of the Twentieth Century." Journal of Advances in Modeling Earth Systems 10(5): 1172-1195.

Larson, S. M. and B. P. Kirtman (2014). "The Pacific Meridional Mode as an ENSO Precursor and Predictor in the North American Multimodel Ensemble." Journal of Climate 27(18): 7018-7032.

Latif, M., Kleeman, R., and Eckert, C.: Greenhouse Warming, Decadal Variability, or El Nino? An attempt to understand the ˜ anomalous 1990s, J. Climate, 10, 2221–2239, 1997.

Latif, M., et al. (2015). "Super El Niños in response to global warming in a climate model." Climatic Change 132(4): 489-500.

Lau, N.-C. and M. J. Nath (1996). "The Role of the "Atmospheric Bridge" in Linking Tropical Pacific ENSO Events to Extratropical SST Anomalies." Journal of Climate 9(9): 2036-2057.

Le Blancq, F. (2011). "Diurnal pressure variation: the atmospheric tide." Weather 66(11): 306-307.

Lenssen, N., G. Schmidt, J. Hansen, M. Menne, A. Persin, R. Ruedy, and D. Zyss, 2019: Improvements in the GISTEMP uncertainty model. J. Geophys. Res. Atmos., 124, no. 12, 6307-6326, doi:10.1029/2018JD029522.

Letnic, M., et al. (2005). "The responses of mammals to La Nina (El Nino Southern Oscillation)–associated rainfall, predation, and wildfire in central Australia." Journal of mammalogy 86(4): 689-703.

Liu, P. (2014). "MJO structure associated with the higher-order CEOF modes." Climate Dynamics 43(7-8): 1939-1950.

Liu, W., et al. (2015). "Extended Reconstructed Sea Surface Temperature Version 4 (ERSST.v4): Part II. Parametric and Structural Uncertainty Estimations." Journal of Climate 28(3): 931-951.

Lübbecke, J. F. and M. J. McPhaden (2017). "Symmetry of the Atlantic Niño mode." Geophysical Research Letters 44(2): 965-973

Madden, R. A. and P. R. Julian (1971). "Detection of a 40–50 Day Oscillation in the Zonal Wind in the Tropical Pacific." Journal of the Atmospheric Sciences 28(5): 702-708.

Mantua, N. J., et al. (1997). "A Pacific Interdecadal Climate Oscillation with Impacts on Salmon Production**." Bulletin of the American Meteorological Society 78(6): 1069-1080.

Marshall, A. G., et al. (2015). "Initiation and amplification of the Ningaloo Niño." Climate Dynamics 45(9-10): 2367-2385.

Matsuno, T. (1966). "Quasi-Geostrophic Motions in the Equatorial Area." Journal of the Meteorological Society of Japan. Ser. II 44(1): 25-43.

McCreary, J. (1976). "Eastern Tropical Ocean Response to Changing Wind Systems: with Application to El Niño." Journal of Physical Oceanography 6(5): 632-645.

McGowan, H. and A. Theobald (2017). "ENSO Weather and Coral Bleaching on the Great Barrier Reef, Australia." Geophysical Research Letters 44(20): 10,601-610,607.

McGregor, S., et al. (2010). "A unified proxy for ENSO and PDO variability since 1650." Climate of the Past 6(1).

McPhaden, M. J. (1993). "TOGA-TAO and the 1991–93 El Niño-Southern oscillation event." Oceanography 6(2): 36-44.

McPhaden, M. J. (1999). "Genesis and evolution of the 1997-98 El Niño." Science 283(5404): 950-954.

McPhaden, M. J., et al. (2015). "The Curious Case of the El Niño That Never Happened: A Perspective from 40 Years of Progress in Climate Research and Forecasting." Bulletin of the American Meteorological Society 96(10): 1647-1665.

Mears, C. A. and F. J. Wentz, (2017) A satellite-derived lower tropospheric atmospheric temperature dataset using an optimized adjustment for diurnal effects , Journal of Climate, 30(19), 7695-7718, doi: 10.1175/jcli-d-16-0768.1.

Monahan, A. H., et al. (2009). "Empirical Orthogonal Functions: The Medium is the Message." Journal of Climate 22(24): 6501-6514.

Morice, C. P., et al. (2012). "Quantifying uncertainties in global and regional temperature change using an ensemble of observational estimates: The HadCRUT4 data set." Journal of Geophysical Research: Atmospheres 117(D8).

Neelin, J. D., et al. (1998). "ENSO theory." Journal of Geophysical Research: Oceans 103(C7): 14261-14290.

Nnamchi, H. C., et al. (2015). "Thermodynamic controls of the Atlantic Niño." Nature Communications 6: 8895.

Nnamchi, H. C., et al. (2016). "An Equatorial–Extratropical Dipole Structure of the Atlantic Niño." Journal of Climate 29(20): 7295-7311.

(2006). Objectively Analyzed Air-Sea Fluxes (OAFlux) For Global Oceans, By Lisan Yu et al. Boulder, CO, Research Data Archive at the National Center for Atmospheric Research, Computational and Information Systems Laboratory.

Ohba, M. and H. Ueda (2007). "An impact of SST anomalies in the Indian Ocean in acceleration of the El Niño to La Niña transition." Journal of the Meteorological Society of Japan. Ser. II 85(3): 335-348.

Okumura, Y. M. and C. Deser (2010). "Asymmetry in the Duration of El Niño and La Niña." Journal of Climate 23(21): 5826-5843.

Okumura, Y. M., et al. (2011). "A proposed mechanism for the asymmetric duration of El Niño and La Niña." Journal of Climate 24(15): 3822-3829.

Oldenborgh, G., KNMI Climate Explorer. Retrieved from: https://climexp.knmi.nl/about.cgi?id=someone@somewhere

Oliver, E. C. J., et al. (2018). "Longer and more frequent marine heatwaves over the past century." Nature Communications 9(1): 1324.

Parker, W. S. (2016). "Reanalyses and Observations: What's the Difference?" Bulletin of the American Meteorological Society 97(9): 1565-1572.

Philander, S. G. H. (1981). "The Response of Equatorial Oceans to a Relaxation of the Trade Winds." Journal of Physical Oceanography 11(2): 176-189.

Poli, P., et al. (2016). "ERA-20C: An Atmospheric Reanalysis of the Twentieth Century." Journal of Climate 29(11): 4083-4097.

Power, S. and Smith, I. N.: Weakening of the Walker Circulation and apparent dominance of El Nino both reach record levels, but has ENSO really changed?, Geophys. Res. Lett., 34, 18702, doi:10.1029/2007GL030854, 2007

Quadrelli, R. and J. M. Wallace (2002). "Dependence of the structure of the Northern Hemisphere annular mode on the polarity of ENSO." Geophysical Research Letters 29(23): 47-41-47-44.

Randel, W. J., et al. (2009). "ENSO influence on zonal mean temperature and ozone in the tropical lower stratosphere." Geophysical Research Letters 36(15).

Rasmusson, E. M. and T. H. Carpenter (1982). "Variations in Tropical Sea Surface Temperature and Surface Wind Fields Associated with the Southern Oscillation/El Niño." Monthly Weather Review 110(5): 354-384.

Rayner, N. A., et al. (2006). "Improved Analyses of Changes and Uncertainties in Sea Surface Temperature Measured In Situ since the Mid-Nineteenth Century: The HadSST2 Dataset." Journal of Climate 19(3): 446-469.

Renwick, J. A. and J. M. Wallace (1996). "Relationships between North Pacific Wintertime Blocking, El Niño, and the PNA Pattern." Monthly Weather Review 124(9): 2071-2076.

Reynolds, R. W. (1988). "A Real-Time Global Sea Surface Temperature Analysis." Journal of Climate 1(1): 75-87.

Reynolds, R. W. and T. M. Smith (1994). "Improved Global Sea Surface Temperature Analyses Using Optimum Interpolation." Journal of Climate 7(6): 929-948.

Reynolds, R. W., et al. (2002). "An Improved In Situ and Satellite SST Analysis for Climate." Journal of Climate 15(13): 1609-1625.

Rienecker, M. M., et al. (2011). "MERRA: NASA's Modern-Era Retrospective Analysis for Research and Applications." Journal of Climate 24(14): 3624-3648.

Ropelewski, C. F. and P. D. Jones (1987). "An extension of the Tahiti–Darwin southern oscillation index." Monthly Weather Review 115(9): 2161-2165.

Roundy, P. E. and G. N. Kiladis (2006). "Observed Relationships between Oceanic Kelvin Waves and Atmospheric Forcing." Journal of Climate 19(20): 5253-5272.

Roundy, P.E., (2012): Tropical-extratropical interactions. Intraseasonal Variability of the Atmosphere-Ocean Climate System, 2nd ed. W. K. -M. Lau and D. E. Waliser, Eds., Springer, 497-512

Roundy, P. E. (2015). "On the Interpretation of EOF Analysis of ENSO, Atmospheric Kelvin Waves, and the MJO." Journal of Climate 28(3): 1148-1165.

Rowntree, P. R. (1972). "The influence of tropical east Pacific Ocean temperatures on the atmosphere." Quarterly Journal of the Royal Meteorological Society 98(416): 290-321.

Saha, S., et al. (2010). "The NCEP Climate Forecast System Reanalysis." Bulletin of the American Meteorological Society 91(8): 1015-1058.

Santoso, A., et al. (2017). "The defining characteristics of ENSO extremes and the strong 2015/2016 El Niño." Reviews of Geophysics 55(4): 1079-1129.

Slingo, J. M. and H. Annamalai (2000). "1997: The El Niño of the Century and the Response of the Indian Summer Monsoon." Monthly Weather Review 128(6): 1778-1797.

Smith, C. A. and P. D. Sardeshmukh (2000). "The effect of ENSO on the intraseasonal variance of surface temperatures in winter." International Journal of Climatology 20(13): 1543-1557.

Smith, T. M., et al. (2008). "Improvements to NOAA's Historical Merged Land–Ocean Surface Temperature Analysis (1880–2006)." Journal of Climate 21(10): 2283-2296.

Stuecker, M. F. (2018). "Revisiting the Pacific Meridional Mode." Scientific Reports 8(1): 3216.

Suarez, M. J. and P. S. Schopf (1988). "A Delayed Action Oscillator for ENSO." Journal of the Atmospheric Sciences 45(21): 3283-3287.

Swetnam, T. and T. Batancourt (1993). Temporal patterns of El Niño/Southern Oscillation-wildfire teleconnections in the southwestern United States. El Niño: historical and paleoclimatic aspects of the Southern Oscillation, Cambridge University Press: 259-270.

Tang, Y. and B. Yu (2008). "MJO and its relationship to ENSO." Journal of Geophysical Research: Atmospheres 113(D14).

Tangang, F., et al. (2018). "ENSO modulation of seasonal rainfall and extremes in Indonesia." Climate Dynamics 51(7-8): 2559-2580.

Thompson, D. W., et al. (2008). "A large discontinuity in the mid-twentieth century in observed global-mean surface temperature." Nature 453(7195): 646-649.

Titchner, H. A. and N. A. Rayner (2014). "The Met Office Hadley Centre sea ice and sea surface temperature data set, version 2: 1. Sea ice concentrations." Journal of Geophysical Research: Atmospheres 119(6): 2864-2889.

Tokinaga, H., et al (2019). "ENSO influence on the Atlantic Niño, revisited: Multi-year versus single-year ENSO events." Journal of Climate:

Tozuka, T., et al. (2014). "Locally and remotely forced atmospheric circulation anomalies of Ningaloo Niño/Niña." Climate Dynamics 43(7-8): 2197-2205.

Trenberth, K. E. (1984). "Signal versus noise in the Southern Oscillation." Monthly Weather Review 112(2): 326-332.

Trenberth, K. E. and T. J. Hoar (1996). "The 1990–1995 El Niño-Southern Oscillation Event: Longest on Record." Geophysical Research Letters 23(1): 57-60.

Trenberth, K. E. and T. J. Hoar (1997). "El Niño and climate change." Geophysical Research Letters 24(23): 3057-3060.

Trouet, V. and G. J. Van Oldenborgh (2013). "KNMI Climate Explorer: a web-based research tool for high-resolution paleoclimatology." Tree-Ring Research 69(1): 3-13.

Troup, A.J. (1965), The ‘southern oscillation’. Q.J.R. Meteorol. Soc., 91: 490-506. https://doi.org/10.1002/qj.49709139009

Vimont, D. J., et al. (2003). "The Seasonal Footprinting Mechanism in the Pacific: Implications for ENSO." Journal of Climate 16(16): 2668-2675.

Wang, C. (2001). "A unified oscillator model for the El Niño–Southern Oscillation." Journal of Climate 14(1): 98-115.

Webster, P. J. (1981). "Mechanisms Determining the Atmospheric Response to Sea Surface Temperature Anomalies." Journal of the Atmospheric Sciences 38(3): 554-571.

Wheeler, M. C. and H. H. Hendon (2004). "An All-Season Real-Time Multivariate MJO Index: Development of an Index for Monitoring and Prediction." Monthly Weather Review 132(8): 1917-1932.

Wolter, K. and M. S. Timlin (1993). Monitoring ENSO in COADS with a seasonally adjusted principal component index.

Wolter, K. and M. S. Timlin (1998). "Measuring the strength of ENSO events: How does 1997/98 rank?" Weather 53(9): 315-324.

Wolter, K. and M. S. Timlin (2011). "El Niño/Southern Oscillation behaviour since 1871 as diagnosed in an extended multivariate ENSO index (MEI.ext)." International Journal of Climatology 31(7): 1074-1087.

Woodruff, S. D., et al. (2011). "ICOADS Release 2.5: extensions and enhancements to the surface marine meteorological archive." International Journal of Climatology 31(7): 951-967.

Wright, P. B. (1989). "Homogenized long-period Southern Oscillation indices." International Journal of Climatology 9(1): 33-54.

Wu, X., et al. (2019). "What Controls the Duration of El Niño and La Niña Events?" Journal of Climate 32(18): 5941-5965.

Wu, Z. and N. E. Huang (2004). "A study of the characteristics of white noise using the empirical mode decomposition method." Proceedings of the Royal Society of London. Series A: Mathematical, Physical and Engineering Sciences 460(2046): 1597-1611.

Wyrtki, K. (1975). "El Niño—the dynamic response of the equatorial Pacific Ocean to atmospheric forcing." Journal of Physical Oceanography 5(4): 572-584.

Xu, K., et al. (2017). "CMIP5 Projections of Two Types of El Niño and Their Related Tropical Precipitation in the Twenty-First Century." Journal of Climate 30(3): 849-864.

Xue, Y., et al. (2003). "Interdecadal Changes of 30-Yr SST Normals during 1871–2000." Journal of Climate 16(10): 1601-1612.

Yadav, R. K., et al. (2018). "Atlantic Niño modulation of the Indian summer monsoon through Asian jet." npj Climate and Atmospheric Science 1(1): 23.

Yu, L., et al. (2008). "Multidecade Global Flux Datasets from the Objectively Analyzed Air-sea Fluxes (OAFlux) Project: Latent and sensible heat fluxes, ocean evaporation, and related surface meteorological variables. OAFlux Project Technical Report. OA-2008-01, 64pp."

Zebiak, S. E. (1982). "A Simple Atmospheric Model of Relevance to El Niño." Journal of the Atmospheric Sciences 39(9): 2017-2027.

Zebiak, S. E. and M. A. Cane (1987). "A Model El Nino–Southern Oscillation." Monthly Weather Review 115(10): 2262-2278.

Zhang, C., et al. (2001). "A workshop on the MJO and ENSO." Bulletin of the American Meteorological Society 82(5): 971-976.

Zhang, C. (2005). "Madden-Julian Oscillation." Reviews of Geophysics 43(2).

Zhang, L., et al. (2009). "Linking the Pacific Meridional Mode to ENSO: Coupled Model Analysis." Journal of Climate 22(12):

Zhang, C. (2013). "Madden–Julian Oscillation: Bridging Weather and Climate." Bulletin of the American Meteorological Society 94(12): 1849-1870.

Zhang, H., et al. (2014). "The South Pacific Meridional Mode: A Mechanism for ENSO-like Variability." Journal of Climate 27(2): 769-783.

Zhang, N., et al. (2017). "Opposite polarities of ENSO drive distinct patterns of coral bleaching potentials in the southeast Indian Ocean." Scientific Reports 7(1): 2443.

Zhang, H., et al. (2019). "Improving the CPC's ENSO Forecasts using Bayesian model averaging." Climate Dynamics 53(5-6): 3373-3385.

Zhao, H. and C. Wang (2019). "On the relationship between ENSO and tropical cyclones in the western North Pacific during the boreal summer." Climate Dynamics 52(1-2): 275-288

Zhu, P., et al. (2007). "Climate sensitivity of tropical and subtropical marine low cloud amount to ENSO and global warming due to doubled CO2." Journal of Geophysical Research: Atmospheres 112(D17).

Zhu, J., et al. (2018). "Response of tropical terrestrial gross primary production to the super El Niño event in 2015." Journal of Geophysical Research: Biogeosciences 123(10): 3193-3203.

Table 1. SST Datasets used in the MEI.extv2. Dataset name, temporal range, native resolution, reference, and the corresponding release year are presented.

MEI.extv2 SST Datasets				
Dataset	Temporal Range	Resolution	Reference	Release Year
HADISST2.1	1850-2007	1x1°	Titchner & Rayner (2014)	2014
NOAA's 20CRv3	1850-2015	1x1°	Slivinski et al (2019)	2019
COBE SST2	1850-2018	1x1°	Hirahara et al (2014)	2014
NOAA's 20CRv2c	1851-2014	2x2°	Compo et al (2011)	2015
ERSSTv5	1854-2020	2x2°	Huang et al (2017)	2017
ERSSTv4	1854-2020	2x2°	Huang et al (2015)	2015
Kaplan Extended v2	1856-2020	5x5°	Kaplan et al (1998)	1998
HADISST	1870-2020	1x1°	Rayner et al (2003)	2003
NOAA's 20CRv2	1871-2012	2x2°	Compo et al (2011)	2013
COBE SST	1891-2020	1x1°	Ishii et al (2004)	2005
ERA-20C	1900-2010	1x1°	Simmons et al (2016)	2016
ERA-20CM	1900-2010	1x1°	Hersbach et al (2015)	2015
CERA-20C	1901-2010	1x1°	Laloyaux et al (2018)	2018
NCEP-R1	1948-2020	2.5x2.5°	Kalnay et al (1996)	1996
JRA-55	1958-2020	2.5x2.5°	Kobyashi et al (2015)	2015
WHOI OA Flux v3	1958-2019	2.5x2.5°	Yu et al (2008)	2008

Table 2. SLP Datasets used in the MEI.extv2. Dataset name, temporal range, native resolution, reference, and the corresponding release year are presented.

MEI.extv2 SLP Datasets				
Dataset	Temporal Range	Resolution	Reference	Release Year
NOAA's 20CRv3	1836-2015	1x1°	Slivinski et al (2019)	2019
HADSLP2r	1855-2019	5x5°	Allan & Ansell (2006)	2006
NOAA 20CRv2c	1860-2014	2x2°	Compo et al (2011)	2015
Kaplan SLP	1865-2001	4x4°	Kaplan et al (2000)	2000
Jones/CRU SOI	1866-2020	2.5x2.5°	Ropelowski & Jones (1987)	1987
NOAA 20CRv2	1871-2012	2x2°	Compo et al (2011)	2013
HADSLP	1871-1998	5x5°	Basnett & Parker (1997)	1997
Australia BOM SOI	1876-2020	N/A	Troup (1965)	1965
ERA-20C	1900-2010	1x1°	Simmons et al (2016)	2016
ERA-20CM	1900-2010	1x1°	Hersbach et al (2015)	2015
CERA-20C	1901-2010	1x1°	Laloyaux et al (2018)	2018
NCEP-R1	1948-2020	2.5x2.5°	Kalnay et al (1996)	1996
NOAA ER SLP	1950-1997	2x2°	Smith & Reynolds (2004)	2004
JRA-55	1958-2020	1.25x1.25°	Kobyashi et al (2015)	2015

Table 3. MEI.v1 (left), MEI.ext (second from the left), MEI.v2 (second from the right), and MEI.extv2 (right) comparison table with the following parameters (from top to bottom): Dataset(s) used, spatial resolution, temporal range, method(s), EOF "training" period, variables used, EOF domain, EOF weighting, basic state adjustments for changes in background climate or observations, uncertainty quantification.

MEIv1, MEI.ext, MEI.v2 and MEI.extv2 Comparison				
	MEIv1	MEI.ext	MEI.v2	MEI.extv2
Dataset(s)	ICOADSv2.5 only	HADSST2 (SST), HADSLP2 (SLP)	JRA-55	15 SST Datasets, 14 SLP Datasets
Spatial Resolution	All variables 2x2 degree	All variables and datasets 5x5 degree	All variables 1.25x1.25 degree	All datasets converted to 5x5° grid. All datasets spatially and temporally complete
Temporal Range	1950-2019	1871-2005	1979-Present	1865-near present
Method	EOF only	EOF only	EOF only	EOF and box averages used
EOF "Training" Period	1950-1993	1871-2005	1979-2018	Variable (dependent on dataset length)
Variables	SST, Surface Air Temperature, SLP, U Wind, V Wind, Cloudiness (fraction of sky)	SST and SLP	SST, SLP, U wind, V Wind, OLR	SST and SLP
EOF Domain	All EOFs: (100E-80W, 30S-30N)	All EOFs: (100E-80W, 30S-30N)	All EOFs: (100E-80W, 30S-30N)	SST EOF: (160E-80W, 15N-20S) SST box: (180W-80W, 5S-5N) SLP EOF: (100E-80W, 30S-20N) SLP box: (closest grid points to Darwin and Tahiti)
EOF Weighting	None	None	None	SLP and SST are EOFs weighted by explained variance, number of datasets, inter-dataset variability,
Climate/ Observational Background State Adjustments	None	None	None	Large suite of sliding base period(s) and detrending. Weighting equation implemented to account for observation differences
Uncertainty Quantification?	None	None	Perturbed ensemble experiments performed in Zhang et al (2019)	~ 26,000 "realizations" based on measures of center, varying base period window size, updating frequency, and juxtaposition.

Table 4. MEI.extv2 ENSO Phase (far left), (Bi-monthly) ranks (second from left), percentiles (second from right), and corresponding standardized MEI anomaly ($\boldsymbol{\sigma}$) (1865-2019).

Extended MEI.v2 ENSO Phase, Intensity, Ranks, Percentiles & Standardized Anomalies Table (1865-2019)			
ENSO Phase and Intensity	**Ranks**	**Percentiles**	**Stand. Anomaly**
Super El Nino	1-5	< 3%	>+1.83
Strong El Nino	6-15	3-10%	+1.23 - +1.79
Moderate El Nino	16-31	10-20%	+0.73 - +1.23
Weak El Nino	32-51	20-33%	+0.37 - +0.73
Neutral ENSO	52-103	33-67%	+0.37 - -0.40
Weak La Nina	104-123	67-80%	-0.40 - -0.78
Moderate La Nina	124-140	80-90%	-0.78 - -1.15
Strong La Nina	141-150	90-97%	-1.15 - -1.53
Super La Nina	151-155	> 97%	< -1.53

Table 5. MEI.extv2 Top 10 strongest El Ninos (1865-2019), with the following parameters (from left to right): rank, year of occurrence, peak bi-monthly period, peak bi-monthly value (via ensemble median analysis), corresponding ENSO event phase and intensity (top 5 El Ninos are "Super"), probability of Super El Nino (based on realisations), probability of El Nino (based on realisations), uncertainty (via equation 3), and uncertainty in terms of rank. Super El Nino and El Nino probabilities of 100% based on the MEI.extv2 realisations are highlighted (in yellow), bolded, and italicized.

Extended MEI Version 2 (MEI.extv2) Top 10 Strongest El Ninos (1865-2019)								
RANK	**Year**	**Peak Bi-Monthly**	**Peak Bi-Monthly Value (Ensemble Median)**	**ENSO Event Phase & Intensity**	**Probability of Super El Nino**	**Probability of El Nino**	**Uncertainty (σ)**	**Rank Uncertainty**
1	**1997**	**AUG-SEP**	2.94	**SUPER EL NINO**	***100%***	***100%***	0.46	**1-3**
2	**1878**	**JAN-FEB**	2.85	**SUPER EL NINO**	91%	***100%***	0.57	**1-4**
3	**1983**	**JAN-FEB**	2.72	**SUPER EL NINO**	***100%***	***100%***	0.46	**1-4**
4	**2015**	**AUG-SEP**	2.50	**SUPER EL NINO**	***100%***	***100%***	0.52	**1-5**
5	**1889**	**JAN-FEB**	2.09	**SUPER EL NINO**	75%	94%	0.54	4 - 14
6	**1941**	**APR-MAY**	1.97	**STRONG EL NINO**	62%	97%	**0.74**	4 - 23
7	**1902**	**JUL-AUG**	1.92	**STRONG EL NINO**	50%	***100%***	0.51	5 - 17
8	**1987**	**JUL-AUG**	1.87	**STRONG EL NINO**	54%	***100%***	0.37	5 - 15
9	**1905**	**JUN-JUL**	1.84	**STRONG EL NINO**	51%	***100%***	0.56	5 - 21
10	**1900**	**MAR-APR**	1.77	**STRONG EL NINO**	35%	***100%***	0.52	5 - 23

Table 6. ENSO Indices correlation (R) and mean squared error (MSE) table (1876-2005). Top row (left column) from left to right (top to bottom): MEI.extv2 weighted ensemble median, MEI.extv2 SST ensemble median, MEI.ext, MEI.ext (linearly detrended), Bivariate ENSO Index Time series (BEST), and Oceanic Nino Index (ONI). Boxes with R values $\geq$ 0.95 are denoted in bold.

ENSO Indices Correlation & Mean Squared Error (1876-2005)								
Indices	**MEI.extv2 Weighted Median**	**MEI.extv2 SST Ens Median**	**MEI.extv2 SLP Ens Median**	**MEI.ext**	**MEI.ext (detrend)**	**BEST**	**SOI (BOM)**	**ONI**
MEI.extv2	-							
MEI.extv2 SST Ens Median	**R: 0.99 MSE: 0.02**	-						
MEI.extv2 SLP Ens Median	R: 0.93 MSE: 0.11	R: 0.88 MSE: 0.20	-					
MEI.ext	**R: 0.95 MSE:0.11**	R: 0.93 MSE: 0.13	R: 0.91 MSE: 0.18	-				
MEI.ext (detrend)	**R: 0.96 MSE:0.07**	**R: 0.95 MSE: 0.09**	R: 0.91 MSE: 0.16	**R: 0.98 MSE:0.04**	-			
BEST	R: 0.92 MSE:0.13	R: 0.90 MSE: 0.18	R: 0.92 MSE: 0.12	R: 0.90 MSE: 0.19	R: 0.90 MSE: 0.19	-		
SOI (BOM)	R: -0.77 MSE: 3.23	R: -0.73 MSE: 3.29	R: -0.84 MSE: 3.25	R: -0.75 MSE: 3.48	R: -0.74 MSE: 3.43	R: -0.91 MSE: 3.20	-	
ONI	**R: 0.97 MSE: 0.07**	**R: 0.97 MSE: 0.06**	R: 0.88 MSE: 0.24	R: 0.92 MSE: 0.16	R: 0.94 MSE: 0.13	R: 0.90 MSE: 0.19	R: -0.72 MSE: 3.47	-

Table 7. MEI.extv2 (boreal) winter (Oct-Mar) ENSO events table (1865-2020) based on the weighted, ensemble median analysis. ENSO events are sorted in each according to the number of consecutive boreal winters they last, with El Nino (La Nina) winters shaded in red (blue).

MEI.extv2 Winter ENSO Events Table (1865-2020)						
3 YR EL NINO	2 YR EL NINO	1 YR EL NINO	1 YR LA NINA	2 YR LA NINA	3 YR LA NINA	4 YR LA NINA
1939-42	1876-78	1868-69	1869-70	1949-51	1892-95	1872-76
2002-05	1884-86	1880-81	1879-80	1961-63	1908-11	
	1895-97	1888-89	1886-87	1970-72	1915-18	
	1899-01	1902-03	1889-90	1984-86	1954-57	
	1904-06	1911-12	1898-99	1995-97	1973-76	
	1913-15	1923-24	1903-04	2007-09	1998-01	
	1918-20	1925-26	1906-07	2010-12		
	1929-31	1951-52	1922-23			
	1957-59	1963-64	1924-25			
	1968-70	1965-66	1933-34			
	1976-78	1972-73	1938-39			
	1986-88	1979-80	1942-43			
	2014-16	1982-83	1964-65			
	2018-20	1991-92	1967-68			
		1994-95	1988-89			
		1997-98	2005-06			
		2006-07	2017-18			
		2009-10				

Table 8. MEI.extv2 Top 10 strongest La Ninas (1865-2019), with the following parameters (from left to right): rank, year of occurrence, peak bi-monthly period, peak bi-monthly value (via ensemble median analysis), corresponding ENSO event phase and intensity (top 5 La Ninas are "Super"), probability of Super La Nina (based on realisations), probability of La Nina (based on realisations), uncertainty (via equation 3), and uncertainty in terms of rank. Super La Nina and La Nina probabilities of 100% based on the MEI.extv2 realisations are highlighted (in yellow), bolded, and italicized.

Extended MEI Version 2 (MEI.extv2) Top 10 Strongest La Ninas (1865-2019)								
RANK	Year	Peak Bi-Monthly	Peak Bi-Monthly Value (Ensemble Median)	ENSO Event Phase & Intensity	Probability of Super La Nina	Probability of La Nina	Uncertainty (σ)	Rank Uncertainty
1	1975	SEP-OCT	-2.07	SUPER LA NINA	98%	***100%***	0.40	1-9
2	1916	NOV-DEC	-2.03	SUPER LA NINA	79%	***100%***	**0.74**	1-18
3	1973	DEC-JAN	-1.96	SUPER LA NINA	99%	***100%***	0.39	1-10
4	1910	MAR-APR	-1.95	SUPER LA NINA	73%	96%	**0.73**	1-20
5	2010	SEP-OCT	-1.93	SUPER LA NINA	94%	***100%***	0.36	1-10
6	1971	FEB-MAR	-1.84	STRONG LA NINA	82%	***100%***	0.53	1-18
7	1988	OCT-NOV	-1.81	STRONG LA NINA	93%	***100%***	0.22	2-10
8	1955	OCT-NOV	-1.79	STRONG LA NINA	79%	***100%***	0.36	1-13
9	2008	JAN-FEB	-1.79	STRONG LA NINA	89%	***100%***	0.29	1-13
10	1892	OCT-NOV	-1.66	STRONG LA NINA	46%	90%	0.38	2-18

Table 9. ENSO Indices correlation (R) table (1979-2005). Top row (left column) from left to right (top to bottom): MEI.extv2 weighted ensemble median, MEI.ext, MEI.v1, BEST, SOI, and the ONI. Boxes with R values ≥ 0.95 are denoted in bold.

ENSO Indices Correlation Table (1979-2005)							
Indices	**MEI.extv2**	**MEI.ext**	**MEI**	**MEI.v2**	**BEST**	**SOI (BOM)**	**ONI**
MEI.extv2	-						
MEI.ext	**0.976**	-					
MEI	**0.957**	**0.974**	-				
MEI.v2	0.932	**0.950**	**0.956**	-			
BEST	0.920	0.915	0.918	0.922	-		
SOI (BOM)	-0.830	-0.826	-0.836	-0.850	-0.946	-	
ONI	**0.963**	**0.956**	0.943	0.931	0.931	0.807	-

Table 10. Jan-Feb 1932-Jan-Feb 1933 MEI.extv2 table. From left to right: Year-Month (YYYYMM), bi-monthly period, MEI.extv2 weighted, ensemble median value (σ), most likely ENSO phase and intensity (based on MEI.extv2 realisations) (will occasionally differ slightly from the weighted median output), El Nino probability (%) (based on MEI.extv2 realisations), Neutral ENSO probability (%) (based on MEI.extv2 realisations), and La Nina probability (%) (based on MEI.extv2 realisations).

Year-Month	Bi-Monthly	MEI.extv2 Ensemble Median	Weighted MEI Ensemble Median ENSO Phase & Intensity (based on percentiles)	Most likely ENSO Phase & Intensity (based on MEI.extv2 member probabilities)	Probability of El Nino (%)	Probability of Neutral ENSO (%)	Probability of La Nina (%)
193201	Jan-Feb	0.091	WARM NEUTRAL	WARM NEUTRAL	19	78	4
193202	Feb-Mar	0.358	WARM NEUTRAL	WARM NEUTRAL	49	51	0
193203	Mar-Apr	0.605	WEAK EL NINO	WEAK EL NINO	83	17	0
193204	Apr-May	0.829	MODERATE EL NINO	MODERATE EL NINO	91	9	0
193205	May-Jun	0.859	MODERATE EL NINO	MODERATE EL NINO	89	11	0
193206	Jun-Jul	0.651	WEAK EL NINO	WEAK EL NINO	93	7	0
193207	Jul-Aug	0.543	WEAK EL NINO	WEAK EL NINO	72	28	0
193208	Aug-Sep	0.464	WEAK EL NINO	WEAK EL NINO	66	34	0
193209	Sep-Oct	0.240	WARM NEUTRAL	WARM NEUTRAL	31	66	2
193210	Oct-Nov	0.101	WARM NEUTRAL	WARM NEUTRAL	8	88	3
193211	Nov-Dec	-0.049	COOL NEUTRAL	COOL NEUTRAL	2	94	4
193212	Dec-Jan	-0.090	COOL NEUTRAL	COOL NEUTRAL	7	90	3
193301	Jan-Feb	-0.166	COOL NEUTRAL	COOL NEUTRAL	3	89	9

Table 11. Nov-Dec 1992-Dec-Jan 1993 MEI.extv2 table. From left to right: Year-Month (YYYYMM), bi-monthly period, MEI.extv2 weighted, ensemble median value (σ), most likely ENSO phase and intensity (based on MEI.extv2 realisations) (will occasionally differ slightly from the weighted median output), El Nino probability (%) (based on MEI.extv2 realisations), Neutral ENSO probability (%) (based on MEI.extv2 realisations), and La Nina probability (%) (based on MEI.extv2 realisations).

Year-Month	Bi-Monthly	MEI.extv2 Ensemble Median	Weighted MEI Ensemble Median ENSO Phase & Intensity (based on percentiles)	Most likely ENSO Phase & Intensity (based on MEI.extv2 member probabilities)	Probability of El Nino (%)	Probability of Neutral ENSO (%)	Probability of La Nina (%)
199211	Nov-Dec	0.225	WARM NEUTRAL	WARM NEUTRAL	49	51	0
199212	Dec-Jan	0.308	WARM NEUTRAL	WARM NEUTRAL	57	43	0
199301	Jan-Feb	0.555	WEAK EL NINO	MODERATE EL NINO	84	16	0
199302	Feb-Mar	0.732	MODERATE EL NINO	MODERATE EL NINO	97	3	0
199303	Mar-Apr	1.077	MODERATE EL NINO	MODERATE EL NINO	97	3	0
199304	Apr-May	1.337	STRONG EL NINO	STRONG EL NINO	100	0	0
199305	May-Jun	1.223	MODERATE EL NINO	STRONG EL NINO	100	0	0
199306	Jun-Jul	0.876	MODERATE EL NINO	MODERATE EL NINO	100	0	0
199307	Jul-Aug	0.569	WEAK EL NINO	MODERATE EL NINO	85	15	0
199308	Aug-Sep	0.505	WEAK EL NINO	WEAK EL NINO	81	19	0
199309	Sep-Oct	0.601	WEAK EL NINO	WEAK EL NINO	92	8	0
199310	Oct-Nov	0.512	WEAK EL NINO	WEAK EL NINO	82	18	0
199311	Nov-Dec	0.375	WEAK EL NINO	WARM NEUTRAL	42	58	0
199312	Dec-Jan	0.330	WARM NEUTRAL	WARM NEUTRAL	31	69	0

Table 12. Dec-Jan 1890-Dec-Jan 1891 MEI.extv2 table. From left to right: Year-Month (YYYYMM), bi-monthly period, MEI.extv2 weighted, ensemble median value (σ), most likely ENSO phase and intensity (based on MEI.extv2 realisations) (will occasionally differ slightly from the weighted median output), El Nino probability (%) (based on MEI.extv2 realisations), Neutral ENSO probability (%) (based on MEI.extv2 realisations), and La Nina probability (%) (based on MEI.extv2 realisations).

Year-Month	Bi-Monthly	MEI.extv2 Ensemble Median	Weighted MEI Ensemble Median ENSO Phase & Intensity (based on percentiles)	Most likely ENSO Phase & Intensity (based on MEI.extv2 member probabilities)	Probability of El Nino (%)	Probability of Neutral ENSO (%)	Probability of La Nina (%)
189012	Dec-Jan	-0.404	COOL NEUTRAL	WEAK LA NINA	1	50	49
189101	Jan-Feb	-0.023	COOL NEUTRAL	COOL NEUTRAL	16	69	14
189102	Feb-Mar	0.284	WARM NEUTRAL	WARM NEUTRAL	49	51	0
189103	Mar-Apr	0.614	WEAK EL NINO	WEAK EL NINO	80	17	3
189104	Apr-May	0.955	MODERATE EL NINO	MODERATE EL NINO	80	17	3
189105	May-Jun	1.001	MODERATE EL NINO	MODERATE EL NINO	83	17	0
189106	Jun-Jul	0.927	MODERATE EL NINO	MODERATE EL NINO	90	10	0
189107	Jul-Aug	0.685	WEAK EL NINO	WEAK EL NINO	91	9	0
189108	Aug-Sep	0.417	WEAK EL NINO	WARM NEUTRAL	59	41	0
189109	Sep-Oct	0.291	WARM NEUTRAL	WARM NEUTRAL	39	61	0
189110	Oct-Nov	0.287	WARM NEUTRAL	WARM NEUTRAL	40	60	0
189111	Nov-Dec	0.167	WARM NEUTRAL	WARM NEUTRAL	20	79	1
189112	Dec-Jan	0.042	WARM NEUTRAL	WARM NEUTRAL	7	89	4

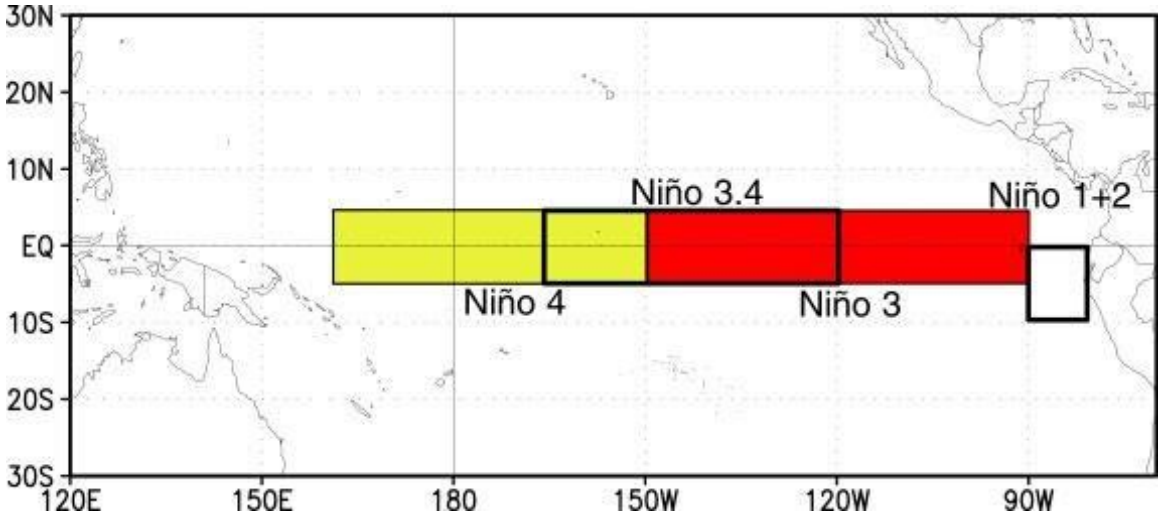

Figure 1. Depiction of the geographic locations of the NINO 1-2, 3, 3.4, & 4 regions as initially diagnosed by Rasmusson and Carpenter (1982) and Barnston et al (1997). Taken from the Climate Prediction Center's *El Nino Regions* page.

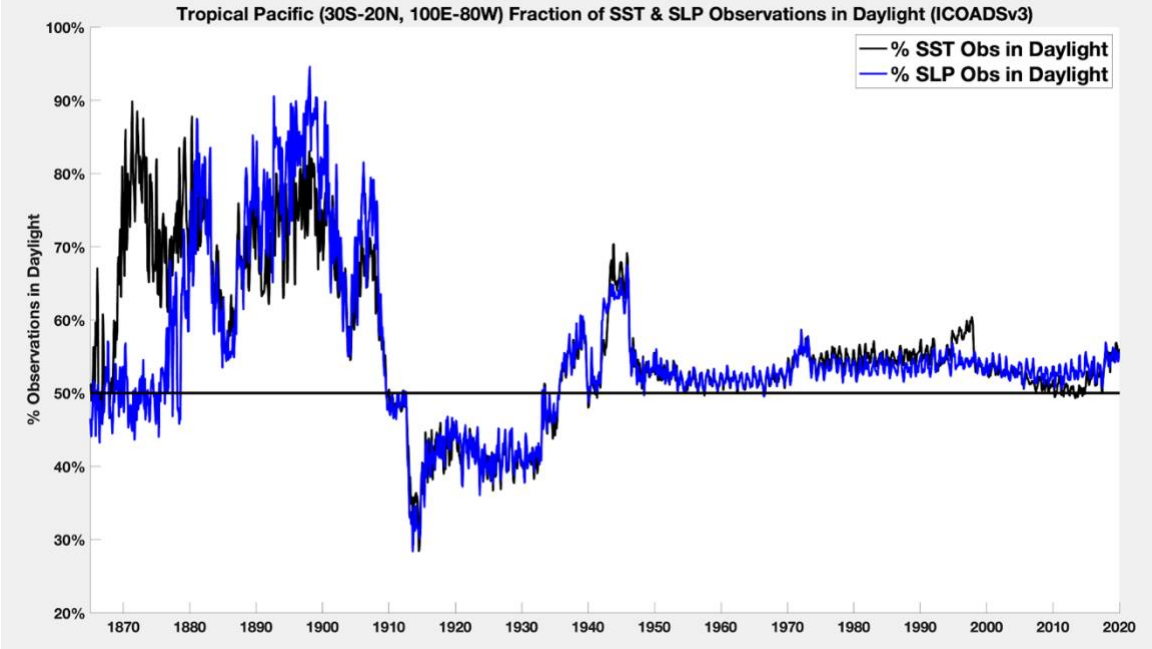

Figure 2. International Comprehensive Ocean-Atmosphere Dataset Release 3.0 (ICOADSv3) fraction of Tropical Pacific (30S-20N, 100E-80W) Sea Surface Temperature (SST) and Sea Level Pressure (SLP) observations collected during daylight hours. Data obtained at NOAA ESRL.

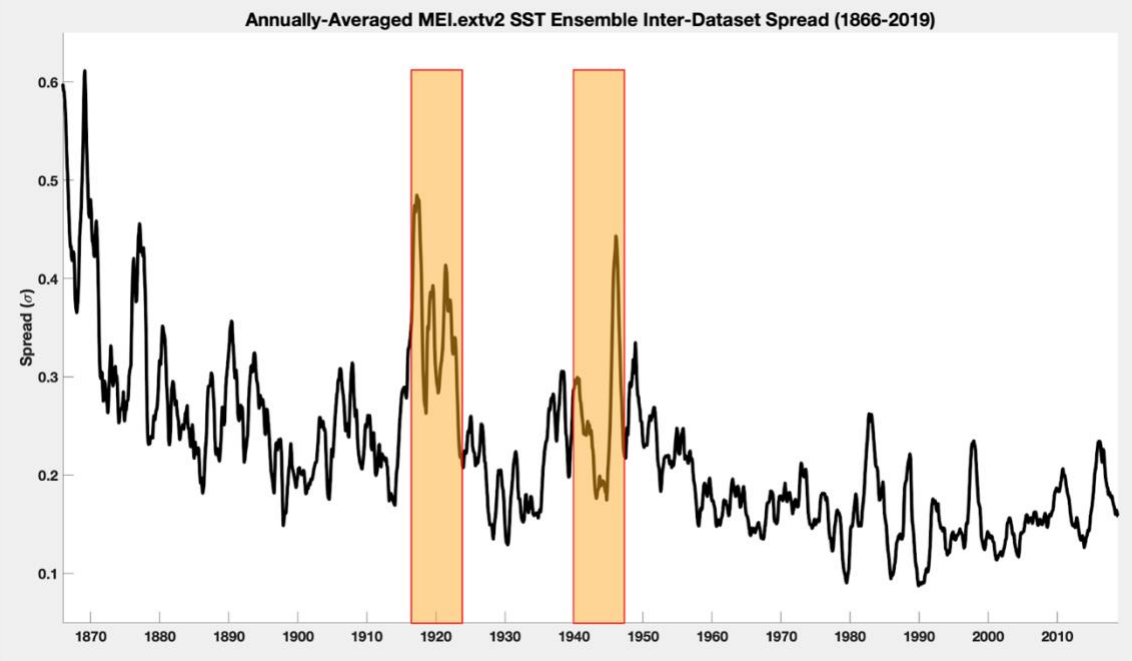

Figure 3. Annually-averaged MEI.extv2 SST ensemble Inter-dataset spread (1866-2019). World War I and II periods are highlighted in orange.

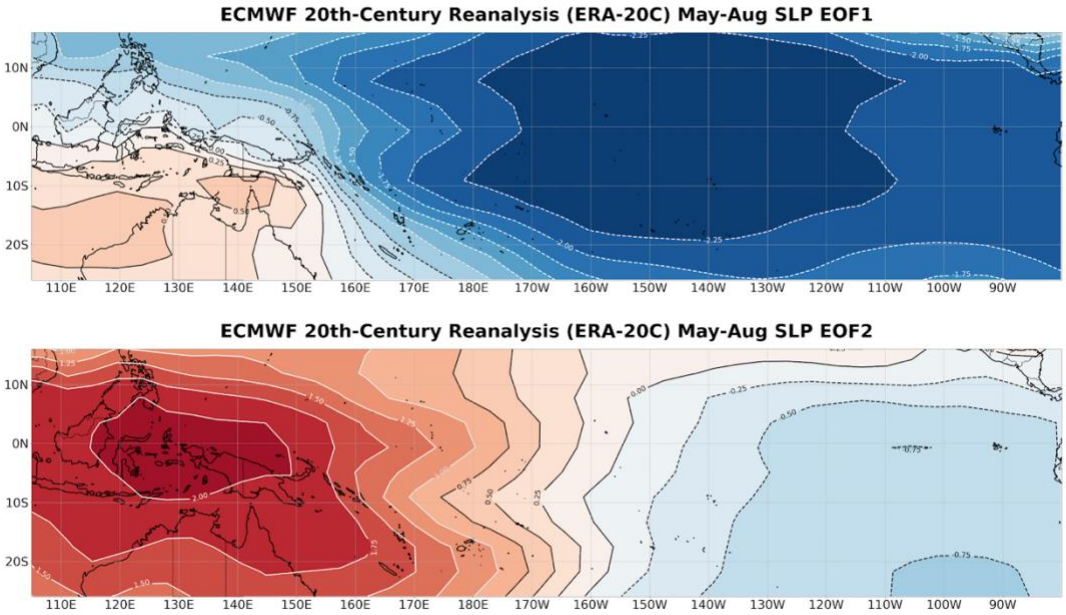

Figure 4. ECMWF 20th-Century Reanalysis (ERA-20C) May-August SLP EOF 1 (top) and SLP EOF 2 (bottom). EOF Temporal range: 1900-2010.

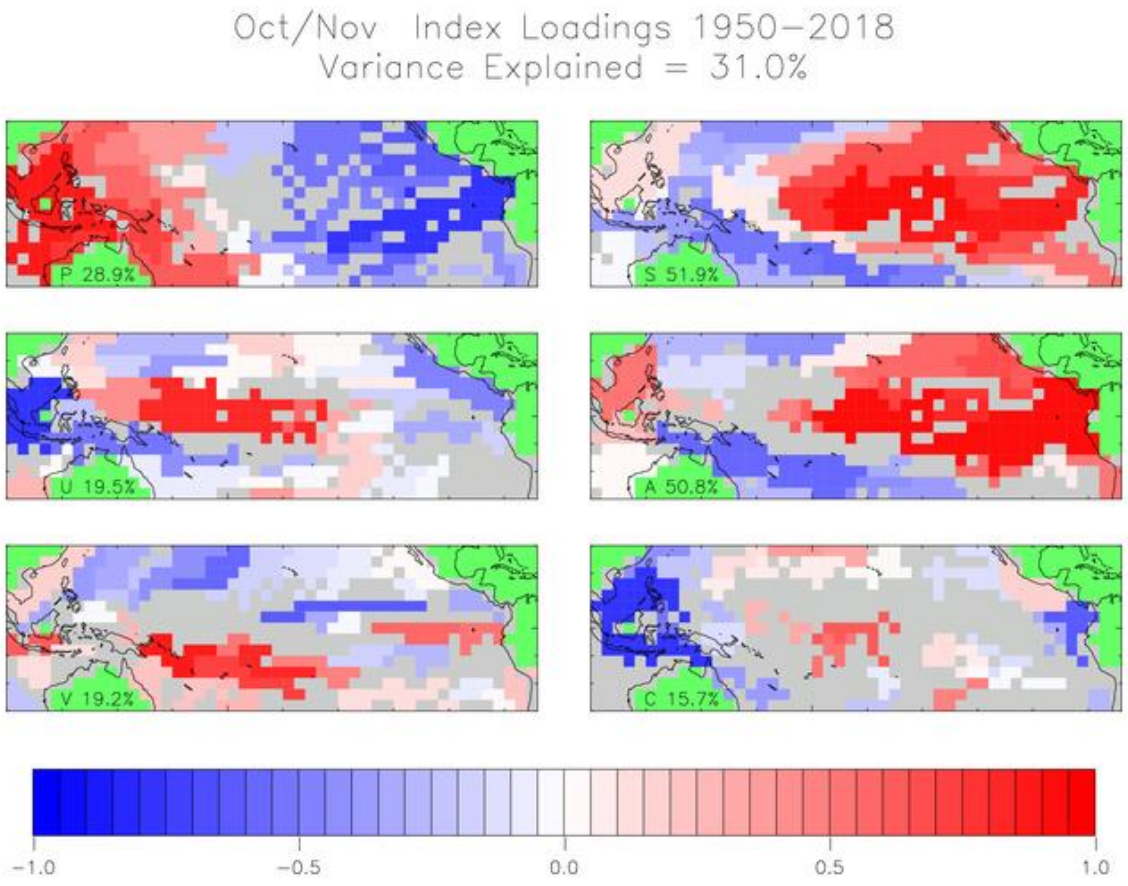

Figure 5. Oct-Nov MEI.v1 EOF-1 loadings for SLP (P) (top left), zonal wind (U) (middle left), meridional wind (V) (bottom left), SST (S) (top right), SAT (A) (middle right), Cloud fraction of sky (C) (bottom right). Taken from NOAA ESRL's MEI.v1 web page.

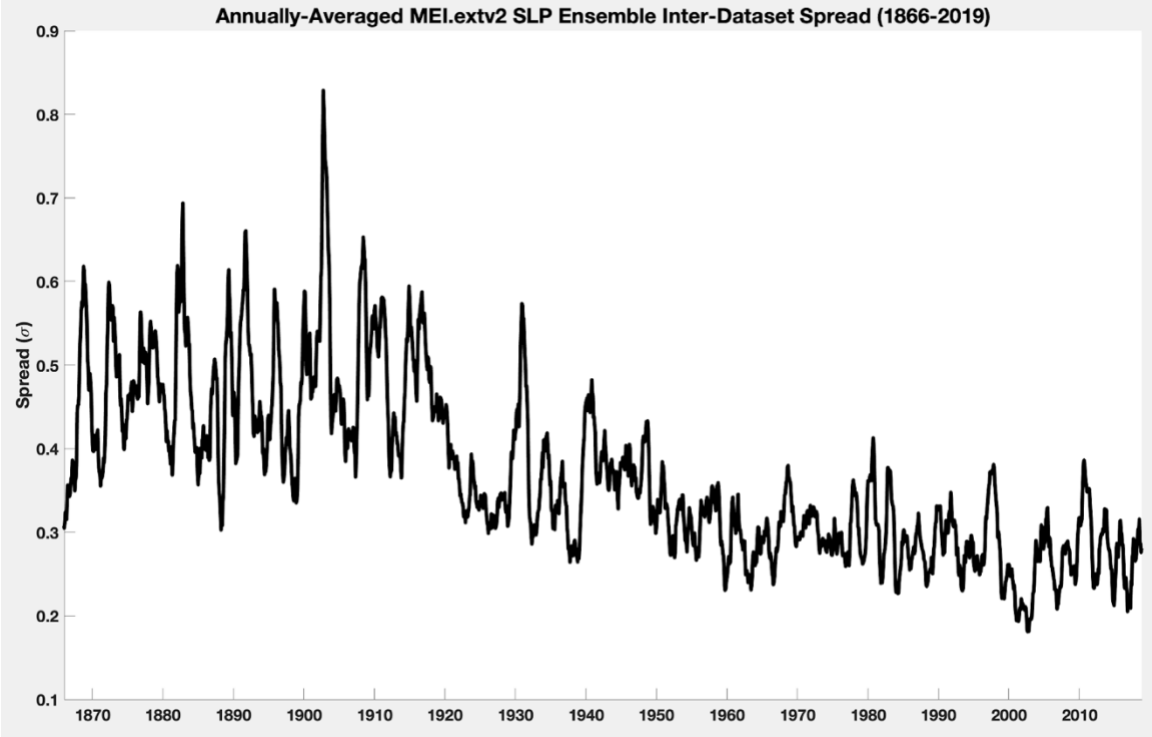

Figure 6. Annually-averaged MEI.extv2 SLP ensemble Inter-dataset spread (1866-2019).

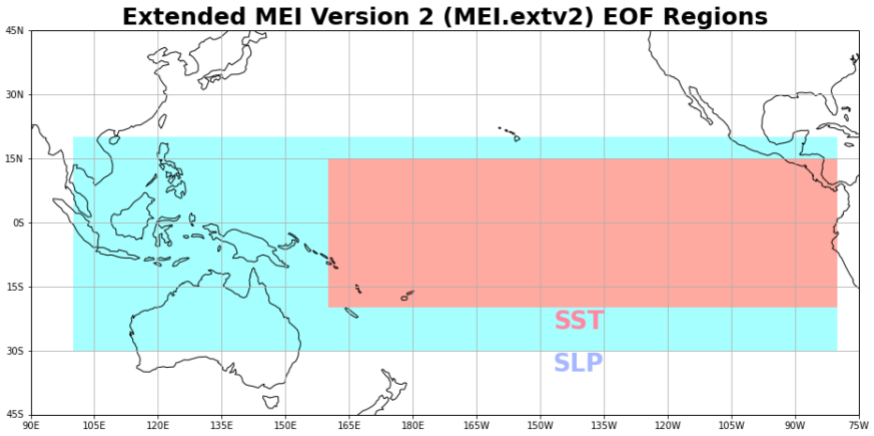

Figure 7. MEI.extv2 EOF regions SLP (light blue) [30S-20N, 100E-80W], SST (pink) [20S-15N,160E-80W]

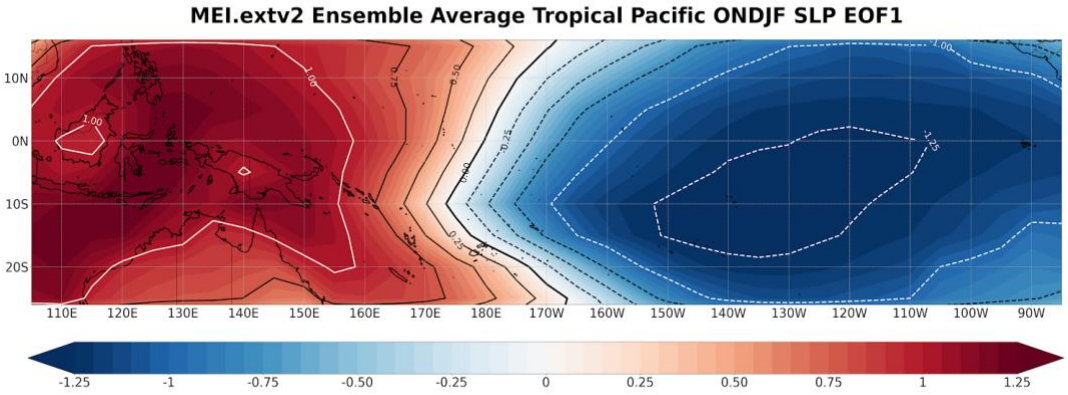

Figure 8. MEI.extv2 Ensemble Average of Oct-Feb SLP EOF1 from the 14 SLP datasets listed in table 2.

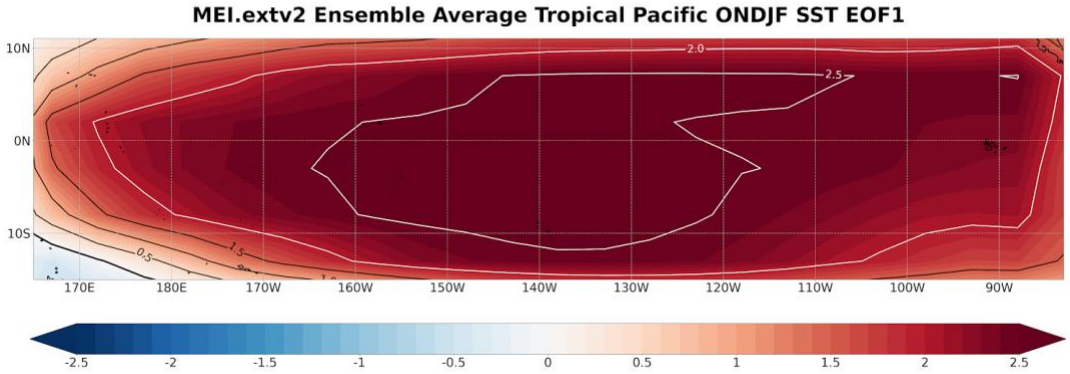

Figure 9. MEI.extv2 Ensemble Average of Oct-Feb SST EOF1 from the 15 SST datasets listed in table 2.

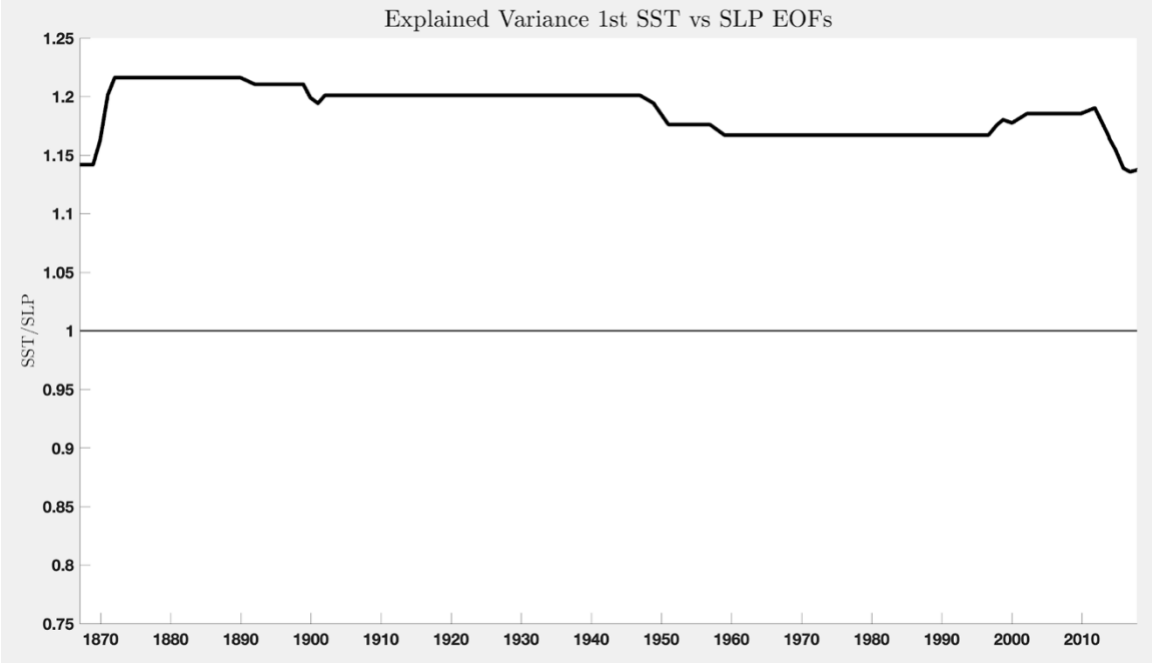

Figure 10. Bi-annually smoothed SST-SLP EOF Explained Variance Ratio (SST EOF 1 Explained Variance (%) /SLP EOF 1 Explained Variance (%)) 1867-2018.

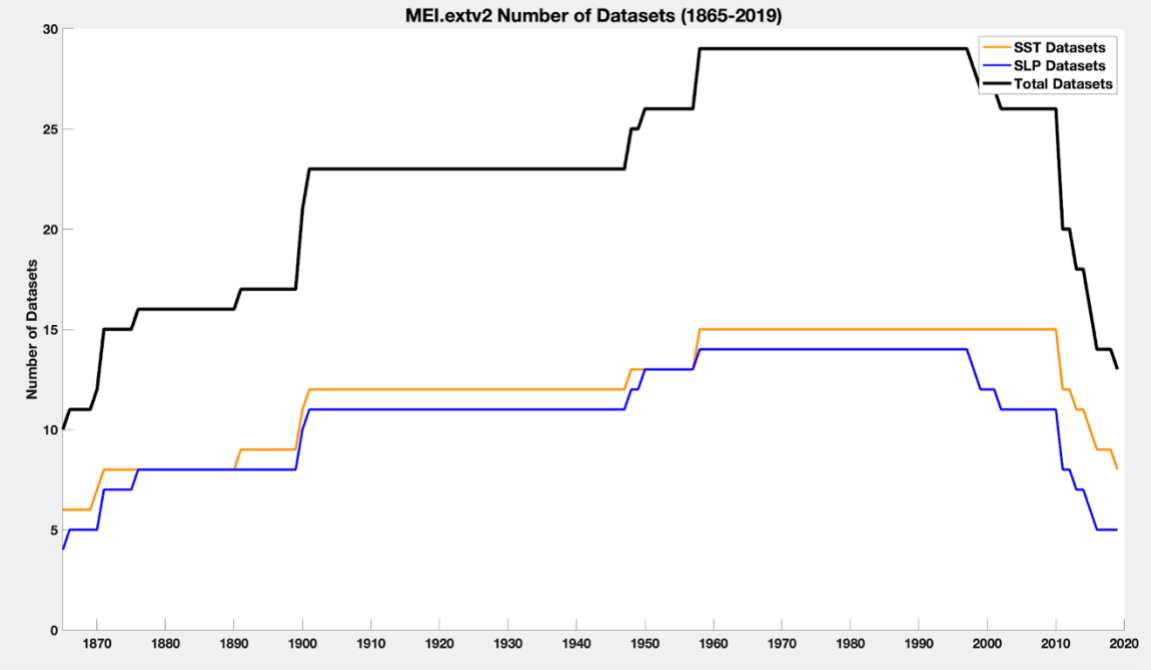

Figure 11. MEI.extv2 Number of datasets for SST (orange), SLP (blue), and total number of datasets (black) 1865-2019.

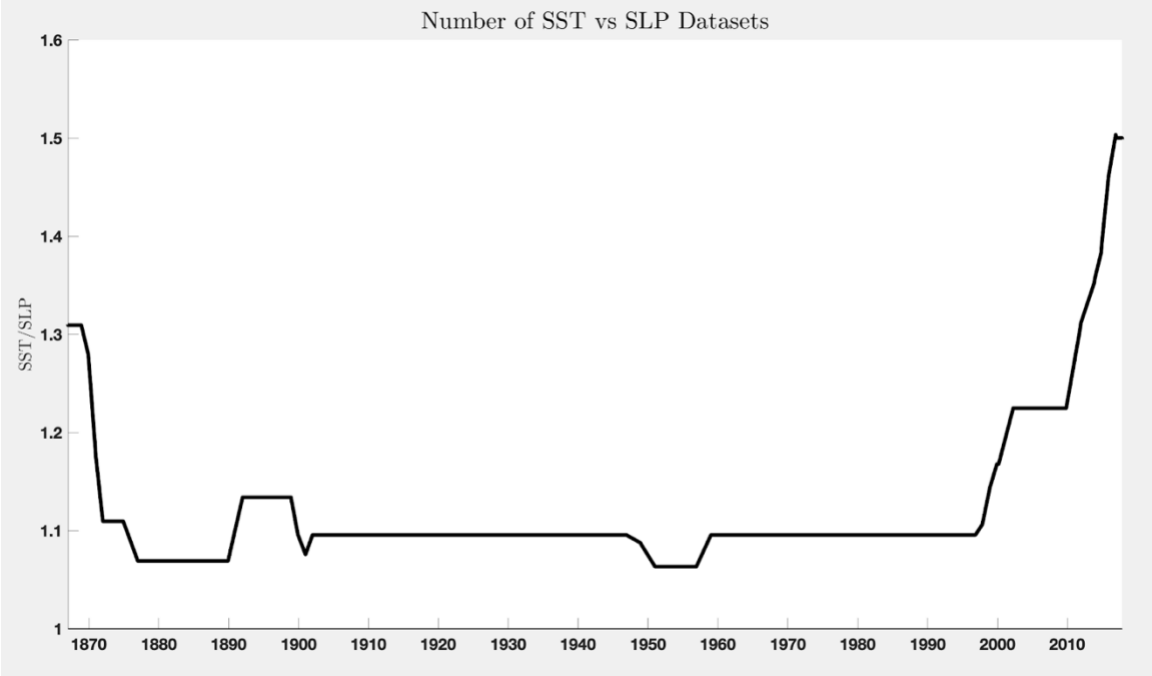

Figure 12. Bi-annually smoothed SST-SLP Dataset Ratio (Number of SST Datasets/ Number of SLP Datasets) (1867-2018)

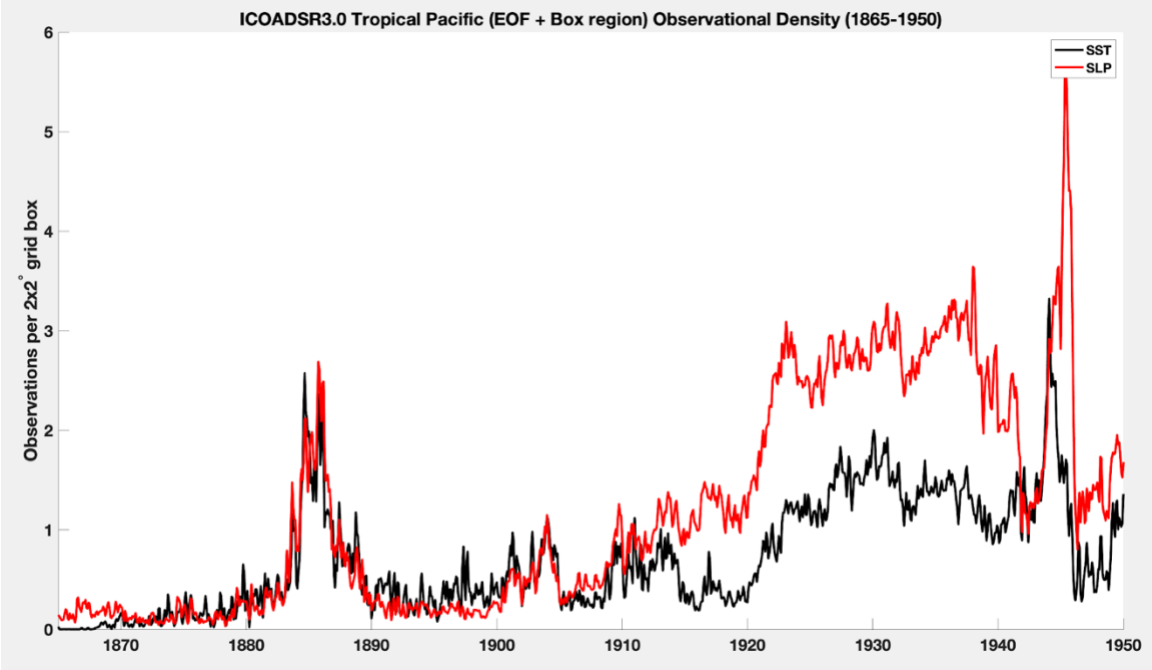

Figure 13. ICOADSR3.0 Tropical Pacific SST (black) and SLP (red) Number of Bi-Monthly Observations per 2x2° grid box averaged over their EOF (SST: [15S-10N,160E-80W], SLP: [30S-20N, 100E-80W]) and Box (SST: [5S-5N, 180W-80W], SLP: Tahiti [17.7S, 149.4W], Darwin [12.5S, 130.8E] (1865-1950).

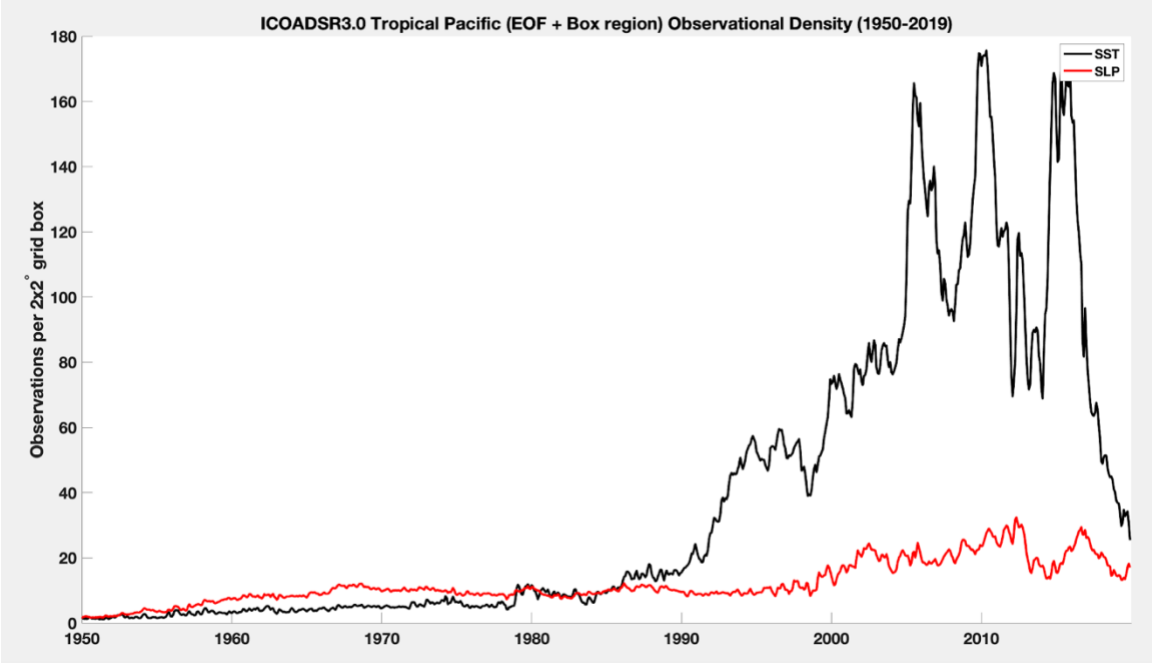

Figure 14. ICOADSR3.0 Tropical Pacific SST (black) and SLP (red) Number of Bi-Monthly Observations per 2x2° grid box averaged over their EOF (SST: [15S-10N,160E-80W], SLP: [30S-20N, 100E-80W]) and Box (SST: [5S-5N, 180W-80W], SLP: Tahiti [17.7S, 149.4W], Darwin [12.5S, 130.8E] (1950-2019).

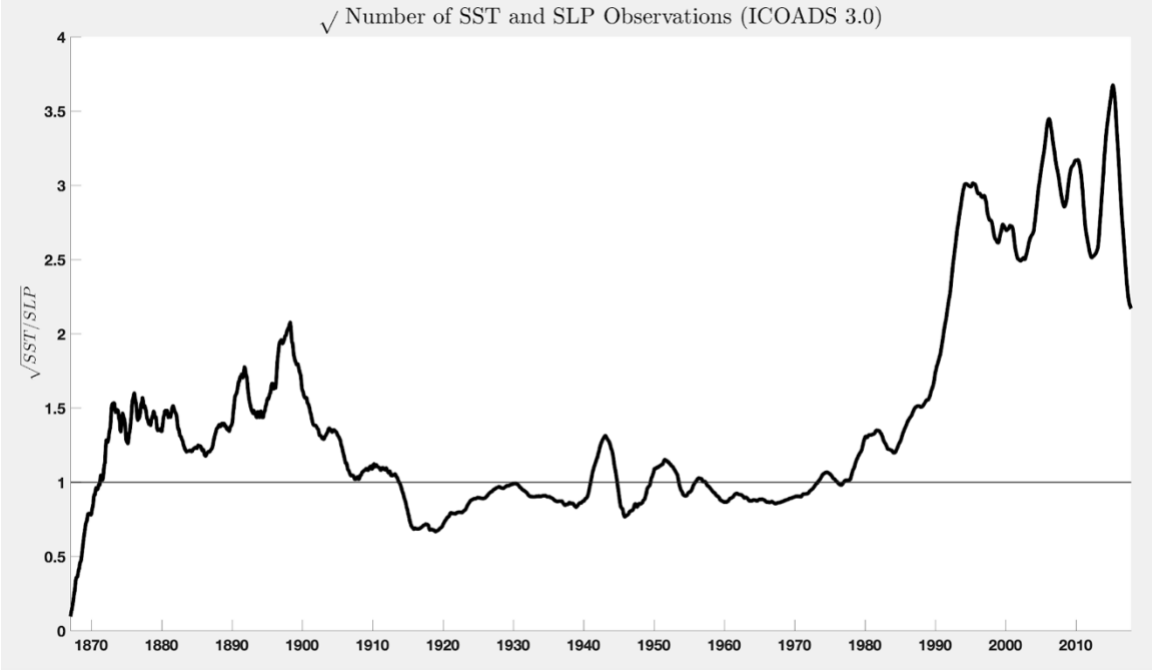

Figure 15. SST-SLP Observational density ratio (sqrt(SST obs density)/sqrt(SLP obs density) via ICOADS R3.0 1867-2018.

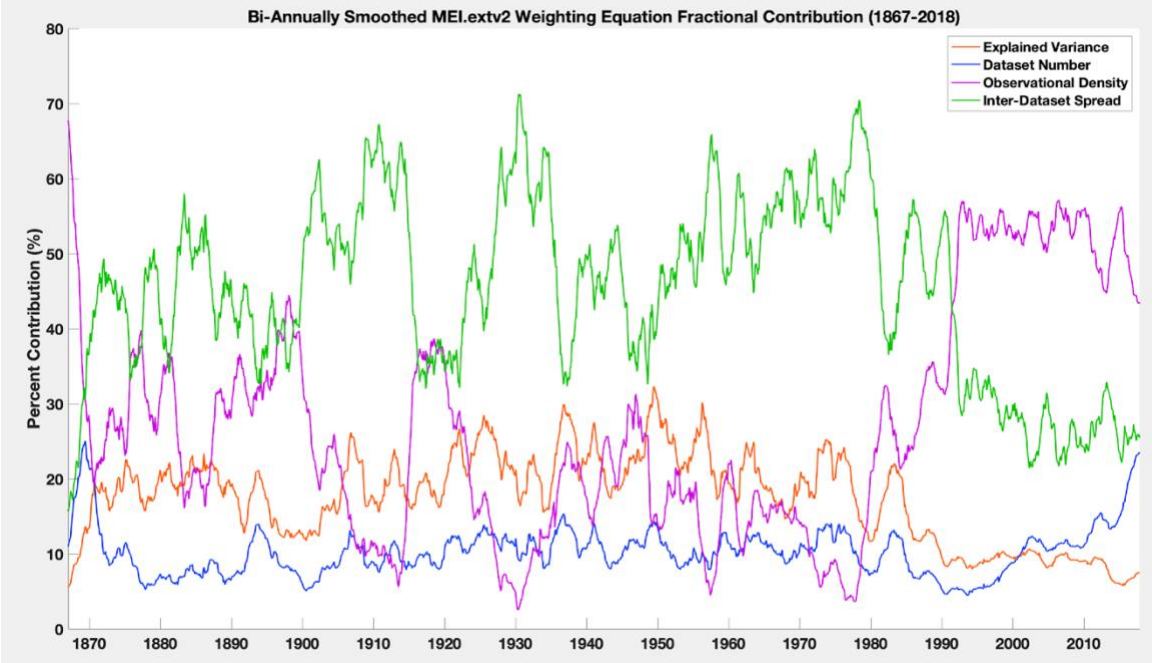

Figure 16. Bi-annually smoothed weighting equation fractional contribution (1867-2018). Explained variance (red), dataset number (blue), observational density (magenta), inter-dataset spread (green).

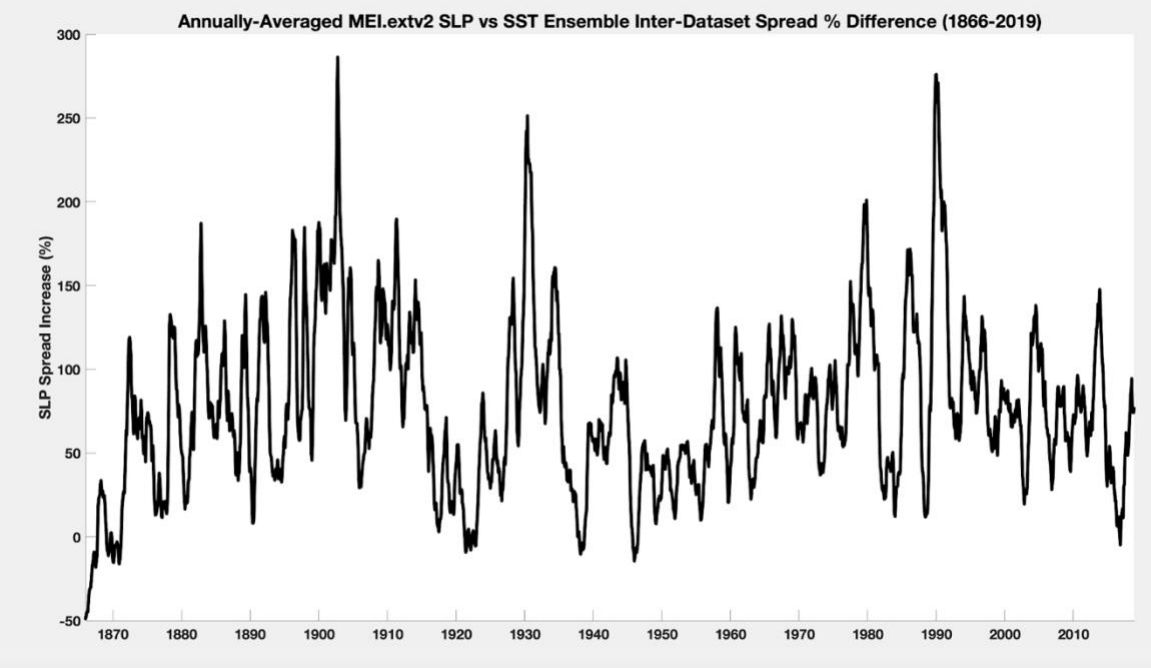

Figure 17. Annually-averaged SLP vs SST ensemble inter-dataset spread percent difference (positive values = SLP higher).

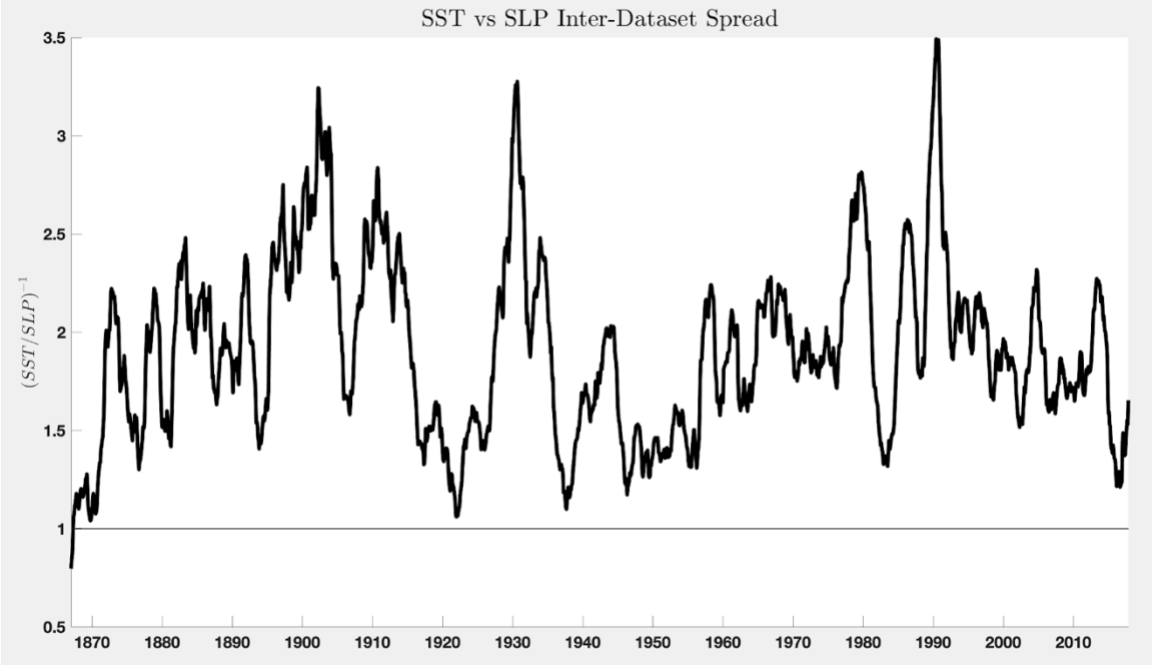

Figure 18. Bi-annually averaged SST - SLP Inter-Dataset Spread Ratio (SLP spread ($\boldsymbol{\sigma}$)/SST spread ($\boldsymbol{\sigma}$)) 1867-2018.

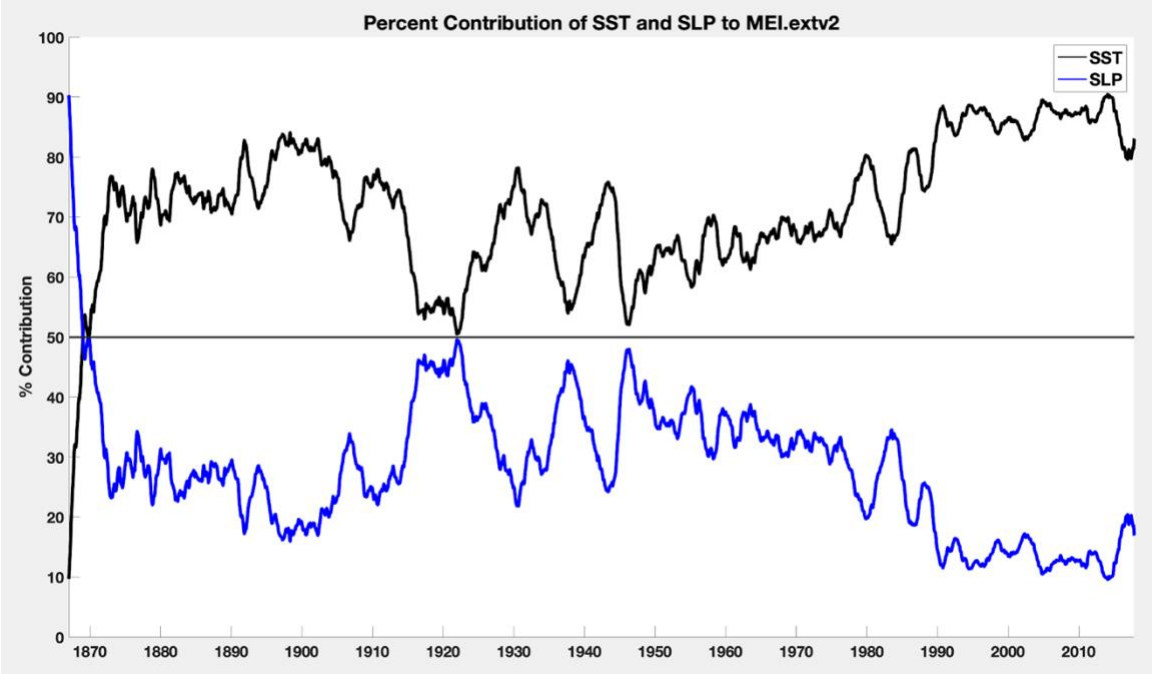

Figure 19. Bi-annually smoothed percent contribution of SST and SLP to the MEI.extv2 (1867-2018).

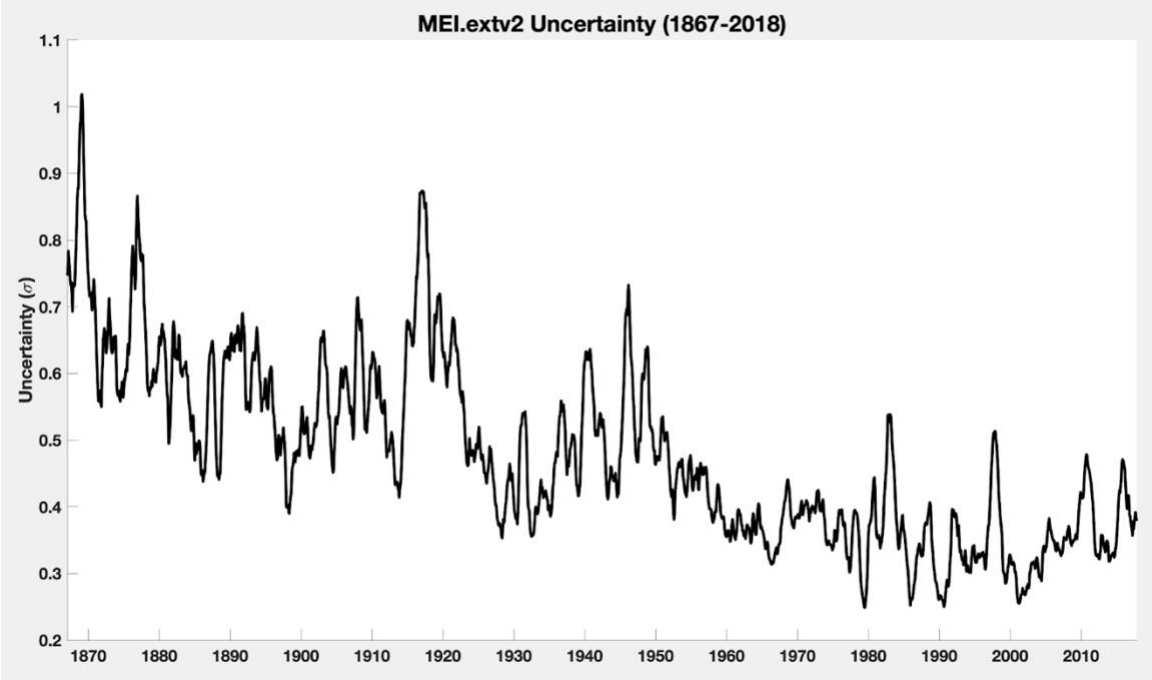

Figure 20. Bi-annually smoothed MEI.extv2 uncertainty ($\boldsymbol{\sigma}$) derived from equation 3 (1867-2018)

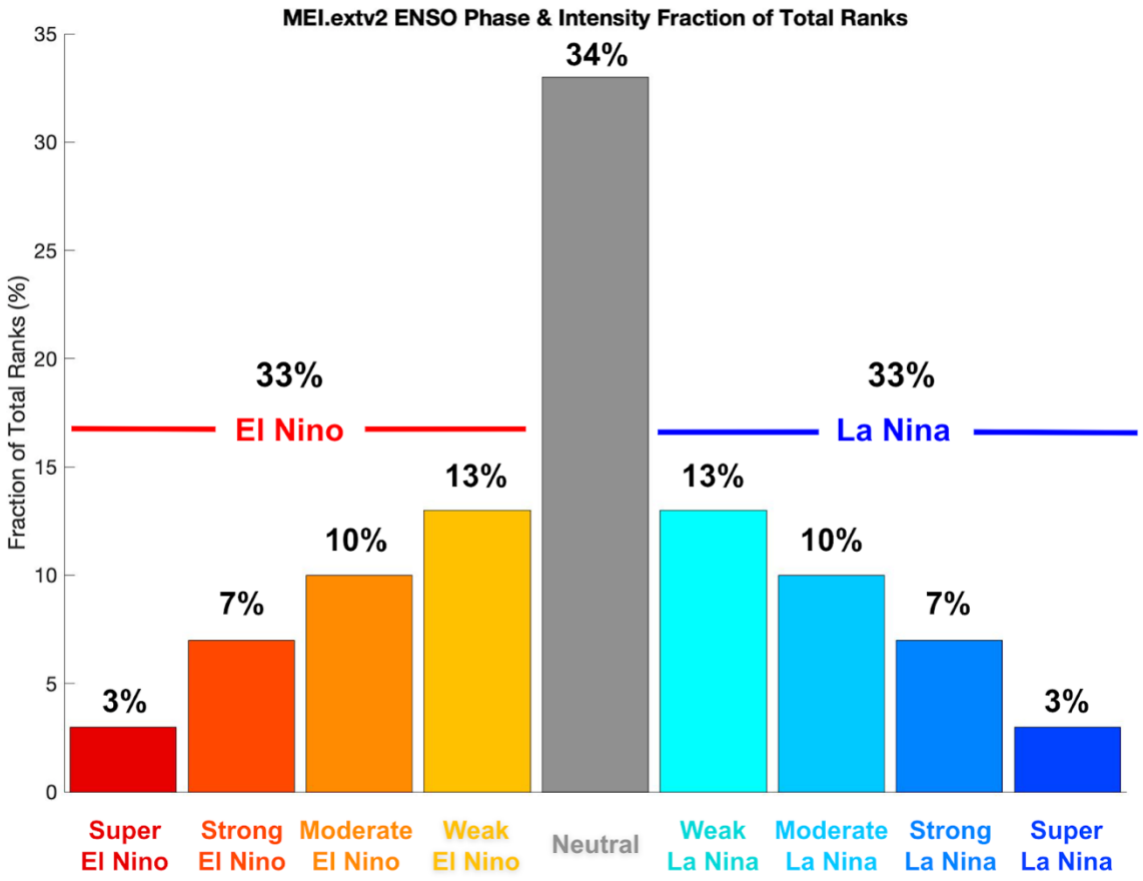

Figure 21. MEI.extv2 ENSO phase and intensity + fraction of total ranks. El Nino (left, warm colors), Neutral ENSO (middle, grey), and La Nina (right, cool colors).

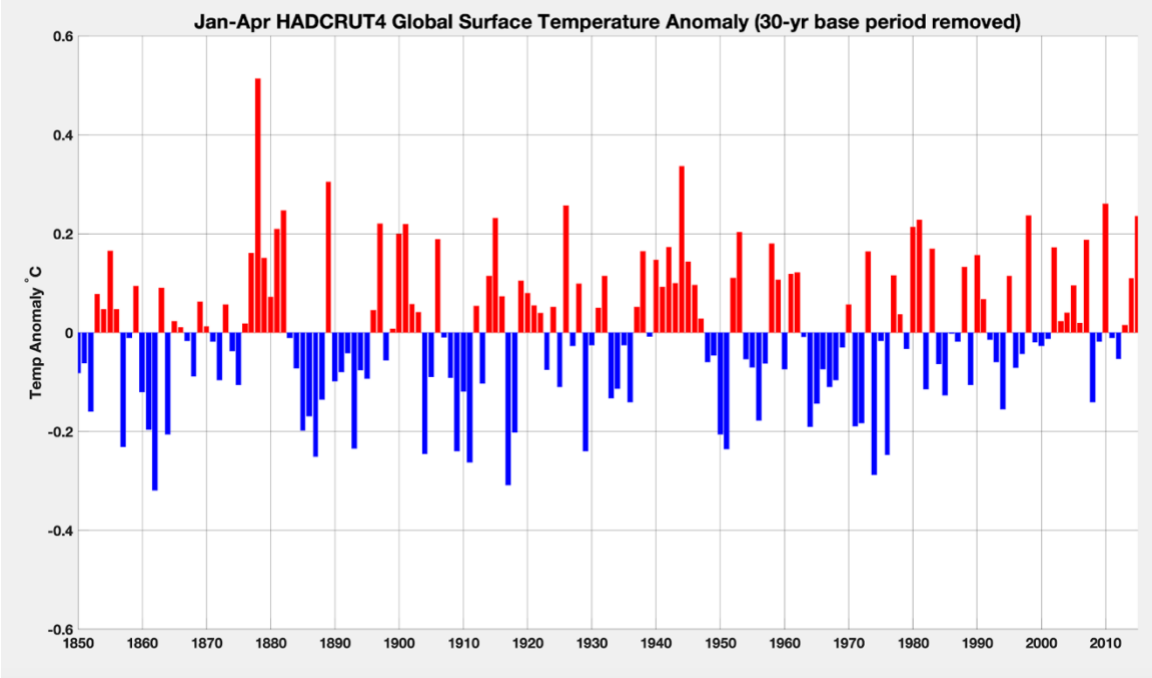

Figure 22. Jan-April averaged HADCRUT4 global surface temperature anomaly average, with a 30-year sliding base period removed (motivated by Aceituno et al, 2009).

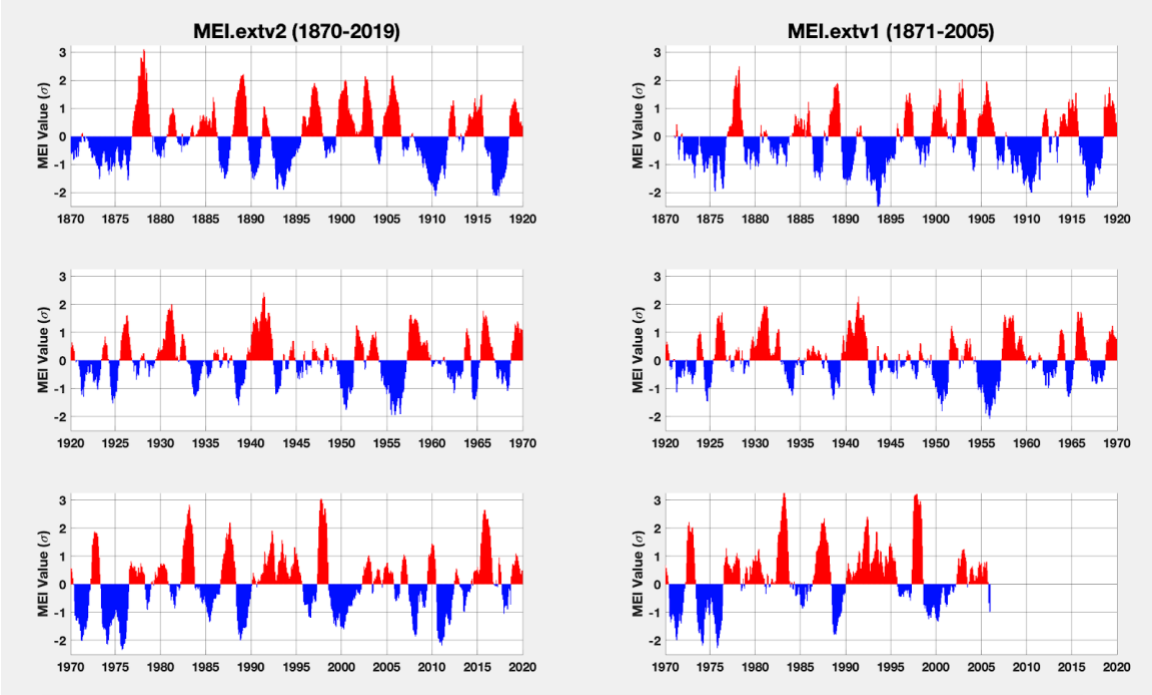

Figure 23. Time series of the MEI.extv2 (left) and MEI.extv1 (right). Red/warm (Blue/cool) colors are associated with El Nino (La Nina) conditions. The overall structure of the plot was motivated by and follows similar conventions to Wolter and Timlin (2011).

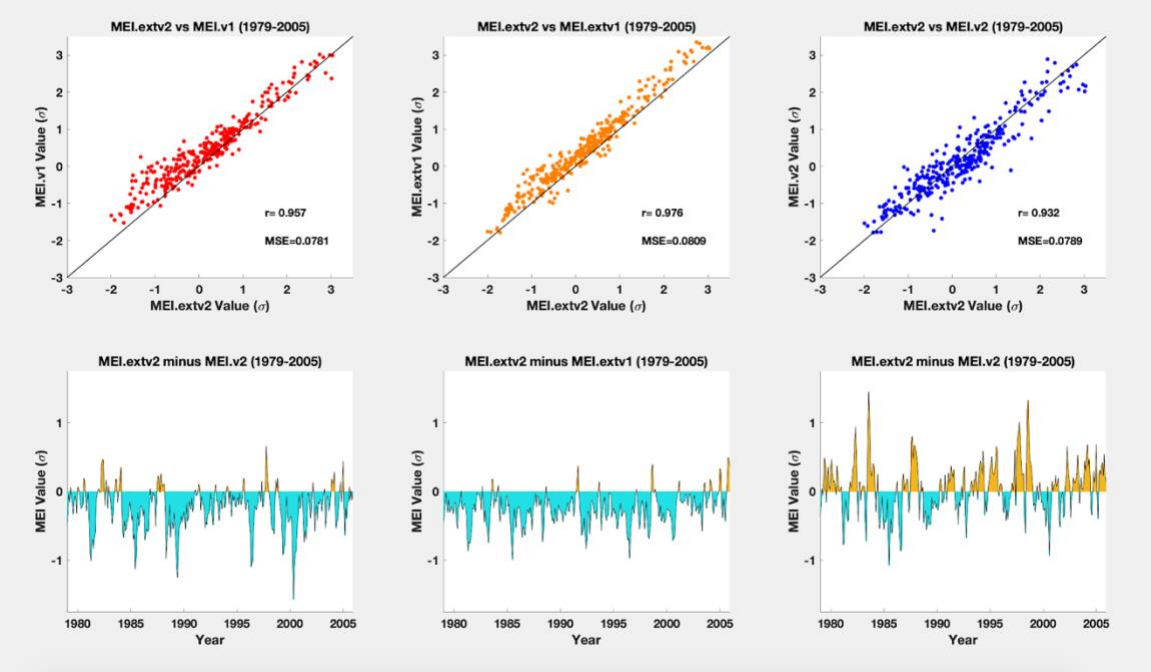

Figure 24. MEI.extv2 scatter (top) and time series difference (bottom) plot with MEI.v1 (left), MEI.ext (middle), and MEI.v2 (right)

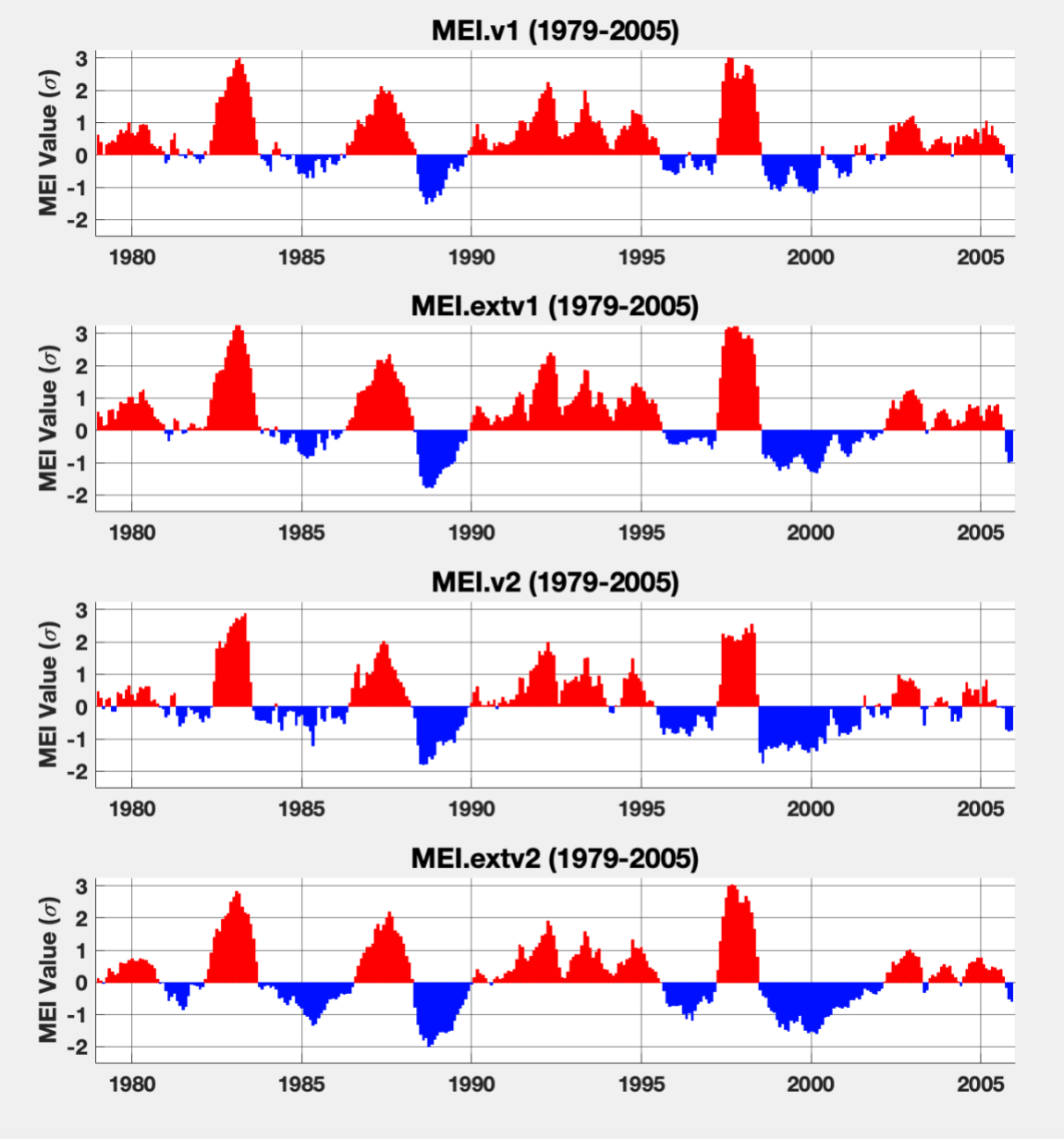

Figure 25. MEI anomaly time series (1979-2005): MEI.v1 (top), MEI.ext (second from top), MEI.v2 (second from bottom), and MEI.extv2 (bottom)

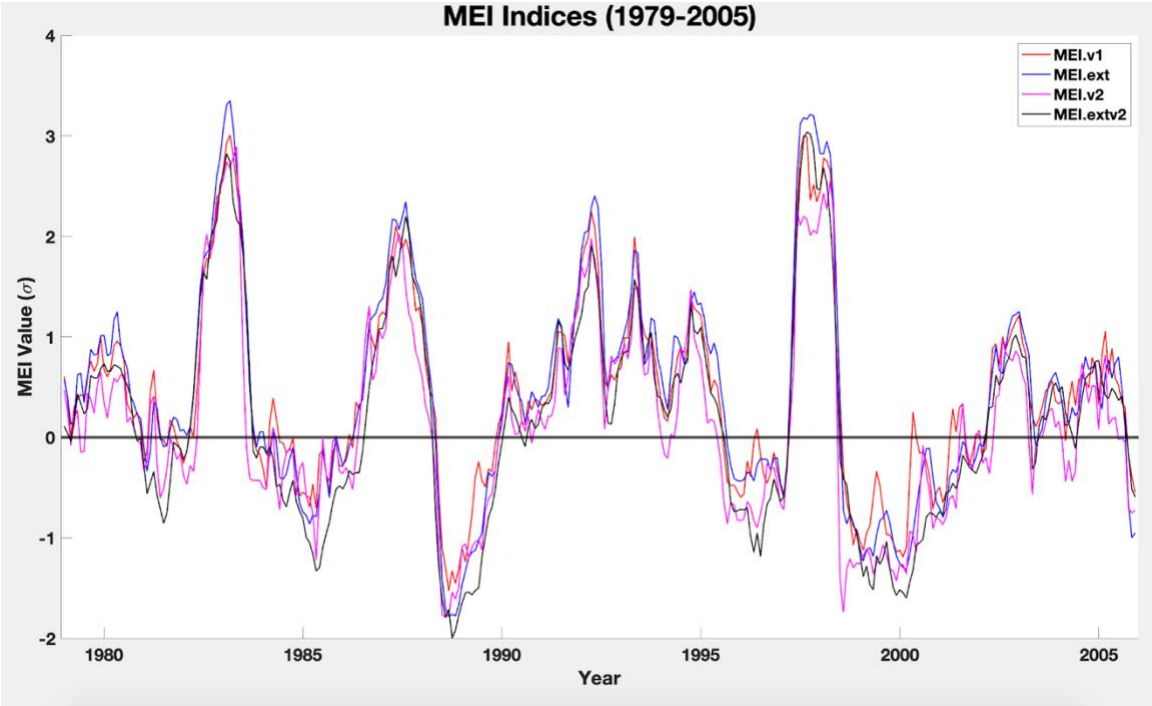

Figure 26. MEI indices time series (1979-2005), MEI.v1 (red), MEI.ext (blue), MEI.v2 (magenta), and MEI.extv2 (black)

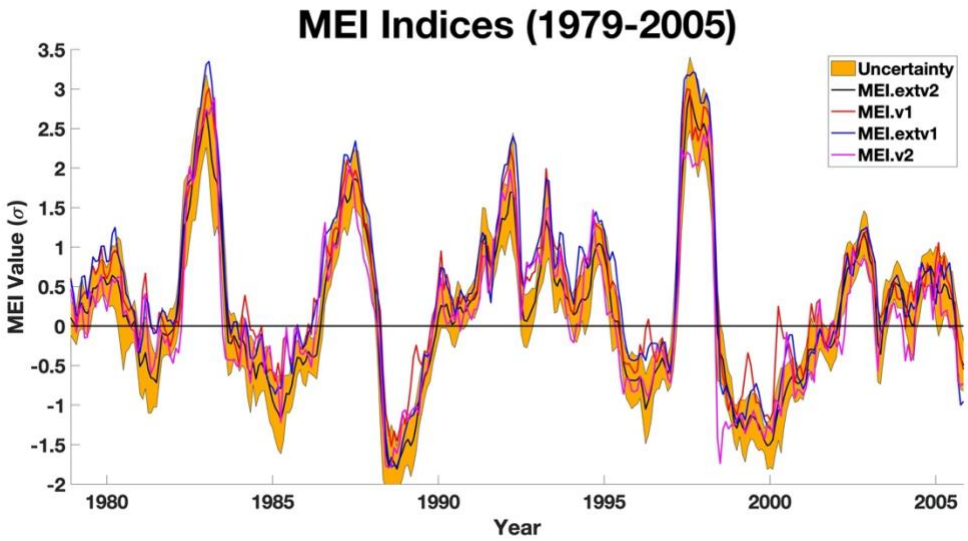

Figure 27. MEI indices time series and uncertainty (1979-2005), uncertainty (orange shading), MEI.v1 (red), MEI.ext (blue), MEI.v2 (magenta), and MEI.extv2 (black)

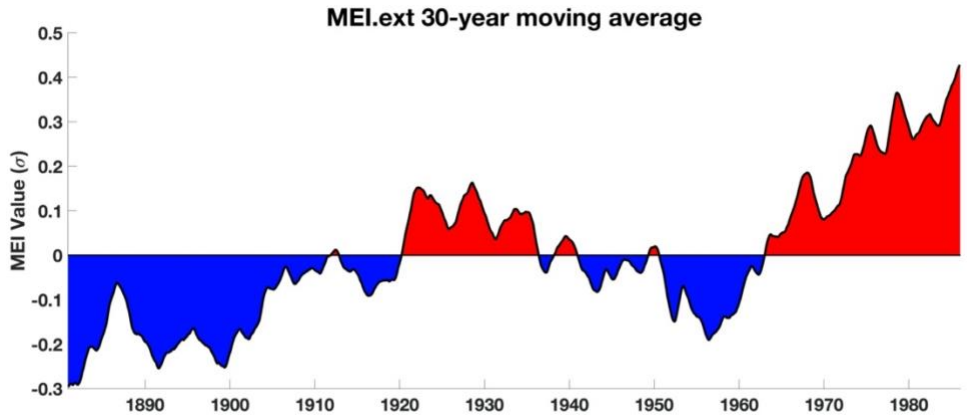

Figure 28. MEI.ext 30-year moving average values (red = positive/El Nino bias, blue = negative/La Nina bias).

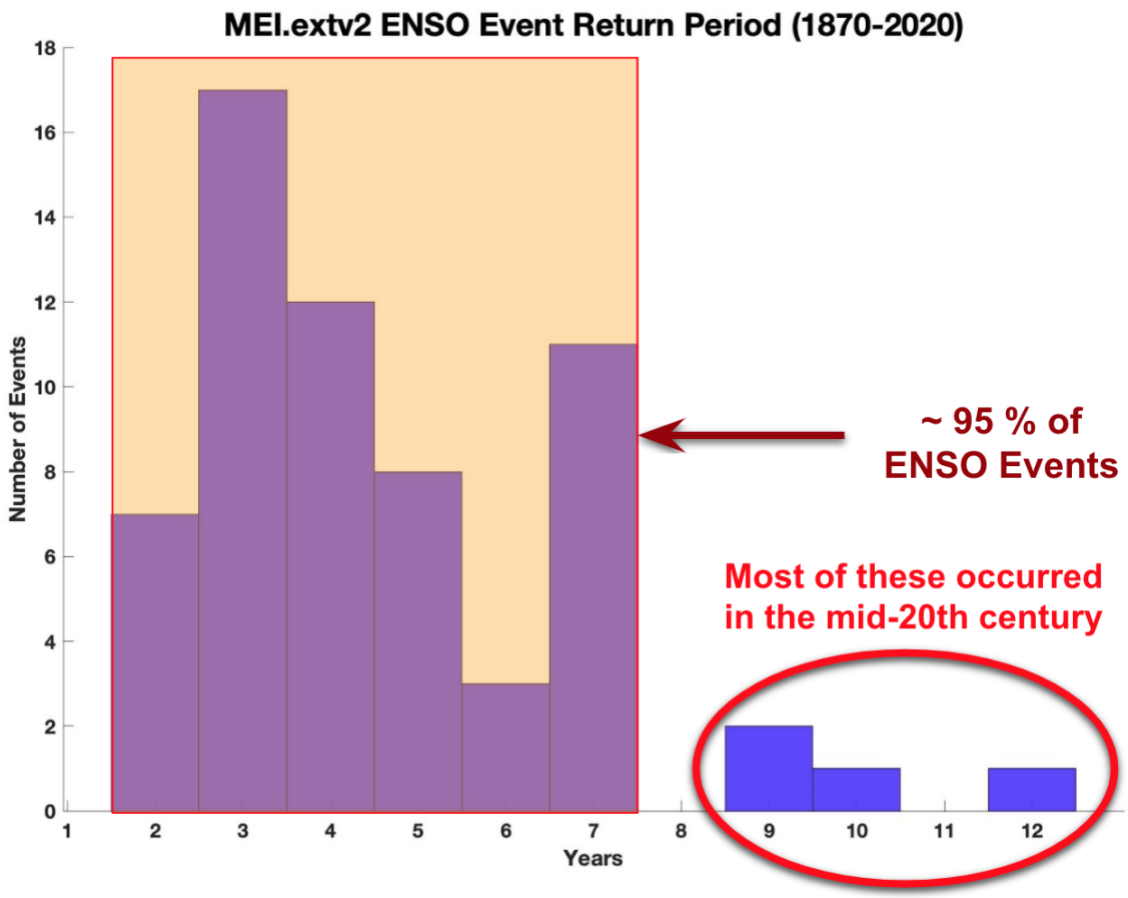

Figure 29. MEI.extv2 ENSO (El Nino or La Nina) event return period histogram.

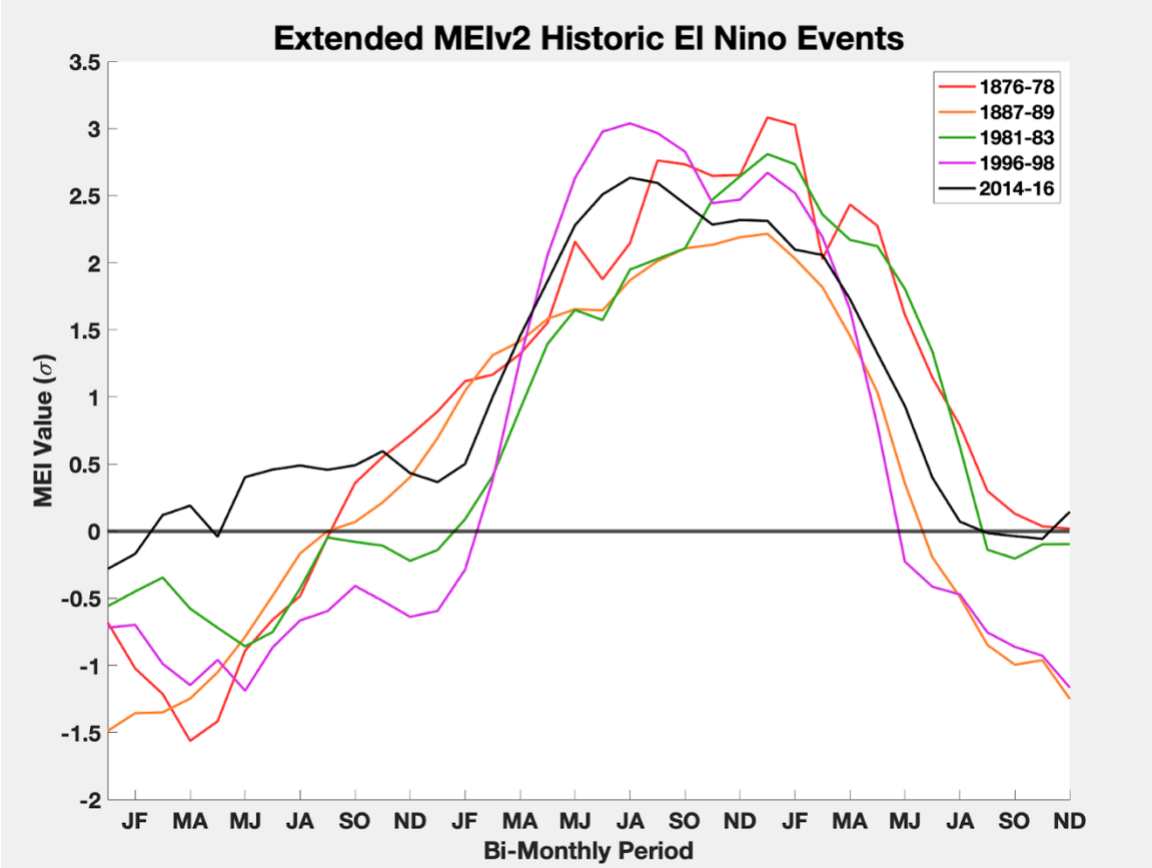

Figure 30. MEI.extv2 “historic” (top 5) El Nino events (as measured by the ensemble median)

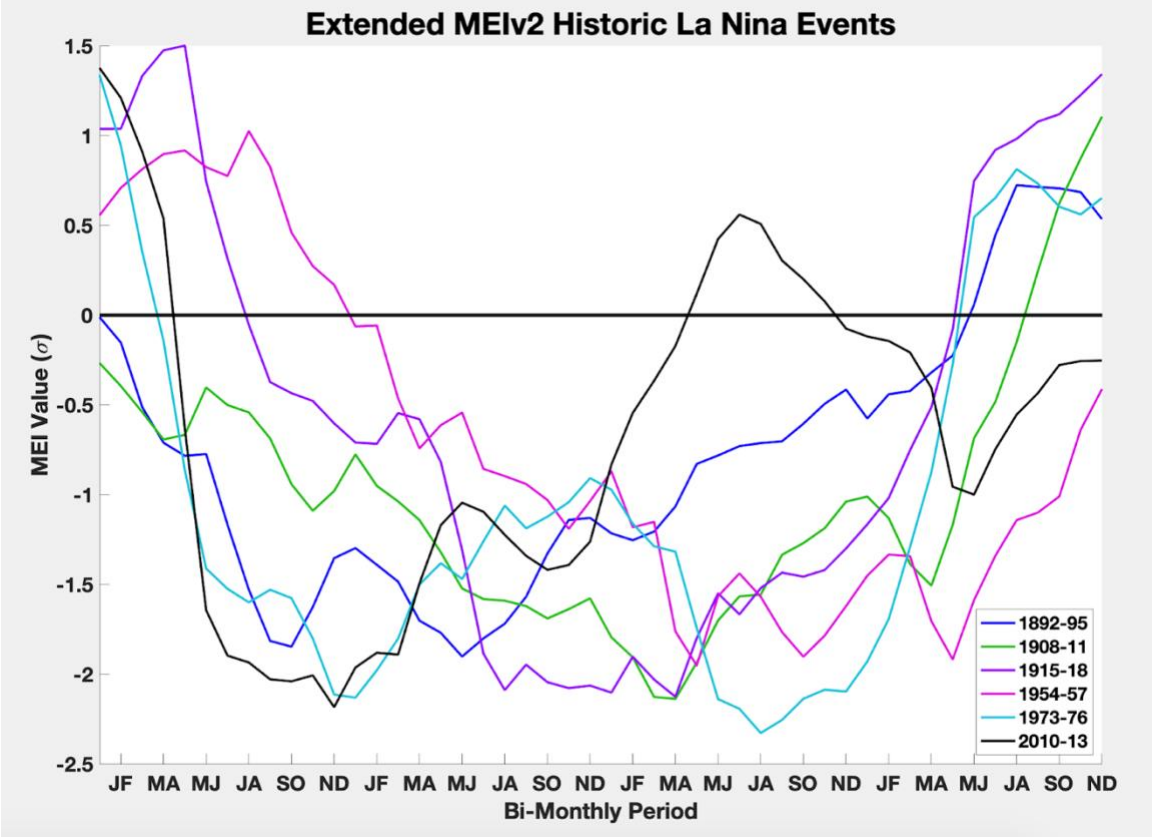

Figure 31. MEI.extv2 “historic” La Nina events (as measured by the ensemble median)

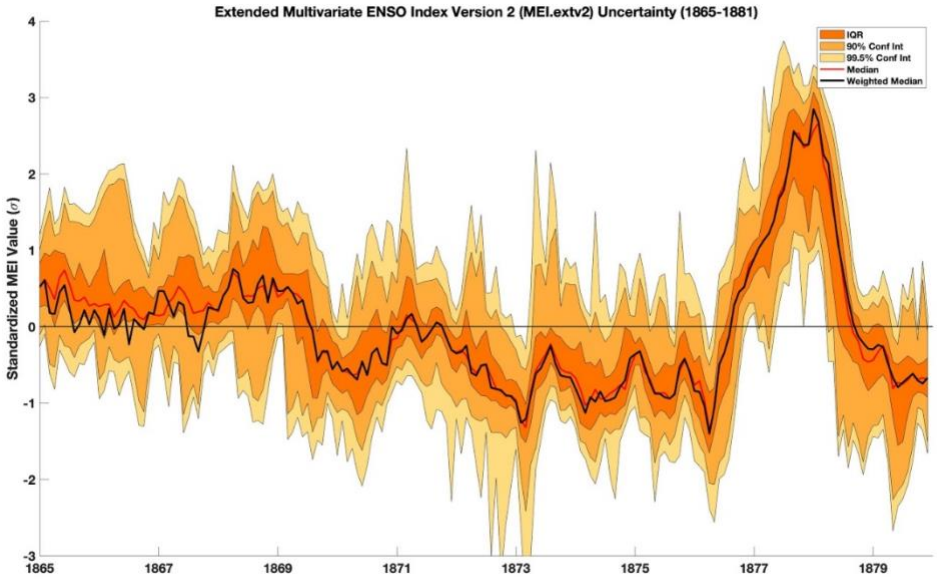

Figure 32. MEI.extv2 uncertainty time series (1865-1880), interquartile range (IQR) (dark orange shading), 90% confidence interval (orange shading), 99.5% confidence interval (yellow shading), unweighted, unadjusted median (red line), weighted, adjusted ensemble median (black line).

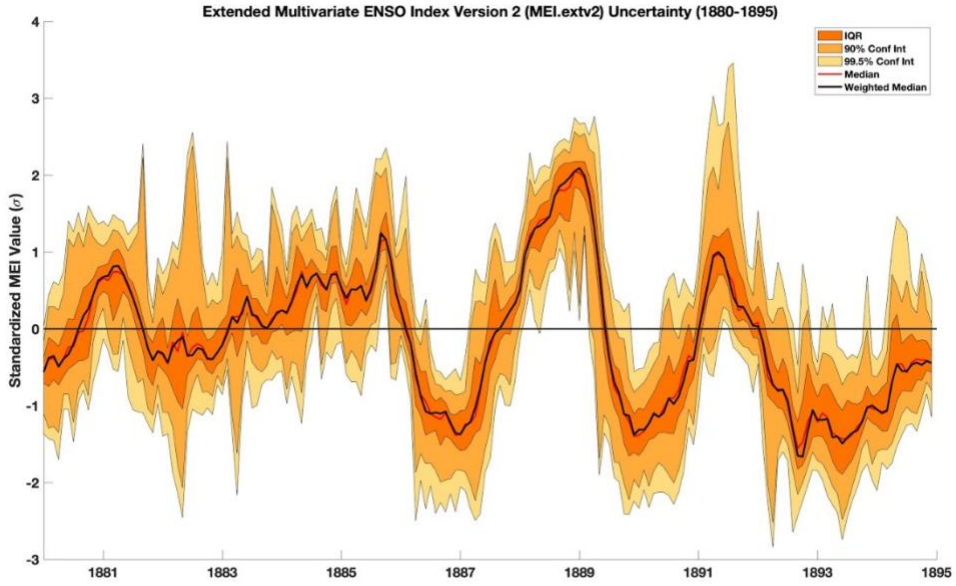

Figure 33. MEI.extv2 uncertainty time series (1880-1895), interquartile range (IQR) (dark orange shading), 90% confidence interval (orange shading), 99.5% confidence interval (yellow shading), unweighted, unadjusted median (red line), weighted, adjusted ensemble median (black line).

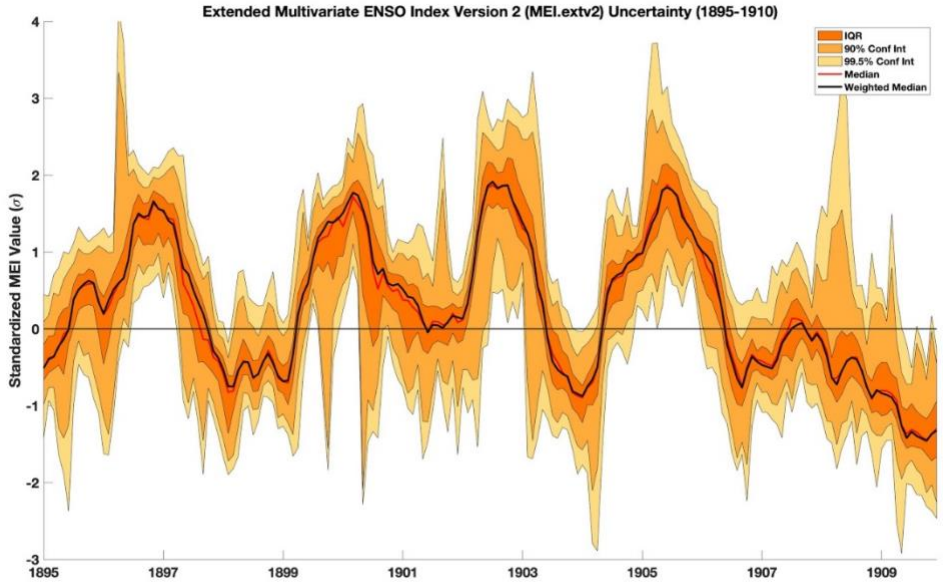

Figure 34. MEI.extv2 uncertainty time series (1895-1910), interquartile range (IQR) (dark orange shading), 90% confidence interval (orange shading), 99.5% confidence interval (yellow shading), unweighted, unadjusted median (red line), weighted, adjusted ensemble median (black line).

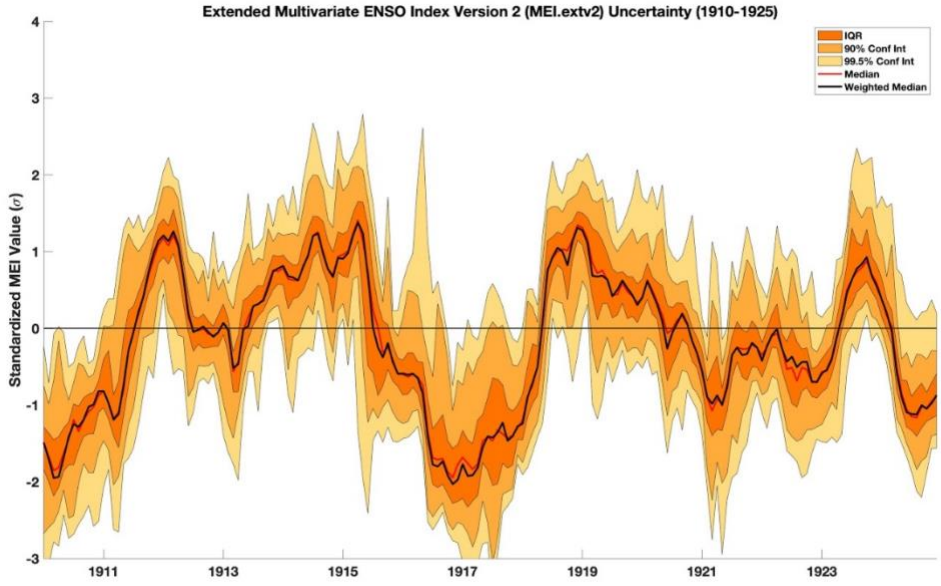

Figure 35. MEI.extv2 uncertainty time series (1910-1925), interquartile range (IQR) (dark orange shading), 90% confidence interval (orange shading), 99.5% confidence interval (yellow shading), unweighted, unadjusted median (red line), weighted, adjusted ensemble median (black line).

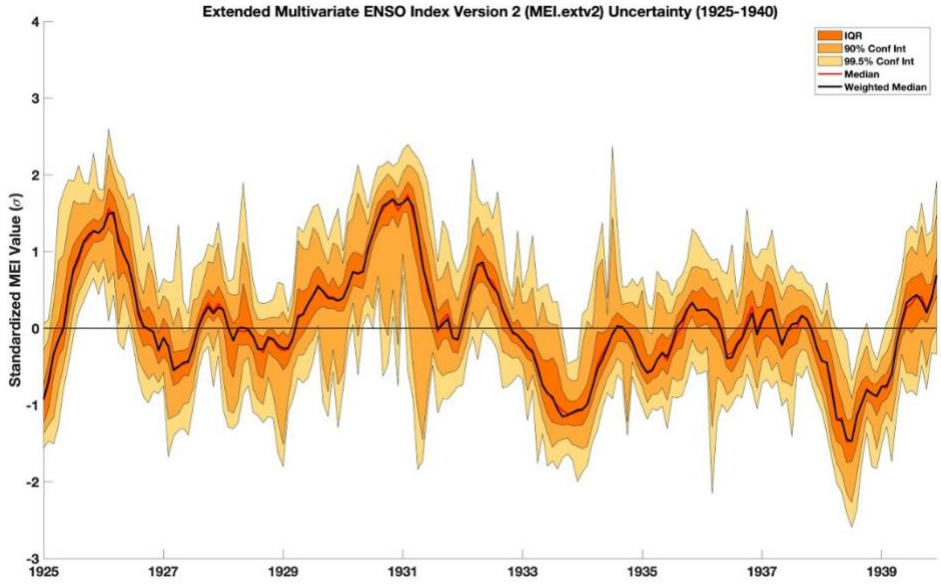

Figure 36. MEI.extv2 uncertainty time series (1925-1940), interquartile range (IQR) (dark orange shading), 90% confidence interval (orange shading), 99.5% confidence interval (yellow shading), unweighted, unadjusted median (red line), weighted, adjusted ensemble median (black line).

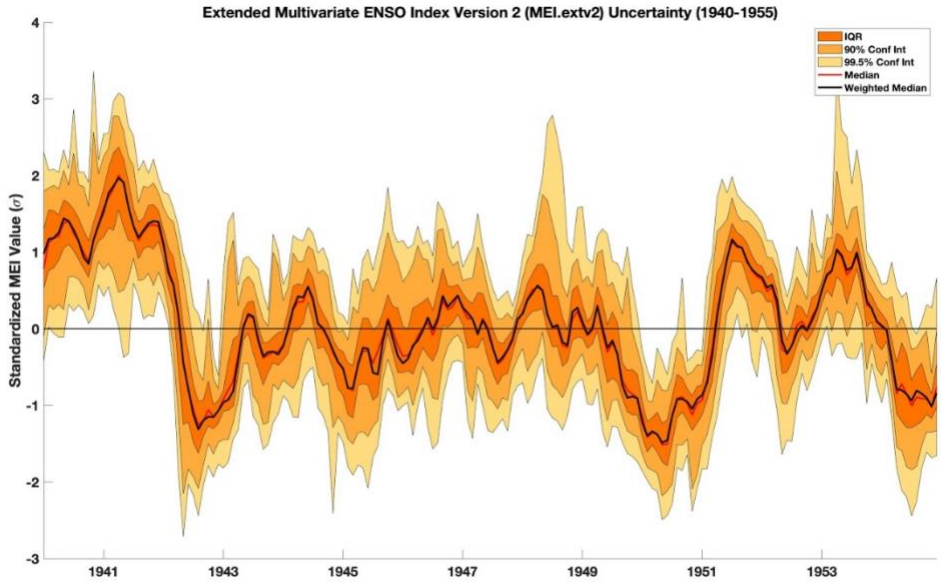

Figure 37. MEI.extv2 uncertainty time series (1940-1955), interquartile range (IQR) (dark orange shading), 90% confidence interval (orange shading), 99.5% confidence interval (yellow shading), unweighted, unadjusted median (red line), weighted, adjusted ensemble median (black line).

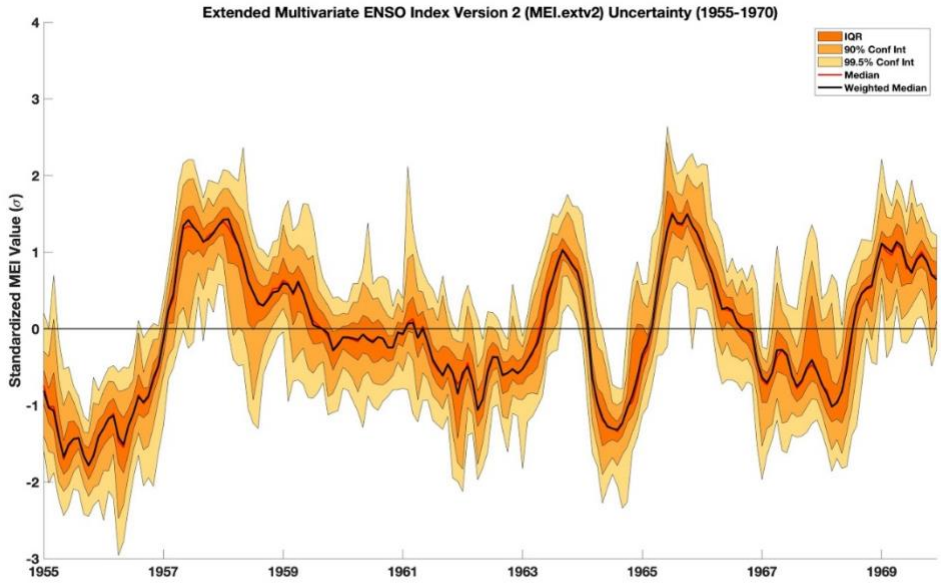

Figure 38. MEI.extv2 uncertainty time series (1955-1970), interquartile range (IQR) (dark orange shading), 90% confidence interval (orange shading), 99.5% confidence interval (yellow shading), unweighted, unadjusted median (red line), weighted, adjusted ensemble median (black line).

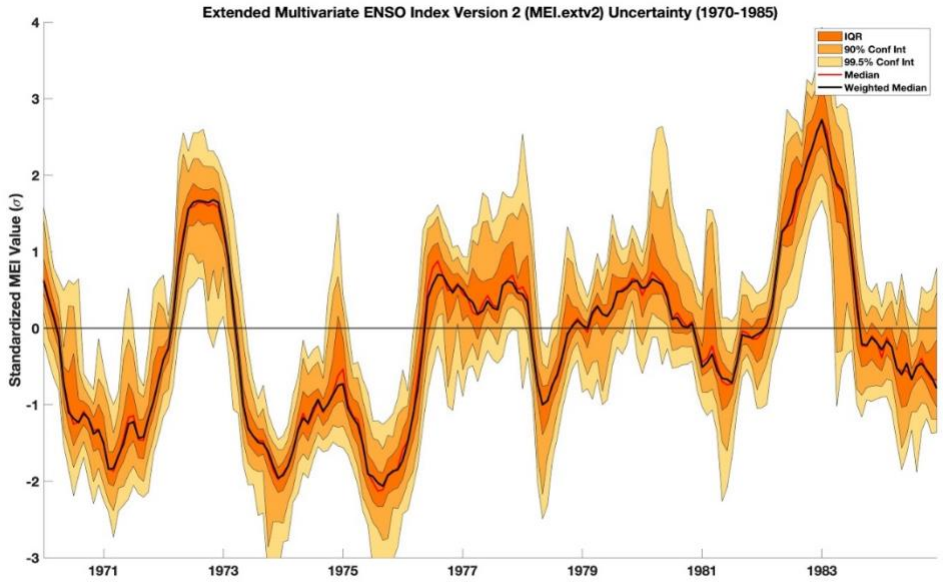

Figure 39. MEI.extv2 uncertainty time series (1970-1985), interquartile range (IQR) (dark orange shading), 90% confidence interval (orange shading), 99.5% confidence interval (yellow shading), unweighted, unadjusted median (red line), weighted, adjusted ensemble median (black line).

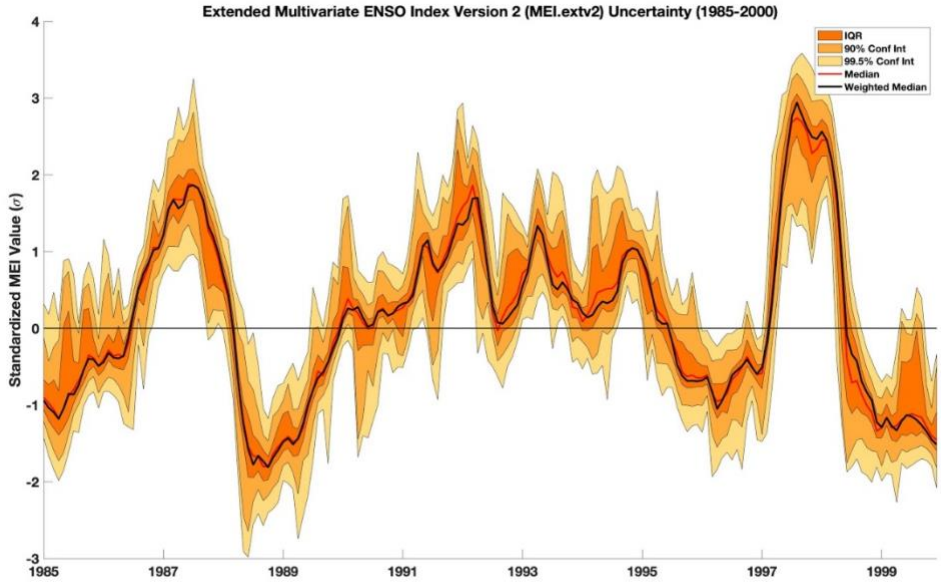

Figure 40. MEI.extv2 uncertainty time series (1985-2000), interquartile range (IQR) (dark orange shading), 90% confidence interval (orange shading), 99.5% confidence interval (yellow shading), unweighted, unadjusted median (red line), weighted, adjusted ensemble median (black line).

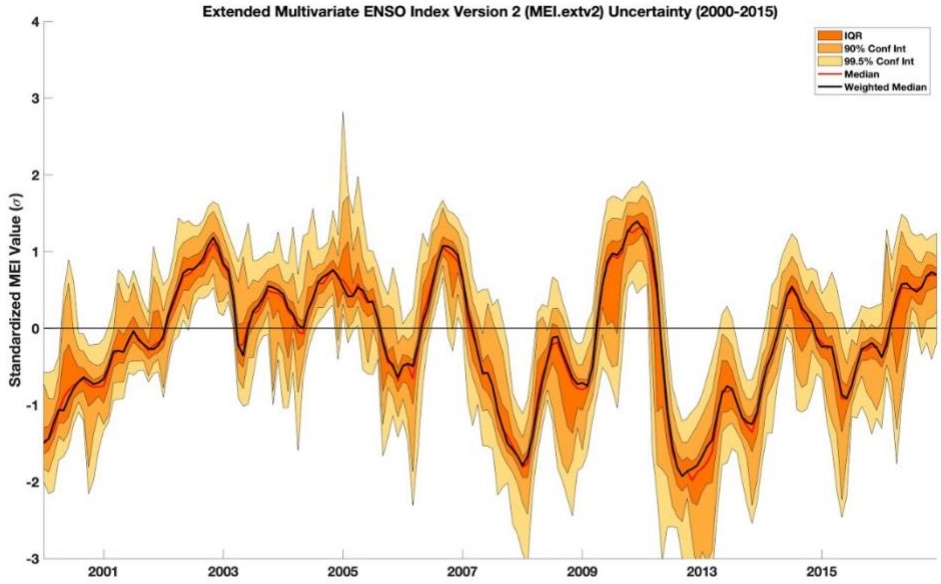

Figure 41. MEI.extv2 uncertainty time series (2000-2015), interquartile range (IQR) (dark orange shading), 90% confidence interval (orange shading), 99.5% confidence interval (yellow shading), unweighted, unadjusted median (red line), weighted, adjusted ensemble median (black line).

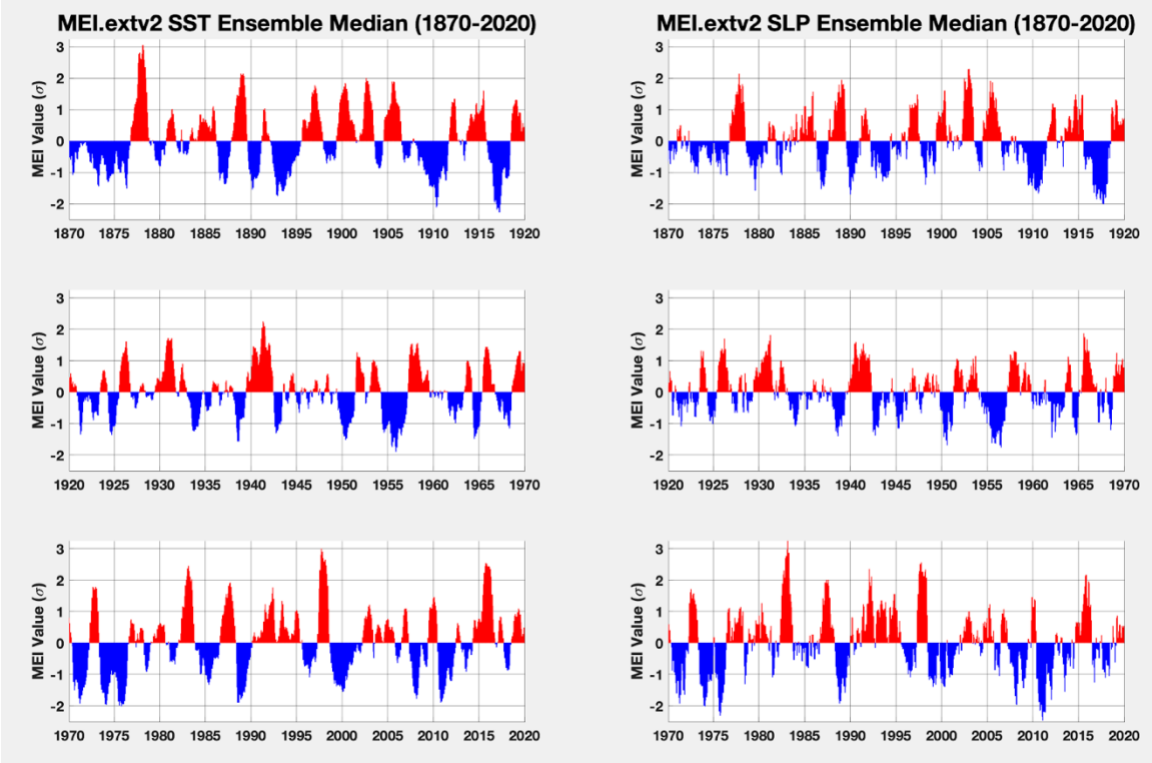

Figure 42. MEI.extv2 SST ensemble median anomaly time series (left), SLP ensemble median anomaly time series (right).

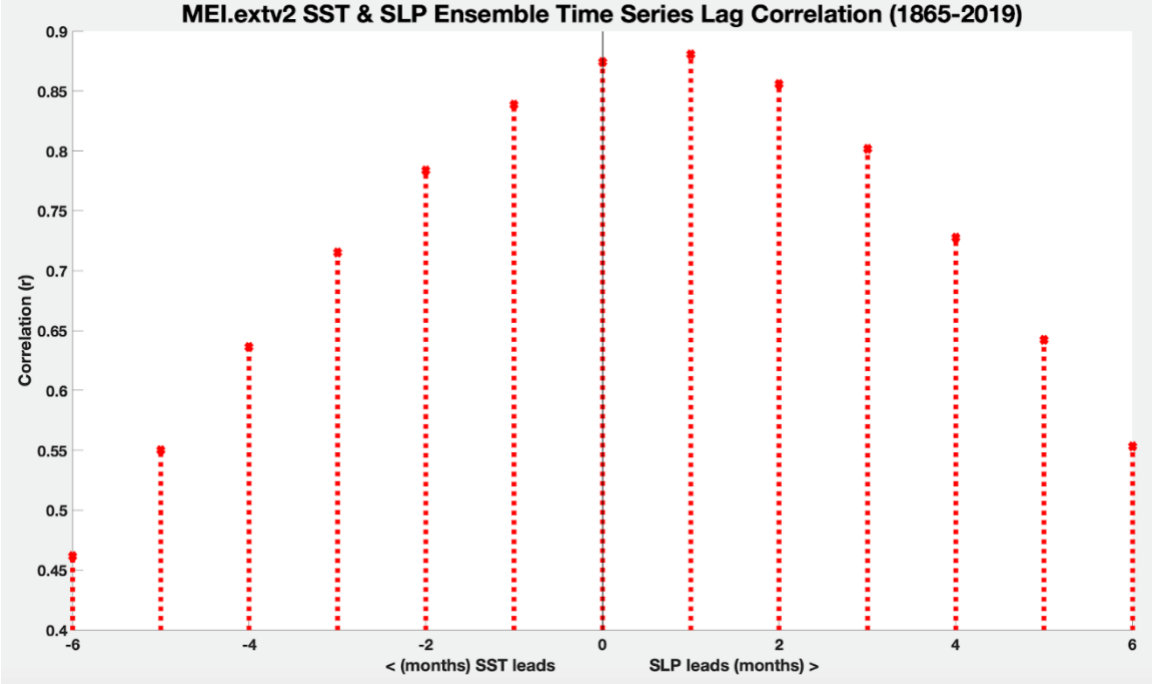

Figure 43. MEI.extv2 SST and SLP ensemble time series lag correlation (in months) (1865-2019).

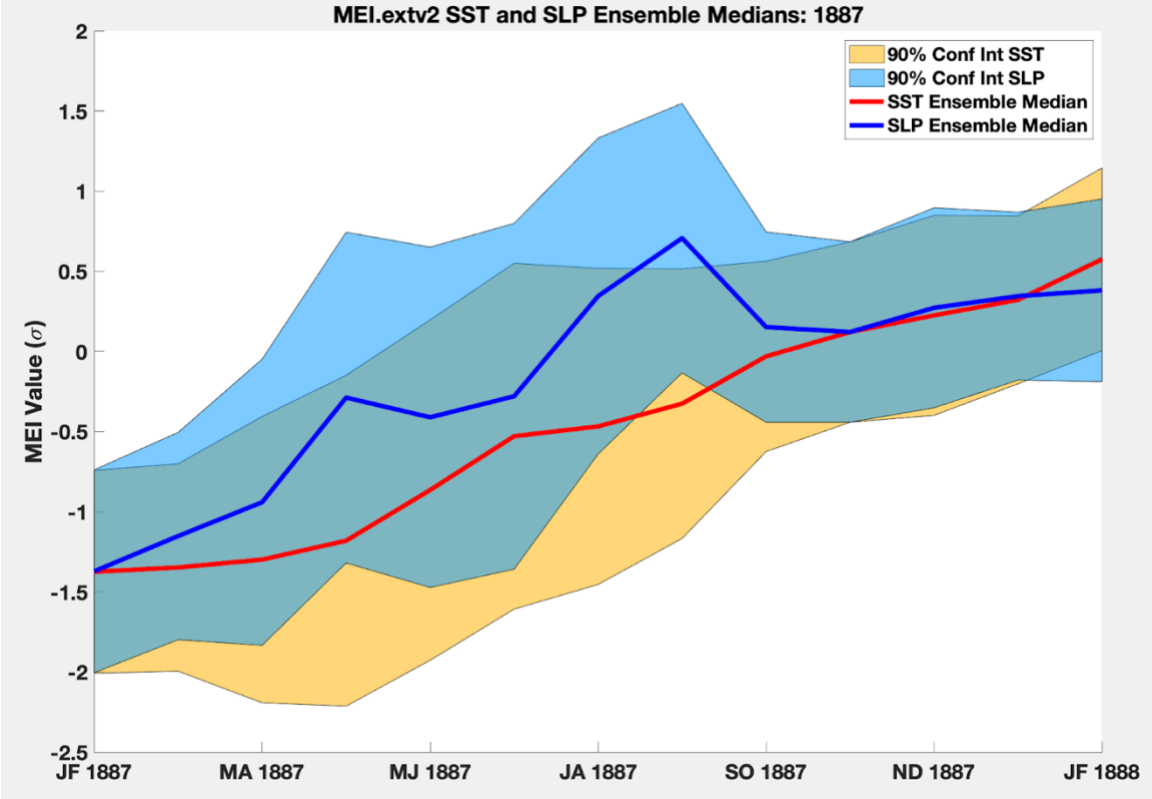

Figure 44. MEI.extv2 SST (red line) and SLP ensemble (blue line) medians with 90% confidence interval shading for SST (light orange) and SLP (light blue).

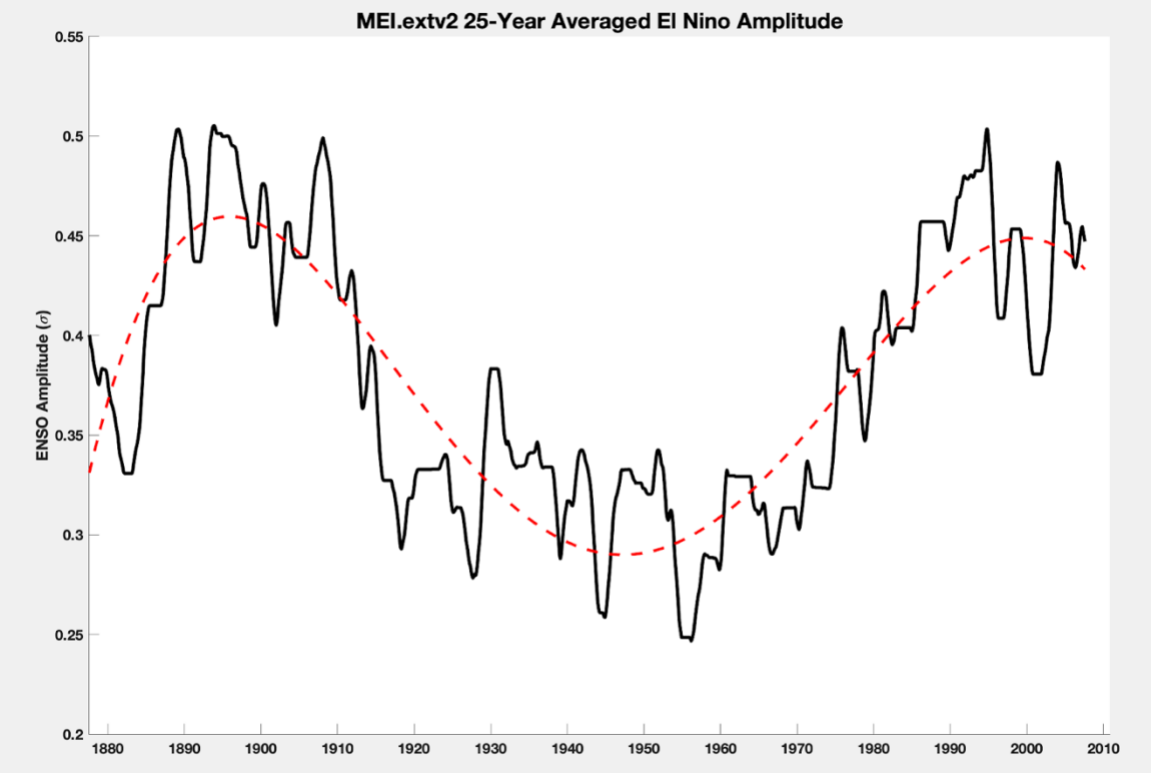

Figure 45. MEI.extv2 25-year averaged El Nino Amplitude (1878-2012) (motivated by Garcia-Herrera et al (2008)).